الجمهورية الجزائرية الديمقراطية الشعبية

République Algérienne Démocratique et Populaire
Ministère de L'Enseignement Supérieur et de la Recherche Scientifique



UNIVERSITÉ SETIF 1-Ferhat ABBAS

FACULTÉ DE TECHNOLOGIE

THÈSE

Présentée au Département de Génie des Procédés

Pour l'obtention du diplôme de

DOCTORAT

Domaine : Sciences et Technologie

Filière : Génie des Procédés **Option : Génie Pharmaceutique**

Par

BENBEKAI RIMA

THÈME

Synthèse de nouveaux supports à base de matériaux naturels pour la libération des médicaments.

Soutenue le 20 / 06 /2026 devant le Jury :

BAITICHE Milad	**Professeur**	**Univ. Sétif1-FerhatABBAS**	**Présidente**
CHEBLI Derradji	**Professeur**	**Univ. Sétif1-FerhatABBAS**	**Directeur de thèse**
BOUGUETTOUCHA Abdallah	**Professeur**	**Univ. Sétif1-FerhatABBAS**	**Co-Directeur**
KAHOUL Fares	**Professeur**	**Univ. M'sila**	**Examinateur**
REFFAS Abdelbaki	**Professeur**	**Univ. M'sila**	**Examinateur**
SOLTANI El Khamsa	**Professeur**	**Univ. Sétif1-FerhatABBAS**	**Examinatrice**

الجمهورية الجزائرية الديمقراطية الشعبية

DEMOCRATIC AND POPULAR REPUBLIC OF ALGERIA
MINISTRY OF HIGHER EDUCATION AND SCIENTIFIC RESEARCH



Setif 1 University-Ferhat ABBAS

Faculty of technology

Thesis submitted to the Process Engineering Department for a Doctorate Degree

Domain: Science and Technology

Section: Process Engineering **Option: Pharmaceutical Engineering**

BY

BENBEKAI RIMA

TITLE OF THE THESIS

Synthesis of new carriers based on natural materials for drug release.

BAITICHE Milad	**Professor**	**SETIF1University-Ferhat ABBAS**	**Chairman**
CHEBLI Derradji	**Professor**	**SETIF1University-Ferhat ABBAS**	**Supervisor**
BOUGUETTOUCHA Abdallah	**Professor**	**SETIF1University-Ferhat ABBAS**	**Co-Supervisor**
KAHOUL Fares	**Professor**	**M'sila University**	**Examiner**
REFFAS Abdelbaki	**Professor**	**M'sila University**	**Examiner**
SOLTANI El Khamsa	**Professor**	**SETIF1University-Ferhat ABBAS**	**Examiner**

Defended on 20 / 06 / 2026 in front of the Jury:

Table of contents

Title	Page
Table of content	i
Acknowledgements	vii
Dedication	viii
List of tables	ix
List of figures	xi
List of abbreviation	xiv
General introduction	1
Chapter 1: literature review on zeolites, layered double hydroxides, and theoretical frameworks in drug delivery systems	
Section I: zeolite	**8**
1. Definition of zeolite	8
2. Zeolite: structure and properties	9
3. Classifications	9
4. Types of zeolites	11
4.1 Natural zeolite	12
4.2 Synthetic zeolite	12
5. Synthesis methods	13
5.1 Hydrothermal synthesis	13
5.2 Solvothermal synthesis	14
5.3 Microwave assisted method	14
5.4 Emulsion method	14
5.5 Ionothermal synthesis	15
6. Applications	16
7. Zeolite in drug delivery system	19
a. Physical system	19
b. Chemical system	20
c. Biological system	20
Section II: Layered Double Hydroxides LDH	**23**

1. History of LDH	23
2. Structure of layered double hydroxides	24
3. Synthesis methods	25
3.1 Co-precipitation	25
3.2 Sol-gel method	26
3.3 Ion exchange method	26
3.4 Homogenous precipitation method	27
3.5 Manual grinding method	27
3.6 Salt oxides method	28
3.7 Hydrothermal and solvothermal method	28
3.8 Electrocoagulation method	29
3.9 Reconstruction of LDHs	29
3.10 Microwave assisted method	30
3.11 Non aqueous precipitation method for small LDHs	30
4. Biomedical applications of layered double hydroxides	31
4.1 Drug delivery systems	31
4.2 Antimicrobial applications	32
Section III: Computational modeling approaches	**32**
1. Computational chemistry	33
1.1 Density functional theory (DFT)	33
1.2 Molecular docking study	35
1.2.1 Preparation of active compound (ligand)	35
1.2.2 Preparation of protein (receptor) and the grid box	36
1.2.3 Molecular docking study	36
2. Advanced modeling and optimization techniques	36
2.1 RSM: Response Surface Methodology	37
2.2 ANN: Artificial Neural Networks	37
2.3 ANFIS: Adaptive Neuro-Fuzzy Inference system	39
2.4 GA: Genetic Algorithms	40
References	41

Chapter 2: Materials and methodologies for synthesis and analysis in drug delivery research.	
1. Materials and methods	50
1.1 Chemicals	50
1.2 Preparation of zeolite P from expanded perlite	50
1.2.1 Pretreatment	50
1.2.2 Hydrothermal synthesis of zeolite P	50
1.2.3 Photodeposition of zeolite P by 1% of silver	51
1.3 Preparation of sodalite from raw bentonite	51
1.4 Synthesis of Layered Double Hydroxides LDH	52
1.5 Drug loading	53
1.5.1 Loading of ibuprofen into zeolite P	53
1.5.2 Loading of ibuprofen into sodalite	53
1.5.3 Loading of ibuprofen into LDH	53
1.5.3.1 Physical mixture	53
1.5.3.2 Dissolution of ibuprofen in alcoholic medium	53
1.6 Dissolution studies	54
1.6.1 Release of ibuprofen from zeolite P and LDH	54
1.6.2 Release of ibuprofen from sodalite	54
1.7 Physico-chemical characterizations	55
1.8 The antimicrobial activity of zeolite P	56
1.8.1 The antibacterial activity	56
1.8.1.1 Bacterial strains and chemical product	56
1.8.2 Well diffusion method for the antibacterial activity of our zeolite P	57
1.8.3 Determination of the minimum inhibitory concentration (MIC) of zeolite P	57
1.9 The minimum antifungal concentration of zeolite P	58
1.9.1 Preparation of the Spore Suspension for Antifungal Evaluation	58
1.9.2 Determination of the Minimal antifungal concentration (MFC)	58
2. Computational method	59
2.1 DFT calculations	59

2.2 Molecular docking	60
3. Artificial Intelligence	61
3.1 Response surface methodology	61
3.2 Artificial neural network	62
3.3 Adaptive neuro fuzzy inference system	64
3.4 Model performance indices	65
References	68
Chapter 3: New synthesis of zeolite P from expanded perlite for gastrointestinal drug release using ibuprofen as a NSAID model. DFT calculation, molecular docking and antimicrobial activity.	
Results and discussion	71
1. Physico-chemical characterizations	71
1.1 The X-ray fluorescence (XRF) analysis	71
1.2 X-ray diffraction (XRD) analysis	72
1.3 Scanning electron microscopy (SEM) and EDS analysis of zeolite P	74
1.4 Fourier Transform Infra-Red (FTIR)	77
1.5 Point of pH zero charge pH_{PZC}	78
1.6 Thermogravimetric analysis TGA and differential scanning calorimetry DSC	79
1.7 N_2 adsorption/desorption isotherm of zeolite P	82
2. Theoretical calculations: DFT and molecular docking studie	85
2.1 DFT calculations results of ibuprofen	85
2.2 Molecular docking results of ibuprofen	70
3. Drug release profiles	92
4. Antimicrobial activity of zeolite P	94
4.1 The antibacterial activity	94
4.2 The minimum antifungal concentration MFC of zeolite P (S1) and dopped zeolite by silver (S Ag)	99
5. Conclusion	101
References	102

Chapter 4: From maghnite to sodalite: characterizations and comparative artificial intelligence-based modeling of ibuprofen release using RSM, ANN and ANFIS.	
1. Results and discussion.	105
1.1 Physico-chemical characterizations of synthetized sodalite	105
1.1.1 The XRD analysis	105
1.1.2 The FTIR analysis	106
1.1.3 The SEM/EDS analysis	108
1.1.4 The TGA/DSC analysis	110
1.1.5 The N_2 adsorption/desorption isotherm	114
1.1.6 Determination of the pH point zero charge	116
1.2 Experimental design result	117
1.3 Interactive plots and sensitivity analysis	118
1.4 Box-Behnken Design (BBD) model analysis	122
1.5 Response surface modeling	122
1.5.1 Analysis of variance	123
1.5.2 Diagnostic plots	125
1.6 Artificial neural network modeling	128
1.7 Adaptive neuro-fuzzy inference system modeling	134
1.7.1 Statistical error analysis	135
1.8 Comparative analysis of the models	136
1.9 Optimization using genetic algorithm	137
2. Conclusion	138
References	140
Chapter 5: synthesis and characterizations of calcium-iron Layered Double Hydroxides as a carrier for the release of an anti-inflammatory drug in gastrointestinal medium.	
III. Results and discussion	145
1. XRD analysis	145
2. FTIR analysis	147
3. Zeta potential	148
4. Size distribution	150

5.	Thermo-Gravimetric Analysis TGA	151
6.	N_2 adsorption-desorption isotherm	159
7.	Drug release profile	161
8.	Conclusion	165
References		166
General conclusion		169
Abstract		

Acknowledgements

I would like to begin by expressing my sincere gratitude to Professor Baitich Milad, President of the jury, for the honor of chairing my thesis defense, and for his time, valuable attention, and scientific contribution to the evaluation of this work.

I extend my sincere thanks to the members of the examination committee for their time, expertise, and valuable evaluation of this thesis. I am deeply grateful to Professors El Khamsa SOLTANI, Abdelbaki REFFAS, and Fares KAHOUL for their meticulous reading, constructive remarks, and insightful feedback as examiners.

I would like to express my deepest gratitude to Professor Derradji CHEBLI, my supervisor, whose knowledge, guidance, and unwavering support were essential to the completion of this work. My sincere appreciation also goes to Professor Abdallah BOUGUETTOUCHA, my co-supervisor, for his insightful advice, constructive criticism, and constant availability throughout this study.

I am especially thankful to Professor Mokhtar BOUTAHALA for his steadfast support, valuable resources, and stimulating scientific discussions during this study. I would also like to thank Professor BENGUERBA Yassine for his encouragement, constant support, and assistance throughout my doctoral journey. May you always remain brilliant, my professor.

I would also like to express my heartfelt gratitude to Professor Sahar MUSTAPHA for making the extraordinary journey from Egypt to Algeria to attend my defense. I sincerely thank her, from Mansoura University in Egypt, for accepting me for a 25-day research internship. I would like to extend my thanks to Dr. CHADI, Professor Ismail SAMIR, and Professor MUSTAPHA Mohcine for their kindness, guidance, and the enriching experiences they shared with me during my stay.

For their significant contributions to this work, I wish to thank Doctors Riyad BOURZAMI, Wafa ZAIBET, Hichem ATTOUT, and Sarra AGA. I sincerely appreciate Dr. Faouzi LASMI for his constant encouragement, support, and commitment to the theoretical components of this research. I am also grateful to Dr. Mahdi ACHOUR for his unwavering support and willingness to lend a hand whenever needed.

I am truly thankful to Professor Antonio GIL from the Public University of Navarre (UPNA), Pamplona, Spain, for welcoming me during a 15-day study trip and for providing access to essential physicochemical characterization facilities. I also wish to thank doctoral researcher Aziza Imane BOULAHBAL for her time, cooperation, and kind support throughout my research efforts, as well as Mr. PABLO for his technical assistance.

I extend my sincere gratitude to the Laboratory of Process and Environmental Engineering (LGPC) of Ferhat Abbas University Setif 1. I am grateful to all the professors and doctoral students for their encouragement and collaborative spirit. The members of Professor ZOUAOUI's laboratory deserve special mention, particularly KAMEL and IMADE. I also greatly appreciate the invaluable advice, commitment, and unwavering support of Dr. Nour El Houda HAMMOUDI.

Finally, I would like to express my gratitude to the Algerian Ministry of Higher Education and Scientific Research for the institutional and financial support that made this study possible.

Rima BENBEKAI

Dedication

I am deeply grateful to my beloved parents, ZERRARGA Fatiha and BENBEKAI Abderrahmane, whose love, guidance, and unwavering support have shaped me into the person I am today.

I would also like to express my sincere gratitude to my sisters, my brother, and my brother's wife, for their constant encouragement, support, and motivation.

I am especially thankful to the children of my sisters and brother, whose presence has brought joy, inspiration, and warmth to my life.

To my husband, Thank you for always encouraging me and standing by my side at every moment. Your support, patience, and belief in me have been a constant source of strength throughout this journey.

Finally, I dedicate this work, with love and gratitude, to all those who have inspired and supported me throughout my journey

Rima BENBEKAI

List of tables

Title of table	Page
Chapter 1: literature review on zeolites, layered double hydroxides, and theoretical frameworks in drug delivery systems.	
Table 1: Classification of zeolite based on Si/Al ratio.	10
Table 2: Classification of zeolite based on the pore size.	11
Chapter 2: Materials and methodologies for synthesis and analysis in drug delivery research.	
Table 1: Factors levels of independent variables for the release of ibuprofen.	61
Table 2: Statistical error functions.	66
Chapter 3: New synthesis of zeolite P from expanded perlite for gastrointestinal drug release using ibuprofen as a NSAID model. DFT calculation, molecular docking and antimicrobial activity.	
Table 1: The chemical compositions of expanded perlite.	72
Table 2: The BET parameters of zeolite P.	83
Table 3: The obtained results of the quantum chemical parameters of ibuprofen molecule using the DFT-B3LYP-6-311G (d, p) method.	89
Table 4: The thermochemistry and electronic properties of ibuprofen molecule using the DFT-B3LYP-6-311G (d, p) method.	70
Table 5: Binding affinity and interaction types between ibuprofen and 5f1a receptor.	92
Table 6: The diameters of the inhibition zones of zeolite P (S1) and dopped zeolite P (S Ag).	96
Table 7: The minimum inhibitory concentration MIC of zeolite P.	97
Table 8: Comparison of the antibacterial activity from literature.	98
Table 9: the Minimal antifungal concentration (MFC) of zeolite P.	100
Chapter 4: From maghnite to sodalite: characterizations and comparative artificial intelligence-based modeling of ibuprofen release using RSM, ANN and ANFIS.	
Table 1: RSM, ANFIS, and ANN models.	118
Table 2: Model Summary Source: Authors.	122

Table 3: Statistical summary of the models investigated.	123
Table 4: ANOVA and model coefficients for the release process.	125
Table 5: Values of connection weights and biases for the completed neural network model. Source: Authors.	131
Table 6: Statistical error indices of the RMS, ANN, and ANFIS.	136

List of figures

Title of figure	Page
Chapter 1: literature review on zeolites, layered double hydroxides, and theoretical frameworks in drug delivery systems.	
Figure 1: TO4 structure of zeolite.	8
Figure 2: The structure of layered double hydroxides.	25
Figure 3: General structure of an Artificial Neural Network (ANN) in a three-layered Multilayer Perceptron (MLP) form.	38
Chapter 2: Materials and methodologies for synthesis and analysis in drug delivery research.	
Figure 1: Hydrothermal synthesis of zeolite P from expanded perlite.	51
Figure 2: Synthesis of sodalite from raw bentonite.	52
Figure 3: The crystal structure of 5f1a ibuprofen's receptor, and the ibuprofen structure on 3D.	61
Figure 4: ANN architecture structure of ibuprofen release.	63
Figure 5: ANFIS structure of the ibuprofen release.	64
Chapter 3: New synthesis of zeolite P from expanded perlite for gastrointestinal drug release using ibuprofen as a NSAID model. DFT calculation, molecular docking and antimicrobial activity.	
Figure 1 a: XRD of the zeolite P synthesized from expanded perlite after her pretreatment with 0.1M HCl at 75°C for 3Hours.	73
Figure 1 b: The percent of various phase in XRD by Rietveld method.	75
Figure 2: SEM images (a) and the EDS analysis (b) of zeolite P.	76
Figure 3: FTIR spectra of the zeolite P synthesized from expanded perlite after its pretreatment by 0.1M HCl at 75°C for 3 hours, loaded by ibuprofen and its photodeposition by Ag.	77
Figure 4: Point of zero charge pH_{PZC} of synthetic zeolite P.	78
Figure 5 a: TGA / DSC analysis of zeolite P.	80
Figure 5 b: TGA and DTG analysis of zeolite P, ibuprofen and zeolite P-ibuprofen.	82

Figure 6 a: N_2 adsorption / desorption isotherm of zeolite P.	84
Figure 6 b: Particle size distribution of zeolite P.	85
Figure 7: The geometry optimization using DFT calculations of ibuprofen.	88
Figure 8: Interactions types between ibuprofen and 5f1a.	91
Figure 9: Ibuprofen release profiles in simulated gastrointestinal medium.	93
Figure 10: The antibacterial activity of **(a)** zeolite P (S1) and **(b)** dopped zeolite P with 1% silver (S Ag).	95
Figure 11: Determination of the MFC of zeolite P (S) and dopped zeolite P with silver (S2 Ag).	99
Chapter 4: From maghnite to sodalite: characterizations and comparative artificial intelligence-based modeling of ibuprofen release using RSM, ANN and ANFIS.	
Figure 1: XRD analysis of synthetic zeolite sodalite from bentonite.	106
Figure 2: FTIR analysis of synthetic zeolite sodalite from bentonite.	108
Figure 3: SEM (a) and EDX (b) analysis of synthetic zeolite sodalite from bentonite.	110
Figure 4: TGA/DSC analysis of (a): synthetic zeolite sodalite from bentonite, (b): ibuprofen and (c): ibuprofen loaded into sodalite.	113
Figure 5: N_2 adsorbed-desorbed isotherm analysis of synthetic zeolite sodalite from bentonite.	115
Figure 6: Particle size distribution of synthetic zeolite sodalite from bentonite.	116
Figure 7: The pH point zero charge of sodalite.	117
Figure 8: Surface (3D) and contour plots of the release of ibuprofen.	122
Figure 9: RSM diagnostic plots for (a) Predicted vs actual, (b) Normal plot of residual, and (c) Perturbation.	127
Figure 10: Plot of the experimental run order against the externally studentized residuals. Source: Authors.	128
Figure 11: ANN performance validation plot.	130
Figure 12: ANN correlation plots for (a) training, (b) validation, (c) testing and (d) overall network processes.	132

Figure 13: Training State.	133
Figure 14: (a) ANFIS Sugeno training error and (b) ANFIS distribution of predicted and experimental data of the release process.	135
Chapter 5: synthesis and characterizations of calcium-iron Layered Double Hydroxides as a carrier for the release of an anti-inflammatory drug in gastrointestinal medium.	
Figure 1: XRD spectra of (a) CaFe -CO_3^{2-} - LDH before calcination (orange), (b) CaFe - CaFe -CO_3^{2-} - LDH calcined at 450°C (red) and after calcination at 550°C (wine).	146
Figure 2: FTIR spectra of CaFe -CO_3^{2-} -LDH.	147
Figure 3: zeta potential of (a) CaFe -CO_3^{2-} -LDH uncalcined, (b) CaFe -CO_3^{2-} -LDH calcined at 450°C and (c) CaFe -CO_3^{2-} -LDH calcined at 550°C.	149
Figure 4: size distribution of (a) CaFe -CO_3^{2-} -LDH uncalcined, (b) CaFe -CO_3^{2-} -LDH calcined at 450°C and (c) CaFe -CO_3^{2-} -LDH calcined at 550°C.	151
Figure 5: Thermogravimetric analysis of CaFe -CO_3^{2-} -LDH uncalcined, CaFe -CO_3^{2-} -LDH calcined and ibuprofen.	156
Figure 6: TGA/DSC curve of LDH-ibuprofen.	158
Figure 7: N_2 adsorption-desorption isotherm of uncalcined LDH.	160
Figure 8: Particle size distribution of uncalcined LDH.	161
Figure 9: drug release from (a) CaFe-CO_3^{2-} -LDH non calcined, (b) CaFe-CO_3^{2-} -LDH calcined at 450°C and from (c) CaFe-CO_3^{2-} -LDH calcined at 550°C.	163

List of abbreviations

Abbreviation	Meaning
ANFIS	Adaptive Neuro Fuzzy Inference System
ANN	Artificial Neural Network
BBD	Box-Behnken Design
DFT	Density Functional Theory
DSC	Differential Scanning Calorimetry
EDX	Energy Dispersive X-ray
FTIR	Fourier Transform Infra-Red
GA	Genetic Algorithm
LDH	Layered Double Hydroxides
MFC	Minimal Antifungal Concentration
MIC	Minimum Inhibitory Concentration
pH	Potential of Hydrogen
RSM	Response Surface Methodology
SEM	Scanning Electron Microscopy
TGA	Thermo-Gravimetric Analysis
XRD	X-Ray Diffraction
XRF	X-Ray Fluorescence

General introduction

General introduction

The rapid development of novel technologies in pharmaceutical formulations is critical, given their significant implications for human health and well-being. As we advance towards more efficient drug delivery systems and innovative therapeutic strategies, the prospects for enhancing patient outcomes and improving quality of life grow substantially. These technological advancements not only optimize the manufacturing process but also facilitate the creation of more targeted and personalized treatment options, thereby underscoring their vital role in the future of healthcare[1]. One of the major challenges in pharmaceutical research is achieving precise and controlled delivery of therapeutic agents to targeted sites within the body. This objective can be accomplished through the development and application of suitable drug delivery systems. Drug release behavior is governed by multiple factors, including the physicochemical properties of the drug and the structural and functional characteristics of the delivery carrier. The selection of an appropriate delivery system plays a critical role in regulating the release kinetics, influencing the rate and duration of drug availability at the intended site. An optimal carrier system not only safeguards the drug from premature degradation but also facilitates its controlled release to enhance therapeutic efficacy while reducing adverse effects. Through careful design and modification of drug carriers, delivery strategies can be optimized to address specific clinical requirements, ultimately improving treatment outcomes [2]. Ibuprofen is a non-steroidal anti-inflammatory drug (NSAID) belonging to the propionic acid derivative family, used as an analgesic, antipyretic, and anti-inflammatory agent to relieve pain, fever, and inflammation. Chemically, it is 2-(4-isobutylphenyl) propanoic acid [3], with the molecular formula $C_{13}H_{18}O_2$ and a molar mass of approximately 206.28 g/mol. It occurs as a white crystalline powder, poorly soluble in water but soluble in organic solvents such as ethanol and acetone, with a melting point of approximately 75-77 °C and a pKa close to 4.4, classifying it as a weak acid [4]. Its mechanism of action relies primarily on the reversible, non-selective inhibition of the cyclooxygenase enzymes COX-1 and COX-2, which are responsible for converting arachidonic acid into prostaglandins. The resulting decrease in prostaglandin synthesis leads to a reduction in pain, fever, and the inflammatory response [3].

In this context, we have selected zeolite as a cation exchange material and layered double hydroxide (LDH) as an anion exchange component. These substances will serve as carriers to develop a modified drug release profile. By utilizing these carriers, we aim to enhance the efficacy

of the drug while reducing the side effects or adverse reactions. This approach allows for more controlled and targeted delivery of the drug, ultimately improving treatment outcomes and patient safety.

Zeolites are crystalline substances that consist of aluminosilicate materials that incorporate alkali or alkaline earth metal cations and possess 3D frameworks composed of interconnected $[SiO_4]^{4-}$ and $[AlO_4]^{5-}$ tetrahedral units linked through shared oxygen atoms [5]. In zeolites, the negative charges within the framework occur due to aluminum atoms substituting silicon atoms in the structure. These negative charges are balanced by cations that exist outside the framework. The structural and compositional variations of zeolites lead to the formation of pore windows that have specific sizes, typically between 4 and 10 Å. Recent discoveries have also identified germanosilicates with extra-large pores that can expand this size to around 20 Å. The cations that compensate for the negative charges in the framework are present in a precise ratio that matches the amount of negative charge. This allows for the possibility of exchanging these cations without damaging the zeolite's structural integrity [6]. The wide ranging applicability of these materials spans numerous technological fields, where they serve as effective adsorbents, catalysts, ion exchange media [7], and molecular sieves [8], capable of selective size based separation. Their unique characteristics including highly porous structures, ion exchange capability, excellent water holding capacity, immunomodulatory and antioxidant properties, biocompatibility, and long-term chemical and biological stability make them particularly attractive for biomedical uses. These applications encompass drug delivery systems, wound management, tissue regeneration, antimicrobial therapies, surface modification of implants, imaging contrast enhancement, detoxification processes, gas adsorption, hemodialysis, and the development of endodontic materials [9, 10]. Zeolites can be produced from different naturally occurring raw materials, particularly bentonite and expanded perlite. Bentonite is a natural clay widely exploited in many industrial fields because of its binding, plasticizing, and suspending properties. Structurally, it is composed of two silica tetrahedral layers surrounding a central alumina octahedral layer. Its ideal chemical composition is approximately 71.62% SiO_2, 15.22% Al_2O_3, and 13.17% H_2O. Owing to this aluminosilicate composition, bentonite represents a promising precursor for zeolite synthesis. In particular, its Si/Al ratio, close to 4.7, falls within a suitable range for the formation of zeolitic materials [11]. While perlite is an amorphous volcanic rock mainly composed of silica and alumina, it can expand up to 20 times its original volume when heated at 700-1200 °C. Expanded

perlite has attracted considerable interest in agriculture, the chemical industry, and environmental protection because of its valuable physicochemical properties, including chemical and thermal stability, adsorption capacity, and cation exchange capacity (CEC). In this context, its surface can develop silanol and silane-diol groups, which are able to interact with metal oxide surfaces through the formation of Si-O-metal bonds. Therefore, expanded perlite has been successfully used as a raw material for zeolite synthesis [12].

Layered Double Hydroxides (LDHs) have garnered significant interest in the advancement of sophisticated drug delivery systems. Their designation as smart excipients arises from numerous beneficial attributes [13]. LDHs possess the ability to intercalate biomaterials within their interlayer regions [14] and adsorb a variety of substances across their extensive surface area. Their flexible structure enables swelling, which is beneficial for modulating drug release profiles. Furthermore, LDHs exhibit high chemical [15] and thermal stability, thus qualifying them for applications. Their significant biocompatibility and ease of synthesis enhance their appeal within the pharmaceutical industry [16]. These attributes collectively establish LDHs as prospective candidates for the enhancement of drug delivery systems, potentially resulting in improved therapeutic efficacy and patient adherence [13].

This thesis is structured into five chapters, focusing on the synthesis of new supports intended to modify the release profile of an anti-inflammatory drug within gastrointestinal fluids. The primary goal is to utilize zeolite as a cation exchanger and Layered Double Hydroxides (LDH) as an anion exchanger, aimed at reducing side effects while enhancing the therapeutic efficacy of the active compound.

Chapter 1 presents a literature review on zeolites, layered double hydroxides (LDHs), and theoretical methodologies, encompassing Density Functional Theory (DFT), molecular docking, and artificial intelligence modeling techniques, including Response Surface Methodology (RSM), Artificial Neural Networks (ANN), and Adaptive Neuro-Fuzzy Inference Systems (ANFIS).

Chapter 2 presents the materials used in this study and describes the experimental procedures in detail, outlining each stage of the research design and analytical methods.

Chapter 3 discusses the synthesis of zeolite P from expanded perlite, serving as both the starting material and aluminosilicate source. The chapter also includes theoretical studies involving DFT and molecular docking of ibuprofen to assess its interaction with the synthesized zeolite.

Chapter 4 focuses on the synthesis and characterization of sodalite derived from raw bentonite, along with a comparative analysis of ibuprofen release using artificial intelligence-based modeling techniques, including RSM, ANN, and ANFIS.

Chapter 5 delves into the synthesis of Calcium-Iron Layered Double Hydroxide (CaFe-CO_3^{2-} LDH) designed as a carrier for the controlled release of an anti-inflammatory drug in a gastrointestinal medium.

In conclusion, this structured approach encompasses comprehensive theoretical and practical investigations aimed at advancing drug delivery systems, contributing to improved therapeutic strategies in pharmacology.

References

[1] I. M. S. Souza and al, "Experimental and molecular modelling study of beta zeolite as drug delivery system," Microporous and mesoporous materials, vol. 321, no. February, pp. 1–10, 2021.

doi: 10.1016/j.micromeso.2021.111152.

[2] P. Shailaja and K. S. Ashok, "A promising oral drug delivery system of microsponges : a brief review a promising oral drug delivery system of microsponges : a brief review," Research J. Pharm. and Tech, vol. 15, 2022.

doi: 10.52711/0974-360X.2022.00725.

[3] M. Mahfuza and al, "Modification of ibuprofen to improve the medicinal effect ; structural , biological , and toxicological study," *Heliyon*, vol. 10, no. 5, p. e27371, 2024.

doi: 10.1016/j.heliyon.2024.e27371.

[4] S. Lerdkanchanaporn and D. Dollimore College, " Pharmaceuticals: A thermal analysis study of ibuprofen," Journal of Thermal Analysis, Vol. 49 (1997) 879-886, 1997.

[5] H. E. Mgbemere and al, "Zeolite synthesis, characterisation and application areas: a review," Int. Res. J. Environ. Sci., vol. 6, no. 10, pp. 45–59, 2017.

[6] Q. Lang and al, "Zeolites for the environment," *Green Carbon*, vol. 2, no. 1, pp. 12–32, 2024.

doi: 10.1016/j.greenca.2024.02.007.

[7] G. Pokuaa and al., "Characterization of chitosan / zeolite drug delivery composite and curcumin release kinetics in a simulated ph environment," Sci. African, vol. 28, no. February, p. e02668, 2025.

doi: 10.1016/j.sciaf.2025.e02668.

[8] G. Ulian and al, "Structural and elastic behaviour of sodalite $Na_8(Al_6Si_6O_{24})Cl_2$ at high-pressure by first-principle simulations," minerals, vol. 8, 2022.

https://doi.org/ 10.3390/min12101323.

[9] H. Serati-nouri and al, “Biomedical applications of zeolite-based materials : A review,” Materials Science & Engineering C, vol. 116, no. February, p. 111225, 2020.

doi: 10.1016/j.msec.2020.111225.

[10] J. Matusiak and al, “Zeolites and zeolite imidazolate frameworks on a quest to obtain the ideal biomaterial for biomedical applications : A review,” Mater. Today, vol. 67, no. August, pp. 495–517, 2023.

doi: 10.1016/j.mattod.2023.06.008.

[11] A. You, M. Be, and I. In, “Synthesis of zeolite a from bentonite via hydrothermal method: the case of different base solution,” vol. 060006, no. April 2016, 2020.

https://doi.org/10.1063/5.0025043.

[12] I. M. Ahmed and al., “Modification of perlite to prepare low cost zeolite as adsorbent material for removal of ^{144} Ce and $^{152+154}$ Eu from aqueous solution,” no. July, 2020.

doi: 10.1515/ract-2019-3221.

[13] L. Moreira and al., “Layered double hydroxides as promising excipients for drug delivery purposes,” european journal of pharmaceutical sciences, vol. 165, no. June, 2021.

doi: 10.1016/j.ejps.2021.105922.

[14] E. E. Gaskell and al, “Ibuprofen intercalation and release from different layered double hydroxides,” therapeutic delivery, vol. 9, pp. 653–666, 2018.

doi: 10.4155/tde-2018-0046.

[15] V. K. A. Shirin and al, “Advanced drug delivery applications of layered double hydroxide,” J. Control. Release, vol. 330, no. August 2020, pp. 398–426, 2021.

doi: 10.1016/j.jconrel.2020.12.041.

[16] A. Y. A. Kaassis and al, “Biocompatible hydroxy double salts as delivery matrices for non-steroidal anti-inflammatory and anti-epileptic drugs,” Appl. Clay Sci., vol. 221, no. August 2021, p. 106456, 2022.

doi: 10.1016/j.clay.2022.106456.

Chapter 1

Literature Review on Zeolites, Layered Double Hydroxides, and Theoretical Frameworks in Drug Delivery Systems.



Section I: Zeolite

1. Definition of zeolite

The term "zeolite" originates from the Greek language, combining two elements: "zeo," which translates to "I boil," and "lithos," meaning "stone." This terminology was first proposed by Swedish mineralogist Axel Frederik Cronstedt in 1756 [1]. Zeolites are categorized as inorganic porous crystalline substances belonging to the tectosilicate mineral group [2]. Their structural design features a three-dimensional network of TO_4 tetrahedral units, where T can represent either Silicon (Si) or Aluminum (Al), interconnected by bridging oxygen atoms [3, 4]. This crystalline framework creates uniform channels and voids, which confer unique porous properties to zeolites. The negative charge resulting from the isomorphous substitution of Si by Al in the structure is balanced by exchangeable cations, such as sodium or calcium. Due to their high specific surface area, uniform pore structure, selective adsorption capabilities, and remarkable chemical and thermal stability, zeolites are widely utilized as adsorbents, ion exchange agents, catalysts, and carriers for drug delivery, facilitating the encapsulation and controlled release of pharmaceutical compounds [2].

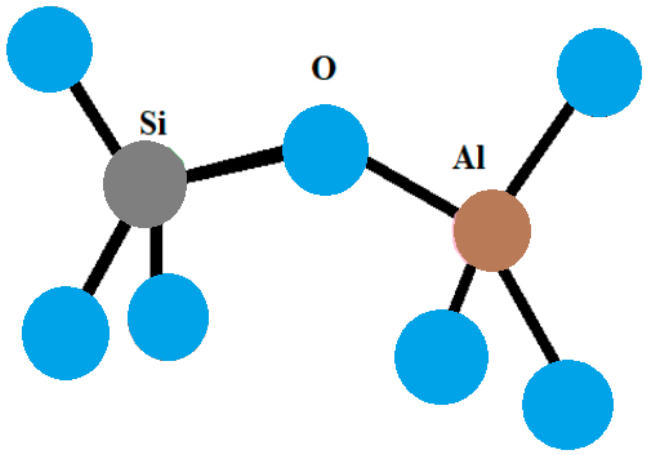


Figure 1: TO_4 structure of zeolite [5].

2. Zeolite: structure and properties

Zeolite frameworks can be deliberately modified through the partial substitution of silicon atoms by aluminum within their tetrahedral network. The relative abundance of aluminum is commonly described using the silica to alumina ratio (SiO_2/Al_2O_3), which reflects the distribution of silicon and aluminum species within the structure. The incorporation of aluminum generates a localized negative charge in the lattice, which must be counterbalanced by extra framework cations in order to maintain overall electroneutrality. These compensating species are typically monovalent or protonic ions, such as NH_4^+, H^+, or Na^+. In cases where protons serve as the charge balancing entities, Bronsted acidic centers are established, leading to enhanced acidity compared with materials containing lower aluminum concentrations. Through careful adjustment of the silicon to aluminum proportion, it becomes possible to tailor essential framework characteristics, including surface polarity, ionic character, and acid strength, both within the internal pore architecture and at the external surface. The ability to precisely control these structural and chemical features has positioned zeolites as highly promising candidates for application in drug delivery technologies. Their intrinsic microporous architecture can be engineered to match the molecular dimensions of specific pharmaceutical compounds, facilitating efficient encapsulation. The presence of an extensive internal surface area, coupled with significant pore volume, supports high drug-loading capacities, while the uniformity of pore dimensions contributes to predictable and sustained release behavior. In addition, the favorable biocompatibility profile and minimal cytotoxicity associated with zeolitic materials further enhance their suitability for medical use. Consequently, the combination of adjustable framework composition, high adsorption efficiency, and compatibility with biological environments underscores the potential of zeolites as advanced carriers for controlled therapeutic delivery [6].

3. Classifications

The silicon to aluminum (Si/Al) ratio plays a fundamental role in defining both the classification and physicochemical behavior of zeolitic materials. Based on this parameter, zeolites are commonly grouped into three distinct categories. Materials with low Si/Al ratios typically fall within the approximate range of 1 to 1.5, whereas intermediate compositions correspond to ratios

between about 2 and 5. Zeolites exhibiting high silicon content are characterized by Si/Al ratios exceeding 10 [7].

Table 1: Classification of zeolite based on Si/Al ratio [5].

Varieties of zeolite	Ratio of Si / Al	Example
Low Si content	From 1.0 to 1.5	Zeolite; X, 4A
Medium Si content	From 2.0 to 5.0	Zeolite Y, mordenite
High Si content	More than 10	Zeolite; ZSM-5, beta
Silica based molecular sieves	More than 100	Silicite

The Si/Al ratio in zeolites is pivotal in influencing their physicochemical properties and efficacy. An increase in the Si/Al ratio leads to improvements in various characteristics, such as thermal stability, hydrophobicity, strength of acidic sites, affinity for non-polar substances, and acid resistance. In contrast, a decrease in this ratio enhances other properties, particularly hydrophilicity, ion exchange capacity, number of acidic sites, availability of extra-framework cations, and interactions with polar molecules. This inverse relationship between the Si/Al ratio and zeolite characteristics facilitates the customization of zeolite materials for specific applications by adjusting the silicon to aluminum ratio during their synthesis. Zeolites with higher Si/Al ratios are generally favored for catalytic applications that require robust acid sites and hydrophobic properties, while those with lower Si/Al ratios are better suited for ion exchange processes and adsorption of polar molecules due to their increased hydrophilicity and superior cation exchange capacity [5]. Zeolites may be classified according to the dimensions of their principal pore apertures: microporous structures (characterized by 8 membered rings or smaller), intermediate porous frameworks (possessing 10 membered rings), macroporous architectures (comprising 12 membered rings), and ultra-large porous systems (exceeding 12 membered rings) [7].

Table 2: Classification of zeolite based on the pore size [5].

Pore size	Zeolite rings	Diameter of the pore (nm)	Exemple
Small	08	From 0.3 to 0.45	LTA
Medium	10	From 0.45 to 0.6	ZSM-5
Large	12	From 0.6 to 0.8	Faujasite (X, Y)
Extra-large	14	From 0.8 to 1.0	VIP 5, Cloverite

Zeolites can be classified into two primary categories: natural and synthetic zeolites. Natural zeolites are produced through geological processes and are found in a range of mineral deposits. Notable examples include clinoptilolite, erionite, scolecite, offretite, chabazite, natrolite, and mordenite. These natural forms are distinguished by their unique porous structures, which provide exceptional ion exchange capacity and selectivity, rendering them useful in various applications such as water purification, agriculture, and catalysis. In contrast, synthetic zeolites are created in laboratories via specific chemical methods to achieve desired structural characteristics and functionalities. This category includes types like Zeolite A (LTA), Zeolite X, Zeolite Y, and Zeolite NaA. These designed materials offer enhanced control over properties such as pore dimensions, framework architecture, and thermal stability, making them suitable for specialized applications, including catalysis, gas separation, and acting as adsorbents in numerous industrial processes. Furthermore, zeolites can be further classified into distinct structural frameworks based on the unique arrangements of their polyhedral units. The adaptability of both natural and synthetic zeolites, along with their capacity for customization for particular applications, highlights their significance in fields such as environmental remediation, chemical processing, and materials science [8].

4. Types of zeolites

Based on their origin, zeolites are classified into two distinct groups: naturally occurring zeolites and synthetic zeolites. The former encompasses more than 40 known mineral species, whereas the

latter comprises over 150 framework types that have been synthesized through laboratory using different methods [9].

4.1 Natural zeolite

Natural zeolites originate through protracted geological transformations spanning millennia to millions of years under distinctive environmental parameters. The characteristic features of natural zeolites, including their intricate channel architecture and ion exchange functionality, resulted from ancient volcanic eruptions that dispersed aluminosilicate-rich ash materials into alkaline terrestrial environments. The geological mechanisms governing zeolite genesis encompass volcanic phenomena, hydrothermal modification, and sedimentary diagenetic reactions. These minerals develop when volcanic debris and ash deposits interact with alkaline aqueous solutions, subsequently crystallizing within post depositional settings over extensive timeframes in shallow marine environments. The majority of naturally occurring zeolites emerge during diagenetic alterations within sedimentary formations, where they manifest as secondary mineral phases produced through low-temperature and low-pressure metamorphic processes across diverse lithological units and geological contexts throughout the Earth's lithosphere. Zeolite formation necessitates alkaline chemical conditions, moderate thermal regimes (generally 40-300°C), and adequate crystallization periods, yielding a three-dimensional framework constructed through tetrahedral linkages of aluminum and silicon atoms via oxygen bridges, establishing an interconnected network of Si-O-Al, Si-O-Si, and Al-O-Al bonds [10].

4.2 Synthetic zeolite

Engineered zeolites provide distinct benefits when compared to naturally occurring zeolitic materials, particularly in terms of compositional purity, consistency of particle morphology, and resistance to elevated temperatures. Their synthesis allows precise control over framework chemistry and pore architecture, enabling the development of materials with customized properties suited to a wide range of industrial applications. In contrast to natural zeolites, synthetic forms are devoid of trace mineral contaminants such as iron or titanium that can compromise characteristics including optical quality, mechanical integrity, and catalytic efficiency.

Furthermore, the deliberate adjustment of structural and chemical parameters in synthetic zeolites facilitates superior performance in specialized functions, notably in catalytic reactions, selective adsorption, and ion-exchange processes [11].

5. Synthesis methods

Zeolite, this name was credited to the Swedish mineralogist Axel Frederik Cronstedt, who used it as early as 1756. In the 1950s, this geologist was synthesized the first zeolite, which was used in the industry for a lot of applications [12].

5.1 Hydrothermal synthesis

Hydrothermal synthesis is the conventional method for zeolite production and is typically conducted in an alkaline medium at temperatures of 90 to 150 °C and pressures of 1 to 15 bar in a closed system for 24 to 96 hours. During this process, aluminosilicate hydrogels, organic structure directing agents, and metal cations are transformed into crystalline aluminosilicate frameworks. These hydrogels are commonly prepared from aluminum and silicon containing precursors such as aluminates, aluminum salts, water glass, or kaolinite. To reduce costs, natural clays (kaolin or halloysite) and industrial or agricultural wastes, including fly ash, rice husk, and paper sludge, are often used as alternative raw materials. Crystallization involves continuous nucleation, with the highest nucleation rate occurring in the early stages, and typically yields crystals ranging from 0.1 to 10 μm at around 100 °C. By adjusting synthesis parameters, various zeolite structures such as chabazite, faujasite, phillipsite, Na-P1, and zeolites X, Y, A, and P can be obtained. Key factors influencing hydrothermal synthesis include the Si/Al ratio, NaOH concentration, crystallization temperature, and time. Low Si/Al ratios favor LTA- and X-type zeolites, whereas higher ratios promote Y, beta, and ZSM-5 type structures. Optimal NaOH concentrations ($\leq$ 3 mol l^{-1}), temperatures between 70 and 200 °C, and crystallization times of 24 to 120 h are critical for achieving high crystallinity and phase purity. For example, Na-X zeolite has been successfully synthesized from natural substrates at 80 °C using 3 mol l^{-1} NaOH, with crystallization initiating after 5 h and reaching a maximum at approximately 18 h, resulting in a product with high temporal stability [5].

5.2 Solvothermal synthesis

The solvothermal synthesis method encompasses zeolite preparation techniques that utilize various solvents as the reaction medium. Within this classification, hydrothermal synthesis can be considered a subset of the solvothermal approach, as water serves as the predominant solvent in conventional zeolite crystallization processes. However, the solvothermal methodology extends beyond aqueous systems to include a diverse range of alternative solvents, including alcohols, hydrocarbons, and pyridine, all of which have been successfully employed in zeolite synthesis. The solvents utilized in solvothermal zeolite preparation span a broad spectrum of polarity and hydrophobicity, ranging from nonpolar hydrophobic media to polar hydrophilic systems, thereby offering flexibility in controlling synthesis conditions and framework properties [13].

5.3 Microwave assisted method

Zeolite materials can be produced through solid state approaches that involve mechanical mixing and grinding of precursor components without the use of solvents. Among advanced synthesis strategies, microwave assisted techniques have gained attention due to their relatively gentle operating conditions and exceptionally short crystallization times. This approach accelerates nucleation by promoting rapid crystal growth within the reaction medium. As an example, Omisanya and co-workers reported the preparation of zeolite A from Kankara kaolin using microwave irradiation, subsequently applying the material as an adsorbent in a solar refrigeration system. Another efficient route for zeolite formation is continuous flow synthesis, which enables complete crystallization within very short timeframes ranging from seconds to minutes owing to the enhanced heat transfer efficiency of tubular reactor configurations. In this context, Pan et al. demonstrated that zeolite Socony Mobil 5 (ZSM-5) could be rapidly formed from an amorphous aluminosilicate precursor in less than one minute. Their findings highlight the strong potential of this methodology for the scalable and industrial production of zeolitic materials [14].

5.4 Emulsion method

The emulsion-based synthesis strategy, widely known as the Pickering emulsion technique, has emerged as a modern approach for the preparation of hierarchical zeolites and related porous frameworks. This methodology is based on the formation of particle stabilized emulsions, in which

inorganic species most commonly silica derived precursors act as stabilizing agents for oil-water systems formulated with either ionic or nonionic surfactants. Unlike conventional emulsions, which are only kinetically stabilized, microemulsions exhibit thermodynamic stability, making them particularly suitable for controlled material synthesis. Within this approach, surfactants play a critical role in promoting interfacial interactions between the immiscible phases, thereby enabling the formation of structured reaction environments. Zeolite nanocrystals are produced through sol-gel or polymerization processes that take place within the continuous phase of the emulsion system. Stabilization of Pickering emulsions typically arises from the combined action of charged surfactants and oppositely charged solid particles, such as silicate species. By modifying the ratio between surfactants and solid particles, phase inversion phenomena can be induced, offering additional control over the synthesis process. The principal aims of this method include the formation of nanosized zeolite crystals, the development of hierarchical pore architectures, and the regulation of particle morphology. The synthesized materials generally exhibit particle sizes below 100 nm, with size control governed by the dimensions of the emulsion droplets and the concentration of precursor species. As reported by Zhang and co-workers, the emulsion assisted crystallization mechanism proceeds through two dominant stages: first, the microemulsion environment regulates the nucleation and growth behavior of zeolitic phases; second, interactions between surfactant molecules and the evolving crystals influence their growth direction, crystal orientation, and final morphology. Despite its advantages, the scope of this synthesis route remains restricted, having been successfully applied to a limited range of zeolitic frameworks, including zeolite A, silicalite 1, ZSM-5, $AlPO_4$-5, and more recently, zeolite Y [15].

5.5 Ionothermal synthesis

Ionothermal synthesis represents an alternative route for zeolite preparation in which ionic liquids serve simultaneously as the reaction medium and the structure directing component. This dual functionality removes the need for elevated pressures typically generated by water vapor in conventional hydrothermal synthesis. The first successful application of this strategy was reported by Cooper and co-workers in 2004, who demonstrated the efficient formation of alumino-phosphate and silico-alumino-phosphate zeolitic frameworks. The resulting materials exhibited high synthesis yields along with improved surface area characteristics. The Ionothermal synthesis

represents a distinct subcategory within the broader solvothermal classification, wherein the solvents employed are predominantly ionic compounds rather than the molecular solvents characteristic of traditional solvothermal methods. The ionic liquids utilized in ionothermal zeolite synthesis possess unique physicochemical properties, particularly their negligible vapor pressures, which fundamentally distinguish this technique from conventional synthesis routes and enable crystallization to proceed under milder pressure conditions while maintaining elevated temperatures [13, 14].

6. Applications

Natural zeolites have historically found applications in various industries, including the cement sector, where they serve as effective fillers. One prominent example is clinoptilolite, which is utilized in agriculture. This zeolite acts as a potassium releasing agent, enhancing soil fertility and promoting plant growth. Its absorbent properties also help extend irrigation intervals, allowing for more efficient water use in agricultural practices. In addition to agricultural applications, natural zeolites are increasingly employed in wastewater treatment processes. They exhibit a strong capacity to remove soluble heavy metals from contaminated water, aiding in environmental cleanup and promoting sustainable water management. The ability of zeolites to adsorb heavy metals makes them valuable in mitigating pollution and protecting ecosystems. Furthermore, the detergent industry has seen significant adoption of zeolites in recent years, where they are used as builders. These zeolites enhance the cleaning efficiency of detergents by softening water and preventing the precipitation of minerals that can interfere with cleaning processes. This widespread use underscores the versatility and effectiveness of zeolites in various applications, highlighting their importance in both environmental and industrial contexts [16]. The biocompatibility of natural zeolites, such as clinoptilolite, ensures that they can be safely used in medical applications without causing significant adverse reactions. This characteristic is crucial for any material intended for drug delivery, as it minimizes potential toxicity [17, 18].

Natural zeolites demonstrate significant potential in regulating physiological fluid balance within biological systems. These microporous aluminosilicate minerals function effectively as therapeutic agents for gastro-intestinal disorders, particularly in managing diarrheal conditions through their

unique ion exchange and adsorption properties. Clinical applications have shown promising results, with clinoptilolite zeolite being successfully employed in veterinary medicine to address digestive disturbances in young livestock. Research protocols typically involve administering one gram of zeolite per kilogram of body weight, mixed with milk, to enhance immune function and provide therapeutic relief from diarrheal symptoms in calves.

The therapeutic mechanism of natural zeolites extends beyond simple fluid regulation to encompass pH buffering capabilities within physiological systems. These materials demonstrate the ability to stabilize bodily pH levels by neutralizing excess acidity, thereby maintaining optimal biochemical conditions for cellular function. The significance of pH homeostasis cannot be understated, as research indicates that chronic acidic conditions (elevated hydrogen ion concentrations) create an environment conducive to various pathological processes. Excessive acidity has been associated with compromised cognitive function, neurological symptoms including depression and anxiety, altered mental states, and reduced consciousness levels. The pH-modulating properties of zeolites therefore represent a multifaceted therapeutic approach that addresses both immediate gastrointestinal symptoms and underlying acid-base imbalances that may contribute to broader health complications.

This dual functionality of natural zeolites, combining fluid volume control with pH regulation, positions them as versatile therapeutic agents with applications spanning digestive health, immune support, and metabolic balance maintenance in both veterinary and potential human medical contexts. Synthetic zeolites have extensive industrial applications that capitalize on their precisely controlled properties and superior performance compared to natural zeolites [1]. Zeolites have traditionally served as fundamental materials in petroleum refining and petrochemical manufacturing processes, where their exceptional properties as adsorbents, ion-exchange media, and catalytic agents have been extensively utilized across industrial-scale operations. In the context of the accelerating shift toward environmentally responsible, renewable energy frameworks, improving energy efficiency has become an essential priority, shaped by both ecological and economic considerations. Against this backdrop, zeolitic materials are increasingly being explored for emerging technological applications that significantly surpass their traditional functions within the petrochemical sector.

The contemporary research focus encompasses the utilization of zeolites in processing renewable feedstock materials, where their selective adsorption and catalytic properties can facilitate the conversion of biomass and other sustainable raw materials into valuable products. Environmental applications represent another expanding frontier, with zeolites demonstrating significant potential in pollution control, contaminated site remediation, and waste treatment processes through their ability to selectively capture and neutralize harmful substances. The pharmaceutical and biotechnology sectors have increasingly recognized zeolites as promising platforms for drug delivery systems, where their controlled porosity and biocompatibility enable precise therapeutic compound release and targeted treatment approaches.

Furthermore, the development of zeolites as advanced functional materials has opened new possibilities across multiple technological domains, including energy storage systems, separation technologies, and smart material applications. This diversification of zeolite applications reflects the growing recognition of their unique structural characteristics and physicochemical properties, positioning these versatile materials as key components in addressing contemporary challenges related to sustainability, environmental protection, and human health advancement. This transformation reflects a fundamental reorientation away from conventional industrial functions toward advanced, sustainability-driven, and highly specialized applications aligned with contemporary objectives in sustainable development [12].

Zeolite nanoparticles (NPs) have attracted considerable attention in biomedical research due to their favorable biocompatibility and capacity for controlled biomolecular transport, stemming from their distinctive structural features and advantageous physicochemical characteristics relative to other mesoporous nanomaterials. These materials exhibit reduced cytotoxic effects, enhanced loading efficiency, and improved precision and effectiveness in intracellular delivery. As a result, zeolites have been investigated for a wide range of medical applications, including antidiarrheal formulations, anticancer therapies, antimicrobial treatments, and magnetic resonance imaging (MRI) contrast enhancement. Additional areas of interest include bone regeneration, neurodegenerative disease research, hemodialysis systems, pharmaceutical delivery platforms, and dental materials.

The contribution of zeolites to MRI diagnostics is particularly significant, as nanoscale porous structures have proven effective in improving image contrast. Their ability to incorporate high spin metal species enables strong interactions with surrounding water molecules, thereby accelerating proton relaxation processes. Beyond imaging, zeolites have demonstrated immunomodulatory effects and are being explored as supportive agents in oncological treatments. For example, clinical observations of activated TMA zeolite administration in patients with diabetes and cancer have been associated with reduced oxidative stress and improved overall health. In response to the growing challenge posed by multidrug resistant bacterial strains, medical researchers are investigating alternative antimicrobial strategies that circumvent the limitations of traditional organic antibiotics. In this context, nanoscale inorganic materials have emerged as promising antibacterial agents due to their high surface area to volume ratios and low toxicity. Experimental studies using micronized zeolite (MZ) in transgenic mouse models of Alzheimer's disease (AD) revealed pronounced antioxidant activity against age related neurodegenerative processes, with no detectable toxicity or long-term adverse effects. Notably, MZ treatment suppressed amyloidogenic pathways, resulting in a marked reduction in Aβ42 levels in treated animals. In addition to the therapeutic investigations, zeolite nanoparticles have also been employed in the development of diagnostic biosensors and analytical tools for Alzheimer's disease research [2].

7. Zeolite in drug delivery system

The fundamental principle underlying most drug delivery systems is the effective transport of drug molecules to their target organs while preserving their pharmaceutical and therapeutic activity. Research has demonstrated that polymer-based systems enable the regulated release of therapeutic agents, enhancing the efficiency of drug transport and minimizing toxic side effects. Drug delivery systems are generally categorized based on their release mechanisms and preparation methods. These categories include:

a. Physical Systems: which encompass porous monoliths and biodegradable systems designed for gradual drug release. These systems rely on the physical characteristics of materials to regulate drug release.

Porous monoliths, for instance, allow drugs to diffuse through their structure at controlled rates. Biodegradable systems gradually break down in the body, releasing the drug over time as the material is metabolized, thus providing a sustained release profile.

b. Chemical Systems: which focus on the immobilization of drug molecules to control their release. In these systems, drug molecules are chemically bonded to carriers, allowing for more precise control over the release rates. This approach commonly employs stimuli-responsive polymers that release therapeutic agents selectively in response to specific environmental conditions, such as pH or temperature.

c. Biological Systems: This category encompasses strategies such as gene-based therapies that are designed to act on defined biological pathways. These platforms rely on biological delivery mechanisms to introduce therapeutic material directly into targeted cells or tissues, enabling modulation of cellular activity and providing a highly effective approach for genetic level intervention [19].

Pharmaceutical agents may be administered to the human body through a range of anatomical pathways, selected according to the therapeutic objectives of the treatment. These administration routes can be designed to produce either localized effects within a specific organ or systemic action throughout the body. The selection process depends on multiple considerations, including the pathology being treated, the intended therapeutic response, and the formulation of the medicinal product. In certain cases, direct delivery to the target site is preferred, as it can enhance treatment efficiency while reducing undesirable systemic effects. In contrast, systemic administration enables widespread distribution of the drug, allowing it to reach multiple tissues, including the diseased area. This flexibility in delivery strategies allows clinicians to customize therapeutic regimens to individual patient requirements. Importantly, the chosen route of administration significantly influences pharmacokinetic processes such as absorption, distribution, metabolism, and elimination, which ultimately determine both the efficacy and safety of the drug. A comprehensive understanding of these delivery pathways is therefore essential for optimizing therapeutic design and improving clinical outcomes [20].

A numerous of studies have demonstrated that the loading of the pharmaceutical compound into zeolite frameworks make them more stable and improve the bioavailability of the active product. For this reason, the zeolite faujasite was proposed to encapsulate the poor soluble drugs [2]. Bertão et al. investigated the development of zeolite-based drug delivery systems (ZDS) constructed from a Na-Y faujasite framework, incorporating silver ions (Ag^{+}) and 5-fluorouracil (5-FU) as antimicrobial and anticancer agents, respectively. Two distinct ZDS formulations, Ag7(5-FU) @Y and Ag4(5-FU) @Y, were prepared by modulating the initial concentration of silver nitrate during the ion exchange process. Structural and compositional characterization confirmed the successful incorporation of both silver and 5-FU without inducing significant modifications to the crystalline integrity of the zeolite. Surface and chemical analyses performed using SEM/EDX and XPS revealed that increased silver content within the zeolite matrix hindered the diffusion of 5-FU molecules, particularly in the Ag7(5-FU) @Y system. As a consequence, this formulation exhibited a greater accumulation of 5-FU at the external surface, but a reduced total drug loading when compared to systems containing lower silver concentrations. Antimicrobial evaluations demonstrated that the observed antibacterial performance resulted from a synergistic interaction between Ag^{+} ions and 5-FU within the dual loaded systems. Among the investigated formulations, Ag4(5-FU) @Y provided the most favorable compromise between efficient drug incorporation, appropriate silver content, and enhanced antibacterial efficacy. These results indicate that combinations involving 5-FU@Y with Ag4Y or Ag4(5-FU) @Y may substantially improve antineoplastic activity, highlighting the potential of these systems for advanced cancer therapeutic applications [21]. In 2024, Dernaika et al. examined the suitability of zeolitic materials as carriers for pharmaceutical delivery, with particular emphasis on cannabidiol (CBD). The efficiency of CBD incorporation and its release behavior from the zeolite framework were investigated through in vitro dissolution studies conducted in simulated gastric and intestinal media. The results demonstrated a high loading efficiency, with approximately 73.5% of CBD successfully encapsulated within the zeolite particles.

Structural integrity of the USY zeolite following drug incorporation was verified by X-ray diffraction (XRD), which showed no detectable alterations to the crystalline framework. Additional characterization using dynamic light scattering (DLS) and nitrogen adsorption analyses further confirmed the effective integration of CBD into the zeolitic matrix. Comparative dissolution experiments revealed that the CBD-loaded zeolite system exhibited markedly enhanced release kinetics in both simulated environments. Within 30 minutes, CBD release reached 67.8% in gastric conditions (pH 1.8) and 62.6% in intestinal conditions (pH 6.8). By comparison, commercially available CBD capsules achieved significantly lower dissolution values of 43.6% and 38.4%, respectively. These findings underscore the promise of zeolites as efficient drug delivery platforms, particularly for poorly bioavailable compounds such as CBD. The observed improvement in dissolution performance suggests that zeolitic carriers may enhance drug absorption and therapeutic effectiveness, offering new opportunities for advanced pharmaceutical formulation strategies targeting low-solubility drugs [22]. In 2025, Eldeeb et al. investigated the performance of a zeolite A/chitosan composite as a pH-responsive carrier for the encapsulation and controlled release of ibuprofen within gastrointestinal environments. The study focused on assessing the influence of pH on drug release efficiency, reflecting the growing interest in targeted delivery systems with stimuli-responsive behavior. To this end, a zeolite A/chitosan (ZA/CS) hybrid material was synthesized and characterized as a delivery platform for ibuprofen, selected as a representative non-steroidal anti-inflammatory drug. The evaluation included determination of drug loading capacity, release behavior under simulated gastrointestinal conditions, and cytotoxicity to assess the suitability of the composite for biomedical use. The ZA/CS system demonstrated an exceptionally high drug loading content of 1989.13 mg/g, accompanied by an entrapment efficiency of 99.88%, indicating nearly complete retention of the incorporated drug. Release studies revealed a sustained and nearly linear ibuprofen release profile in simulated gastrointestinal media. Under gastric conditions, approximately 55% of the drug was released within the first two hours. To elucidate the release mechanism, the experimental data were analyzed using seven kinetic models, among which the Ritger Peppas model provided the best fit.

The calculated diffusion exponent values were 0.863 at pH 1.2 and 0.981 at pH 7.4, suggesting that the release process is governed by anomalous (non-Fickian) diffusion involving both molecular diffusion and polymer relaxation mechanisms. Furthermore, biocompatibility assessments conducted using the MTT assay confirmed that the ZA/CS composite exhibited no cytotoxic effects, supporting its safety for potential therapeutic applications. Collectively, these findings highlight the promise of the ZA/CS composite as an effective pH-sensitive drug delivery platform, particularly for pharmaceuticals such as ibuprofen that require controlled and site-specific release to enhance therapeutic efficacy while reducing adverse effects [23]. Recent progress in the design of zeolite-based platforms for controlled pharmaceutical release, as demonstrated by Grandprix Kadja et al, showcase their enhanced drug loading capacity, tailored release profiles, and biocompatibility. Zeolites can encapsulate substantial amounts of drugs, enabling improved bioavailability, especially for poorly soluble medications. Their ion-exchange properties allow for stimulus responsive release, making them suitable for targeted therapies like cancer treatment and anti-inflammatory drug delivery. Additionally, innovative formulation techniques, including composites with polymers, further enhance their effectiveness. Ongoing research aims to optimize zeolite synthesis and characterize their interactions with various drugs, positioning zeolites as promising candidates in modern pharmacotherapy [17]. Consequently, zeolitic materials offer promising strategies to improve the efficiency and precision of drug delivery platforms. Nevertheless, additional investigations are required to refine their application and to evaluate their long-term safety profiles comprehensively.

Section II: Layered Double Hydroxides (LDH)

1. History of LDH

Layered double hydroxides (LDHs), also known as hydrotalcite-like compounds or anionic clays [24], represent an important class of lamellar inorganic materials whose history dates back to the discovery of the natural mineral hydrotalcite ($Mg_6Al_2(OH)_{16}CO_3\ 4H_2O$) by Hochstetter in 1842. Despite this early identification, LDHs did not attract significant scientific attention until the mid-20th century, when Feitknecht and co-workers systematically investigated their formation, crystal

chemistry, and anion exchange behavior. In the 1960s and 1970s, the pioneering work of Allmann and Taylor provided detailed structural models based on X-ray diffraction studies, firmly establishing LDHs as a distinct family of materials derived from the brucite structure. Since the 1990s, advances in materials chemistry and nanotechnology have driven extensive research into LDHs due to their compositional flexibility, structural tunability, and multifunctional properties, leading to widespread applications in catalysis, environmental remediation, energy conversion and storage, and biomedicine [25].

2. Structure of layered double hydroxides

Layered double hydroxides (LDHs) possess a structure derived from brucite, $Mg(OH)_2$, in which divalent metal cations (M^{2+}) located in octahedral coordination sites are partially replaced by trivalent metal cations (M^{3+}). This partial substitution produces positively charged metal hydroxide layers described by the general formula; $[M^{2+}_{x-1}M^{3+}_{x}(OH)_2]^{x+}$. Charge neutrality is maintained through the incorporation of exchangeable interlayer anions (A^{n-}), such as carbonate, nitrate, chloride, or organic species, together with interlayer water molecules, yielding the overall composition $[M^{2+}_{x-1}M^{3+}_{x}(OH)_2]^{x+}$ $[A^{n-}_{x/n}]$ mH_2O. The parameter x, defined as the molar fraction of trivalent cations relative to the total metal content, typically falls within the range of 0.2 to 0.4 [26]. The hydroxide layers consist of edge sharing MO_6 octahedra arranged in a two-dimensional framework, while the interlayer region is stabilized by electrostatic attractions, hydrogen bonding, and van der Waals interactions. A key characteristic of LDHs is their high degree of structural flexibility, arising from the wide range of possible metal cation combinations, tunable M^{2+}/M^{3+} ratio commonly between 2 and 6 in the synthesized materials and the capacity to accommodate a diverse array of inorganic and organic anions within the interlayer space [27]. These features, together with high anion exchange capacity, large specific surface area, adjustable acid-base properties, and good thermal stability, underpin the broad applicability of LDHs in fields such as catalysis, adsorption, energy storage, drug delivery, and environmental remediation [28]. Furthermore, LDHs exhibit a well-known "memory effect", whereby thermal decomposition of the layered structure into mixed metal oxides can be reversed upon rehydration in the presence of appropriate anions, enabling reconstruction of the original lamellar structure and offering additional opportunities for post synthetic modification and functionalization [29].

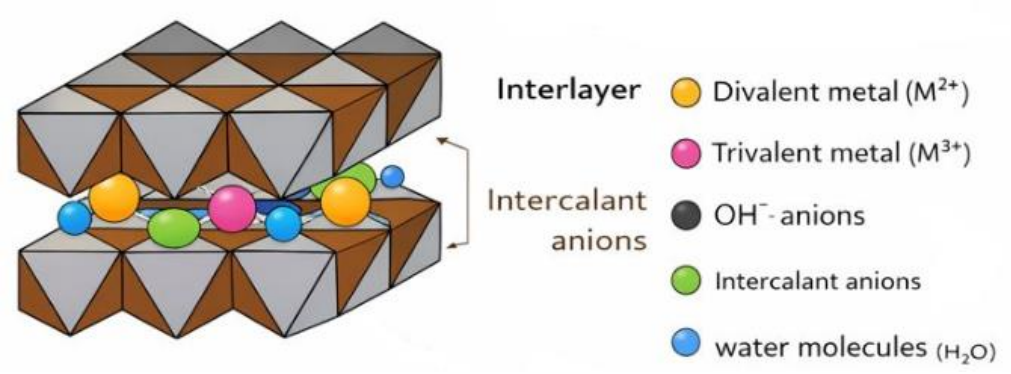


Figure 2: The structure of layered double hydroxides [30].

3. Synthesis methods

Layered double hydroxides (LDHs) are synthesized through various techniques that allow control over composition, crystallinity, particle size, morphology, and interlayer anions. The most common methods include co-precipitation, urea hydrolysis, hydrothermal/solvothermal synthesis, anion exchange, reconstruction (memory effect), and emerging approaches like mechanochemical or electrodeposition. These methods exploit the flexible structure of LDHs, enabling tuning for applications in catalysis, drug delivery, adsorption, and energy storage.

3.1 Co-precipitation

Co-precipitation is the most widely employed method for the synthesis of layered double hydroxides (LDHs) owing to its simplicity, cost effectiveness, compositional flexibility, and suitability for large scale production. In this method, aqueous solutions containing divalent M^{2+} and trivalent M^{3+} metal salts in a predetermined molar ratio are precipitated under alkaline conditions in the presence of hydroxide ions and, in most cases, a source of interlayer anions. Depending on the mode of pH control during precipitation, the coprecipitation method can be classified into two main approaches: coprecipitation at constant pH and coprecipitation at variable pH [28, 31].

3.2 Sol-gel method

The sol-gel method is a cost effective and straightforward technique that offers excellent homogeneity due to the molecular level mixing of precursors. The initial step in the sol-gel technique involves dispersing the starting materials, typically metal nitrates, in deionized water. A citric acid solution is subsequently introduced to the mixture and stirred for approximately one hour at a specified temperature. Following this, an ethylene glycol solution is added, and stirring is continued at an elevated temperature. During this phase, solvents evaporate, causing the mixture to transition from a sol to a gel state. The resulting precursor gel is then dried at temperatures exceeding 100 °C for about one day. The mixed metal oxides obtained are further heated at 650°C for approximately four hours. Finally, layered double hydroxides (LDHs) are synthesized by reconstituting the mixed metal oxide powders in deionized water at an elevated temperature for about four hours. LDHs produced via the sol-gel method exhibit high specific surface areas, superior homogeneity, and enhanced purity. Additionally, the method is characterized by its low processing temperatures, high efficiency, and simplicity [29].

3.3 Ion exchange method

The ion exchange technique offers an effective approach for incorporating anionic species into the interlayer galleries of layered double hydroxides. This method is based on the principle of replacing existing interlayer anions with other anionic species through exchange reactions. The procedure involves suspending precursor LDHs, typically containing weakly bound anions such as nitrate or chloride, in aqueous solutions containing the desired exchangeable anionic species. The suspension is stirred continuously at room or elevated temperature for several hours to facilitate the exchange process. Subsequently, the solid precipitate is collected by filtration, washed multiple times with deionized water to remove residual ions, and dried in an oven, typically overnight. The interlayer region may also contain water molecules, referred to as the interlayer water domain, where hydrogen bonding between water molecules and the inorganic hydroxide layers play a crucial role in organizing the interlayer structure. The high anion exchange capacity of LDH materials facilitates the replacement of native interlayer anions with incoming functional anions, making this method particularly suitable and readily implementable for preparing LDH

based functional materials with desired interlayer compositions. This technique is advantageous due to its mild reaction conditions, preservation of the layered structure, and versatility in accommodating various organic and inorganic anionic guests [32].

3.4 Homogenous precipitation method

The urea hydrolysis method, also known as homogeneous precipitation [29], represents an alternative approach for LDH synthesis. The high solubility of urea enables precise control over the hydrolysis rate through temperature adjustment, making it an effective precipitating agent for LDH preparation. This method facilitates the synthesis of LDHs with desirable crystalline structures, large hexagonal platelet morphologies, and uniform distribution of metal cations throughout the lattice. The molar ratio of urea to metal ions is a critical parameter that significantly influences the quality of the synthesized LDHs. For instance, comparative studies on Ni-MgO-Al_2O_3 catalysts derived from LDHs using co-precipitation, urea hydrolysis, and wet impregnation methods have demonstrated that catalysts prepared via urea hydrolysis exhibit superior metal support interactions, smaller nickel particle sizes, enhanced resistance to coke formation, and higher basicity, resulting in improved catalytic performance with toluene conversion rates reaching approximately eighty-five %. LDHs synthesized through urea hydrolysis are characterized by uniform particle size, well-defined morphology, and high crystallinity, attributes that render this method particularly attractive for various practical applications including catalysis and functional material development [33].

3.5 Manual grinding method

The manual grinding method is a simple and rapid technique for the synthesis of layered double hydroxides (LDHs). In this approach, metal salts are manually ground with sodium hydroxide pellets in a mortar, leading to the formation of a homogeneous paste. The resulting material is then thoroughly washed with deionized water to remove residual ions and subsequently dried in a vacuum oven. LDHs synthesized by the manual grinding method exhibit physicochemical characteristics comparable to those obtained via the conventional co-precipitation method. This technique can also be employed for the preparation of magnetic LDHs by grinding iron containing metal salts with sodium hydroxide pellets. A key advantage of the manual grinding method is that

it does not require heating or refluxing steps, a carbon dioxide free atmosphere, or the use of solvents, making it an energy efficient and environmentally friendly synthesis route [29].

3.6 Salt oxides method

In this method, a metal salt solution is slowly mixed with another metal oxide, followed by vigorous agitation at a specific temperature to obtain layered double hydroxides (LDHs). For instance, Mg_2Al-CO_3-LDHs were produced using magnesium hydroxide, aluminum nitrate, and light magnesium carbonate as raw materials, resulting in average particle sizes ranging from 202 nm to 334 nm. The structure of chromium LDH synthesized through various methods was characterized, revealing that the LDHs obtained via the salt-oxide method exhibited lower ordering compared to those made through co-precipitation. This method requires precise control of the solution pH during the mixing of metal salt solutions, as it significantly impacts the formation and properties of the LDHs. Additionally, the salt oxide method is selective for types of LDHs and necessitates extreme acidic or basic conditions, often yielding layered double hydroxides with relatively poor stability [33].

3.7 Hydrothermal and solvothermal method

The hydrothermal synthesis method shares similarities with co-precipitation, wherein aqueous solutions containing M^{2+} and M^{3+} metal salts are added dropwise to a base solution under vigorous stirring at room temperature, maintaining a pH range of 8 to 10. The resulting suspension is subsequently transferred into a Teflon-lined autoclave and heated at temperatures between 100 to 180°C for 10 to 48 hours, depending on the metal ions employed. The precipitated solid is collected by centrifugation, thoroughly washed with ethanol and deionized water, and dried overnight in an oven. Compared to co-precipitation, the hydrothermal technique produces LDHs with more uniform morphology and enhanced crystallinity. The solvothermal method is analogous but employs organic solvents (such as alcohols or glycerol) instead of water, with reactions conducted in closed systems at temperatures and pressures above the solvent's boiling point.

Both hydrothermal and solvothermal approaches are recognized for their advantages in nanomaterial synthesis, including lower energy consumption, reduced processing temperatures, the minimal environmental impact, and the ability to achieve high degrees of crystallinity. These features make them attractive green synthesis routes for advanced materials [32].

3.8 Electrocoagulation method

The electrocoagulation technique represents an in-situ synthesis approach for layered double hydroxides (LDH) that confers multiple advantages. Notably, it obviates the requirement for solid-liquid phase separation and substantially reduces the duration needed to complete the synthesis. Moreover, the process eliminates the use of pH adjusting agents or additional chemical reagents. A key feature of the electrocoagulation method is the capacity for polarity control, which enables precise tuning of the divalent / trivalent molar ratio and, consequently, broadens the scope of LDH applications. In the experimental setup, magnesium and aluminum electrodes were immersed in a glass reactor containing an aqueous sodium chloride solution, with continuous agitation provided by a magnetic stirrer. The electrodes were connected to a direct current (DC) power supply. Upon completion of the electrocoagulation process, the resulting suspension was filtered, and the obtained solid was dried in an oven at 105 °C for 2 hours to yield the synthesized LDH [29].

3.9 Reconstruction of LDHs

The reconstruction method is based on a unique characteristic of layered double hydroxides (LDHs), commonly referred to as the structural memory effect. In this approach, the pristine LDH is first subjected to calcination, which results in the elimination of interlayer water molecules, intercalated anions, and hydroxyl groups, leading to the formation of a mixed metal oxide phase. Upon subsequent exposure of the calcined material to an aqueous solution containing the desired guest anions, rehydration occurs. During this process, water molecules restore the hydroxylated metal layers, while additional water molecules and anions are incorporated into the interlayer region, thereby reconstructing the original layered structure. The efficiency of the memory effect is strongly influenced by the chemical composition of the LDH layers and the calcination temperature, with higher calcination temperatures generally leading to a partial or complete loss

of this effect. The reconstruction method is particularly advantageous for the intercalation of large organic anions, as it minimizes competition between counter ions originating from precursor metal salts and the target intercalating species. However, a major limitation of this method is that it often results in LDH products with low crystallinity or partially amorphous structures [34].

3.10 Microwave assisted method

The synthesis of layered double hydroxides (LDHs) using microwave (MW) irradiation is a method that accelerates the aging process to approximately 15 to 60 minutes. This MW assisted aging technique enables the production of homogeneous particles, which are generally smaller than those synthesized through reflux aging. High surface area Mg-Al-LDHs can be achieved by combining Mg $(OH)_2$ and Al $(OH)_3$ in a molar ratio of 2:1. The product obtained from MW heating was analyzed using X-ray diffraction (XRD). The powder product, following the drying process and subsequent hydrothermal treatment, exhibited distinct XRD peaks corresponding to Mg-Al-LDH, while the slurry state product prior to drying did not display any detectable crystalline structure [27].

3.11 Non aqueous precipitation method for small LDHs

Layered double hydroxides (LDH) with reduced particle size and lower average dimensions demonstrate superior performance compared to conventional LDH exhibiting larger average particle sizes. Small particle LDH can be synthesized via a non-aqueous precipitation method. This approach entails the dropwise addition of a methanolic solution containing metal nitrates to a sodium hydroxide solution in methanol. The resulting mixture is vigorously stirred, and the precipitated slurry is subsequently recovered by centrifugation. The collected material is then subjected to hydrothermal treatment in a Teflon lined autoclave. Following hydrothermal processing, the final slurry is redispersed in deionized water and allowed to stand at room temperature. When manually dispersed LDH aggregates in aqueous suspension undergo hydrothermal treatment, it promotes the detachment of individual LDH particles from the aggregates. This hydrothermal step supplies the necessary energy to facilitate particle delamination and detachment.

The resulting small particle LDH system exhibits enhanced efficiency in drug delivery applications relative to LDH of conventional particle size. Employing this method enables the preparation of a well-dispersed, stable aqueous suspension of LDH [29].

4. Biomedical applications of layered double hydroxides

Layered double hydroxides (LDHs) have emerged as versatile nanomaterials with diverse biomedical applications due to their unique properties including biocompatibility, tunable composition, high anion exchange capacity, pH responsive behavior, and ability to protect intercalated molecules [35].

4.1 Drug delivery systems

Layered double hydroxides (LDHs), have emerged as significant carriers in drug delivery systems due to their distinctive structural characteristics and favorable biocompatibility. The lamellar architecture of LDHs provides a high surface to volume ratio, facilitating the intercalation of a diverse array of therapeutic agents. This capability enables a sustained and controlled release of drugs at targeted sites, thereby minimizing adverse effects and enhancing bioavailability. The synthesis of LDHs is typically achieved through several established methods, including co-precipitation, ion exchange, and sol-gel techniques, all of which yield high loading efficiencies and cater to various applications. Numerous studies have reported the successful encapsulation of a wide range of therapeutics such as anti-inflammatory agents, antibiotics, and anticancer drugs demonstrating not only improvements in solubility and stability but also enhanced therapeutic efficacy. Notably, LDHs have been investigated for application in cancer treatment, where their pH sensitive properties allow for drug release in response to the acidic microenvironment of tumors. Additionally, their positive surface charge significantly enhances ocular drug delivery by prolonging residence time on the negatively charged surfaces of the cornea and conjunctiva. Furthermore, LDHs exhibit potential in gene delivery, enabling the transportation of negatively charged nucleic acids to specific cellular sites. Nonetheless, several challenges persist, including potential toxicity, difficulties in achieving targeted delivery, and the degradation of LDHs in acidic conditions, which may limit their effectiveness in oral drug delivery.

Ongoing research endeavors aim to enhance the functionality of LDHs through surface modifications and the development of hybrid systems, thereby improving their performance as drug delivery vehicles. In conclusion, LDHs constitute a versatile and promising platform for advanced drug delivery applications, positioned to substantially improve therapeutic outcomes across a wide range of biomedical contexts [29].

4.2 Antimicrobial applications

The rapid emergence of multidrug-resistant bacterial strains has positioned layered double hydroxides (LDHs) as promising nanocarriers for antimicrobial drug delivery, offering critical advantages in reducing therapeutic dosages, minimizing adverse effects, and combating antibiotic resistance. Various studies have demonstrated that LDH-based systems, particularly those utilizing Mg-Al-LDH and Zn-Al-LDH matrices, can successfully encapsulate diverse antimicrobial agents including vancomycin, norfloxacin, penicillin G, isoniazid, cefotaxime, cefadroxil, and natural compounds like mandelic acid and berberine through co-precipitation, anion exchange, or reconstruction methods. These systems exhibit pH dependent sustained release profiles, typically showing controlled drug release over extended periods (ranging from hours to days) compared to rapid release from free drugs, with release kinetics following zero order, pseudo second order, or Bhaskar models depending on pH conditions. Significantly, LDH-drug complexes demonstrate enhanced antimicrobial efficacy with minimum inhibitory concentrations often two to three-fold lower than free drugs, attributed to synergistic effects between the antimicrobial agent and metal ions (particularly Zn^{2+}) present in the LDH structure, improved drug stability, and sustained bioavailability at infection sites. The co-precipitation method generally provides superior results compared to other synthesis techniques due to stronger drug carrier interactions and more homogeneous chemical characteristics, resulting in better controlled release profiles. Comprehensive cytotoxicity evaluations across multiple studies confirm the biocompatibility of these systems with cell viabilities exceeding 80% and biocompatibility three-fold better than isolated drugs, while antimicrobial activity studies demonstrate effectiveness against both Gram-positive and Gram-negative bacteria, including resistant strains, with prolonged antibacterial action lasting up to ten days.

These LDH based antimicrobial delivery platforms thus represent a highly promising strategy for enhancing therapeutic efficacy while reducing drug related toxicity and addressing the critical challenge of antibiotic resistance [30].

Section III: Computational modeling approaches

1. Computational chemistry

Computational chemistry is a multidisciplinary scientific discipline that applies numerical and algorithmic techniques to the study of chemical systems, drawing upon foundational principles from chemistry, physics, and computer science. By combining theoretical models with advanced computational tools, this field enables the investigation of molecular structures, spectroscopic features, chemical reactivity, enzyme-ligand interactions, and a broad range of molecular and physicochemical properties. Common computational approaches include ab initio methods, which derive molecular characteristics through first principles solutions of the Schrödinger equation; semi-empirical techniques, which reduce computational complexity by incorporating experimentally derived parameters; and molecular mechanics, which employs classical force fields to describe atomic and molecular behavior. Among these methods, density functional theory (DFT) is particularly appropriate for the present study, as it allows accurate analysis of structural properties, electronic interactions, and vibrational behavior [36]. In addition, molecular docking simulations are used to estimate interaction energies between biologically relevant targets, such as proteins, and potential therapeutic compounds, thereby offering valuable insight into underlying biological mechanisms [37].

1.1 Density functional theory (DFT)

Density Functional Theory (DFT) is a sophisticated quantum mechanical modeling approach used to investigate the electronic structure of many body systems, particularly in chemistry and materials science. At its core, DFT simplifies the complex interactions of electrons by focusing on electron density rather than wave functions, allowing for computationally feasible calculations of various molecular properties [38].

Using DFT, researchers can accurately calculate a wide range of parameters, including the energies of the Highest Occupied Molecular Orbital (HOMO) and the Lowest Unoccupied Molecular Orbital (LUMO), energy gaps (ΔE) (equation a), chemical hardness η (equation b), chemical softness δ (equation c), lipophilicity log(p), and chemical potential Cp (equation d) [39].

$\Delta E = E_{LUMO} - E_{HOMO}$ ..... equation (a)

$$\eta = \frac{1}{2}\Delta E \text{ ..... equation (b)}$$

$$\delta = \frac{1}{\eta} \text{ ..... equation (c)}$$

$$Cp = \frac{E\,(HOMO) - E(LUMO)}{2} \text{ ..... equation (d)}$$

These calculations play a crucial role in understanding the stability, reactivity, and electronic properties of compounds, making DFT an essential tool for predicting behavior in chemical reactions and material properties [40]. The choice of DFT over other computational methods, such as Hartree Fock (HF) or semi empirical techniques, is often motivated by its balance between accuracy and computational efficiency. DFT incorporates electron correlation effects more effectively than HF, which neglects these interactions, thereby providing a more reliable description of molecular systems [36]. Additionally, DFT simulations allow for the exploration of larger and more complex systems that would be computationally prohibitive with more traditional methods, thereby expanding the scope of theoretical predictions and facilitating advancements in various fields, including drug design [41-43], catalysis [44], and materials development [45]. Overall, DFT serves as a cornerstone for modern computational chemistry, offering valuable insights and predictive capabilities that are vital for both theoretical research and practical applications [46].

1.2 Molecular docking study

Molecular docking is a computational approach commonly used to estimate how a small molecule associates with a biological macromolecule, most often a protein or enzyme, by identifying the most energetically favorable binding configuration.

By simulating ligand-receptor complex formation, this technique provides valuable insights into binding strength and site-specific interactions that govern molecular recognition in biological systems. Molecular docking enables the determination of key descriptors, including binding free energy, interaction patterns, and the three-dimensional positioning of the ligand within the target molecule's active site [47]. Molecular docking is a key component of modern drug discovery and development, as it enables the computational identification of promising therapeutic candidates by virtually assessing small molecules against specific protein targets. Its widespread adoption is largely due to its ability to rapidly and systematically screen extensive chemical libraries, thereby supporting lead identification, optimization, and structure guided drug design. Compared to experimental techniques, docking simulations can quickly provide valuable information about how well a ligand fits into a receptor's active site, thus guiding further experimental studies. Additionally, advancements in docking algorithms and scoring functions have enhanced the accuracy of predictions, allowing researchers to model complex interactions and explore the dynamics of ligand-receptor relationships. Overall, molecular docking serves as an essential component of modern pharmacology, offering researchers a means to evaluate and refine potential therapeutic agents effectively [48]. The molecular docking simulation was conducted in three sequential steps; first, the preparation of the ligand or active compound, second, the preparation of the target protein and definition of the grid box, and third, the docking simulation [39].

1.2.1 Preparation of active compound (ligand)

The process of ligand preparation is crucial for successful molecular docking, as it involves transforming 2D chemical structures into corresponding low energy 3D geometries. This process begins with the acquisition of the two-dimensional structure of the ligand, which can be sourced from databases like PubChem or created manually using molecular editing software, such as ChemDraw [49]. Once the 2D structure is established, it is converted into a three-dimensional representation by assigning spatial coordinates to all constituent atoms [50]. This conversion requires algorithms to predict bond angles, bond lengths, and overall molecular geometry, adhering to established chemical rules and force fields. After generating the initial 3D structure, energy minimization is performed to optimize the geometry and identify the lowest energy conformation.

Following the energy minimization step, hydrogen atoms are added if they are absent, ensuring that the ligand is fully hydrogenated for accurate docking simulations [48]. Finally, the prepared ligand is converted into the appropriate file format required by the docking software, such as PDB for AutoDock, facilitating seamless integration into the docking workflow [49].

1.2.2 Preparation of protein (receptor) and the grid box

The preparation of the receptor is an essential step that involves several elementary and indispensable procedures to refine the protein structure for accurate docking simulations. The protein structure, retrieved from the Protein Data Bank (PDB), undergoes systematic refinement that includes removing water molecules that may interfere with ligand binding, filling in missing loops and side chains to complete the protein structure, deleting alternate conformations of residues that result from crystallographic ambiguity, adding hydrogen atoms which are typically absent in experimental structures, and inserting missing atoms in incomplete residues to ensure structural integrity. These preparation and refinement procedures are essential for generating a structurally reliable and chemically complete receptor model. Once the protein preparation stage is completed, a receptor grid is constructed to accurately define the spatial boundaries and location of the binding region. This grid delineates the receptor's active site, specifying the area where interactions between the ligand and surrounding amino acid residues are expected to occur, thereby ensuring precise simulation of ligand-receptor binding events [50].

1.2.3 Molecular docking study

Molecular docking was conducted to predict the interactions between the active compound and the enzyme, as well as the binding affinities of the ligands at the enzyme's active site [51]. The results were visualized using ligand interaction tools [49].

2. Advanced modeling and optimization techniques

In the realm of data analysis and optimization, various advanced modeling techniques play a pivotal role in enhancing decision making processes and improving outcomes to explores four significant methodologies [52]:

Response Surface Methodology (RSM), Artificial Neural Networks (ANN), Adaptive Neuro-Fuzzy Inference System (ANFIS) [53], and Genetic Algorithms (GA) [54]. Each of these approaches offers unique strengths in handling complex, nonlinear relationships and optimizing processes across diverse fields such as engineering [55], finance, and healthcare [56]. Understanding these techniques equips practitioners with the tools needed to tackle complex problems and drive innovation.

2.1 RSM: Response Surface Methodology

Response Surface Methodology (RSM) comprises a set of mathematical and statistical tools employed to develop predictive models and analyze systems in which a measured response is affected by multiple influencing factors. This approach aims to describe and quantify the relationships between the response variable and the corresponding independent variables. The central objective of RSM is to determine optimal conditions, such as maximum yield or improved performance, by systematically evaluating variable interactions and identifying the most favorable combination of operating parameters. Widely applied in experimental design and process optimization, RSM provides a structured framework for assessing how variations in input factors influence the output response and for locating conditions that lead to optimal system performance [55].

2.2 ANN: Artificial Neural Networks

An Artificial Neural Network (ANN) is a computational paradigm modeled after the functional principles of biological neural systems, developed to process information, identify patterns, and solve complex tasks through data driven learning. The architecture of an ANN is generally organized into three essential components: an input stage, one or more intermediate processing stages, and an output stage [57]. The input stage serves as the interface through which raw data are introduced into the network, with each node corresponding to an individual feature; in the illustrated configuration, K nodes receive the initial dataset for further processing. Between the input and output stages, the hidden processing layer performs the core computational operations by transforming incoming information through interconnected weighted pathways.

In the presented model, this layer consists of L processing units that receive signals from the input nodes via weighted links represented by W_{ij}, where each weight quantifies the influence of a specific input signal. These intermediate units apply nonlinear activation functions, enabling the network to capture complex relationships and dependencies that extend beyond linear representations. The final stage of the network is the output layer, which generates predictions or classifications based on the processed information received from the hidden layer.

This layer contains M output nodes connected through weights denoted as W_{jk}, each producing a response corresponding to the modeled outcome. Data propagation within the ANN follows a forward progression: inputs are weighted, aggregated with bias terms, transformed through activation functions, and transmitted sequentially until the final output is obtained [58]. Model training is achieved through an optimization procedure known as backpropagation, where discrepancies between predicted and reference values are computed and transmitted backward through the network. This iterative adjustment of connection weights minimizes prediction error over successive training cycles, ultimately allowing the network to accurately map input features to desired outputs for the specified problem [57].

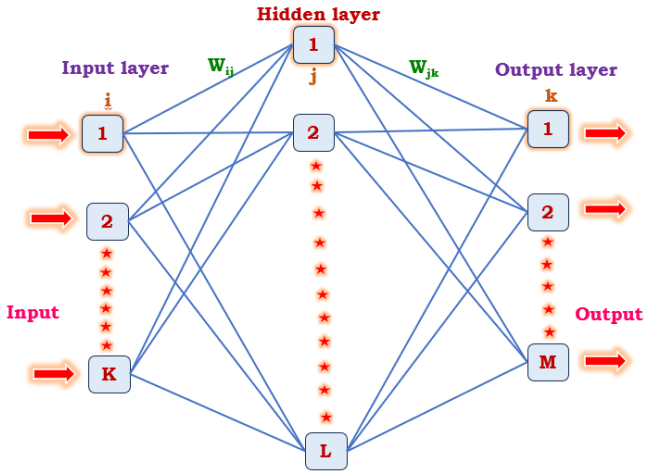


Figure 3: general structure of an Artificial Neural Network (ANN) in a three-layered Multilayer Perceptron (MLP) form [58].

2.3 ANFIS: Adaptive Neuro-Fuzzy Inference system

The Adaptive Neuro-Fuzzy Inference System (ANFIS) represents an advanced artificial intelligence technique designed to perform highly accurate predictions [59] in engineering applications by synergistically integrating two powerful methodologies: Artificial Neural Networks (ANN) and Fuzzy Inference Systems (FIS). By combining the learning capabilities of neural networks with the reasoning abilities of fuzzy logic, the ANFIS model effectively captures the complexities and nonlinearities inherent in sophisticated processes, resulting in a superior predictive framework. This hybrid approach has been extensively investigated and successfully applied across numerous environmental engineering applications, demonstrating its versatility and effectiveness in handling complex prediction tasks. The ANFIS architecture operates through a two-phase mechanism that leverages the distinctive advantages of both constituent technologies. Initially, the system undergoes a training phase similar to conventional ANNs, during which appropriate algorithms establish meaningful connections and relationships among the instantaneous data points within the entire dataset, enabling the model to learn underlying patterns and dependencies. Once trained, the system transitions to function as a FIS, utilizing fuzzy logic rules to make inferences and predictions based on the learned relationships [58]. This dual integration creates a cohesive framework that maximizes the computational efficiency of neural networks while incorporating the interpretability and human like reasoning of fuzzy systems. The development of an ANFIS model involves several distinct stages, including architecture construction [60], parameter selection, and system training, each requiring careful consideration and optimization. Critical decisions during model development include selecting appropriate membership functions and their associated parameters, which define how input variables are mapped to fuzzy sets, as well as partitioning both input and output data into rule-based segments that form the foundation of the fuzzy inference process. The ANFIS methodology streamlines the training procedure by incorporating widely used clustering algorithms, such as subtractive clustering or fuzzy c-means, which facilitate the systematic organization, classification, and structuring of input data into meaningful clusters, ultimately enhancing the model's ability to generalize and predict accurately across diverse conditions [58].

2.4 GA: Genetic Algorithms

As its name implies, the Genetic Algorithm (GA) is fundamentally based on Charles Darwin's theory of natural selection and evolution, representing the pioneering computational technique to employ multiple evolutionary operators simultaneously, including crossover, recombination, mutation, and selection. Each of these operators plays a critical and distinct role in the GA framework, contributing essential mechanisms for exploring solution spaces and resolving complex optimization problems. Unlike conventional optimization algorithms that typically process objective functions sequentially, GA possesses the unique capability to handle multiple complex objective functions in parallel, making it particularly powerful for multidimensional optimization challenges. Since its inception, GA has gained widespread popularity not only within biotechnology, where evolutionary concepts naturally align with biological systems, but also across diverse engineering disciplines including electrical, mechanical, civil, and aeronautical engineering, where optimization problems are prevalent and often highly complex. The Genetic Algorithm operates as a stochastic search technique that fundamentally adopts the principle of "survival of the fittest," systematically favoring superior solutions while eliminating poorly performing individuals from the population across successive generations. Because GA draws its inspiration directly from natural selection and reproductive processes observed in biological systems, the terminology used in GA closely mirrors biological concepts, including terms such as chromosomes, genes, population, fitness, reproduction, and generation. As reflected in natural biological evolution, the optimization processes within GA inherently involve randomness and probabilistic operations, introducing diversity and preventing premature convergence to suboptimal solutions. However, unlike uncontrolled natural evolution, genetic algorithm provides researchers with the flexibility to define and adjust the level of randomization through various parameters such as mutation rates, crossover probabilities, and selection pressure, thereby maintaining controlled stochasticity while systematically directing the search toward optimal or near the optimal solutions [61].

References

[1] H. Serati-nouri and al, "Biomedical applications of zeolite-based materials : A review," Mater. Sci. Eng. C, vol. 116, no. June, p. 111225, 2020.

doi: 10.1016/j.msec.2020.111225.

[2] T. Pandya and al, "Zeolite-based nanoparticles drug delivery systems in modern pharmaceutical research and environmental remediation," Heliyon, vol. 10, no. 16, p. e36417, 2024.

doi: 10.1016/j.heliyon.2024.e36417.

[3] K. Ito and al, "Further synthetic investigation of YNU-5 zeolite and its application as a solid acid catalyst for the MTO reaction," catalysis today, vol. 459, no. March, pp. 0–10, 2025.

doi: 10.1016/j.cattod.2025.115402.

[4] G. Pokuaa and al., "Characterization of chitosan / zeolite drug delivery composite and curcumin release kinetics in a simulated ph environment," Sci. African, vol. 28, no. February, p. e02668, 2025.

doi: 10.1016/j.sciaf.2025.e02668.

[5] N. Kordala and M. Wyszkowski, "Zeolite properties, methods of synthesis, and selected applications," molecules, vol. 29, 2024.

doi: 10.3390/molecules29051069.

[6] A. J. Wise and al, "Zero-order and prolonged release of atenolol from microporous FAU and BEA zeolites , and mesoporous MCM-41 : Experimental and theoretical investigations," J. Control. Release, vol. 327, no. March, pp. 140–149, 2020.

doi: 10.1016/j.jconrel.2020.07.027.

[7] J. Matusiak and al, “Zeolites and zeolite imidazolate frameworks on a quest to obtain the ideal biomaterial for biomedical applications : A review,” Mater. Today, vol. 67, no. August, pp. 495–517, 2023.

doi: 10.1016/j.mattod.2023.06.008.

[8] Z. B. Eken and al, “Effects of zeolite as a drug delivery system on cancer therapy : a systematic review,” molecules, vol. 26, 2021.

doi: 10.3390/molecules26206196.

[9] M. G. Rimoli and al., “Synthetic zeolites as a new tool for drug delivery,” Wiley InterScience ; Journal of Biomedical Materials Research Part A , 2007.

doi: 10.1002/jbm.a.31763.

[10] I. Marantos and al, “Zeolite formation and deposits,” Natural Zeolites Handbook, no. January 2012, 2018.

doi: 10.2174/978160805261511201010028.

[11] M. Fitriani and al, “Synthesis and characterization of zeolites from coal fly ash waste,” Indonesian Physical Review, vol. 08, no. 01, pp. 62–71, 2025.

doi: /10.29303/ip r.v8i1.370.

[12] Q. Lang and al, “Zeolites for the environment,” Green Carbon, vol. 2, no. 1, pp. 12–32, 2024.

doi: 10.1016/j.greenca.2024.02.007.

[13] H. E. Mgbemere and al, “Zeolite Synthesis, Characterisation and Application Areas: A Review,” Int. Res. J. Environ. Sci., vol. 6, no. 10, pp. 45–59, 2017.

[14] T. Derbe and al, “A short review on synthesis , characterization , and applications of zeolites,” Advances in Materials Science and Engineering; Hindawi, vol. 2021, 2021.

doi: 10.1155/2021/6637898.

[15] N. Salahudeen, "A review on zeolite : application , synthesis and effect of synthesis parameters on product properties," Chem. Africa, vol. 5, no. 6, pp. 1889–1906, 2022.

doi: 10.1007/s42250-022-00471-9.

[16] H. Serati-nouri and al, "Biomedical applications of zeolite-based materials : A review," Mater. Sci. Eng. C, vol. 116, no. February, p. 111225, 2020.

doi: 10.1016/j.msec.2020.111225.

[17] G. T. M. Kadja and al, "Recent advances in the utilization of zeolite-based materials for controlled drug delivery," Results Chem., vol. 5, no. March, p. 100910, 2023.

doi: 10.1016/j.rechem.2023.100910.

[18] S. Rahmani and al, "Application of synthetic nanozeolite sodalite in drug delivery," International Current Pharmaceutical Journal, vol. 5, no. May, pp. 55–58, 2016.

[19] A. Datt, "Applications of mesoporous silica and zeolites for drug delivery," PhD (Doctor of Philosophy) thesis, University of Iowa, 2012.

http://ir.uiowa.edu/etd/3442.

[20] K. K. Jain, "Chapter 1 an overview of drug delivery systems," Springer Science+Business Media, LLC, part of Springer Nature, vol. 2059. 2020.

doi: 10.1007/978-1-4939-9798-5_1.

[21] A. R. Bert and al, "Preliminary evaluation of zeolite-based platforms as potential dual drug delivery systems against microbial infections in the tumor microenvironment," Microporous and Mesoporous Materials, vol. 364, no. July 2023, 2024.

doi: 10.1016/j.micromeso.2023.112871.

[22] F. Dernaika and al, "Development and characterization of a zeolite based drug delivery system : Application to cannabidiol oral delivery," Heliyon, vol. 10, no. 17, p. e37373, 2024, doi: 10.1016/j.heliyon.2024.e37373.

[23] A. M. Eldeeb and al, "pH-responsive zeolite-A / chitosan nanocarrier for enhanced ibuprofen drug delivery in gastrointestinal systems," Int. J. Biol. Macromol., vol. 289, no. December 2024, p. 138879, 2025.

doi: 10.1016/j.ijbiomac.2024.138879.

[24] K. Imene and al., "Thermal treatment of Cu-doped hydrotalcite-like adsorbents for improved removal of methyl orange from water," Sep. Purif. Technol., vol. 365, no. March, p. 132656, 2025.

doi: 10.1016/j.seppur.2025.132656.

[25] T. Hu and al, "Layered double hydroxide-based nanomaterials for biomedical applications".

[26] S. Bahraminejad and al, "Synthesis and physicochemical characterization of Zn – Al layered double hydroxides (LDHs) as a delivery system for amphotericin B : In vitro and in silico antileishmanial study," Heliyon, vol. 9, 2023.

10.1016/j.heliyon.2023.e15308.

[27] J. Kameliya and al, "Layered double hydroxide materials: a review on their preparation, characterization, and applications," inorganics, vol. 11, 2023.

doi: 10.3390/ inorganics11030121.

[28] I. A. Abdallah and al, "Applications of layered double hydroxides in sample preparation : A review," Microchem. J., vol. 192, no. February, p. 108916, 2023.

doi: 10.1016/j.microc.2023.108916.

[29] V. K. A. Shirin and al, "Advanced drug delivery applications of layered double hydroxide," J. Control. Release, vol. 330, no. August 2020, pp. 398–426, 2021.

doi: 10.1016/j.jconrel.2020.12.041.

[30] L. Moreira and al., "Layered double hydroxides as promising excipients for drug delivery purposes," European Journal of Pharmaceutical Sciences, vol. 165, no. June, 2021.

doi: 10.1016/j.ejps.2021.105922.

[31] A. C. Bouali and al, "Layered double hydroxides (LDHs) as functional materials for the corrosion protection of aluminum alloys : A review," Appl. Mater. Today, vol. 21, p. 100857, 2020.

doi: 10.1016/j.apmt.2020.100857.

[32] A. V Karim and al, "Nanostructured modified layered double hydroxides (LDHs) -based catalysts : A review on synthesis , characterization , and applications in water remediation by advanced oxidation processes," Curr. Opin. Solid State Mater. Sci., vol. 26, no. 1, p. 100965, 2022.

doi: 10.1016/j.cossms.2021.100965.

[33] G. Liu and al, "Biochar / layered double hydroxides composites as catalysts for treatment of organic wastewater by advanced oxidation processes : A review," Environ. Res., vol. 234, no. July, p. 116534, 2023.

doi: 10.1016/j.envres.2023.116534.

[34] R. E. El-dessouky, "Layered double hydroxides-biopolymer nanocomposites for the controlled delivery of vitamins," The American University in Cairo School of Sciences and Engineering, 2016.

https://fount.aucegypt.edu/etds/245.

[35] J. Wen and al, "Recent advances in LDH-based nanosystems for cancer therapy," Mater. Des., vol. 198, p. 109298, 2021.

doi: 10.1016/j.matdes.2020.109298.

[36] M. E. Ayalew, "DFT studies on molecular structure , thermodynamics parameters , HOMO-LUMO and spectral analysis of pharmaceuticals compound quinoline (benzo [b] pyridine)," pp. 29–42, 2022.

doi: 10.4236/jbpc.2022.133003.

[37] A. M. Abbas and al, "Design , synthesis , anti-inflammatory activity , dft modeling and docking study of new ibuprofen derivatives," Int. J. Mol. Sci, vol. 25, no. March, 2024.

doi: 10.3390/ijms25063558.

[38] H. Guan and al, "Application of Density Functional Theory to Molecular Engineering of Pharmaceutical Formulations," Int. J. Mol. Sci., vol. 26. 3262, 2025.

doi: 10.3390/ijms26073262.

[39] O. E. Oyeneyin and al, "Structural modification of ibuprofen as new nsaids via dft , molecular docking and pharmacokinetics studies," Int. J. Adv. Eng. Pure Sci., vol. 33, no. 4, pp. 614–626, 2021.

doi: 10.7240/jeps.928422.

[40] M. Khadka and al, "Spectroscopic , quantum chemical , and topological calculations of the phenylephrine molecule using density functional theory," nature portfolio; Scientific Reports, vol. 15, no. 208, pp. 1–18, 2025.

doi: 10.1038/s41598-024-81633-2.

[41] R. Xiao and al, "Thermodynamic and kinetic study of ibuprofen with hydroxyl radical : a density functional theory approach," International Journal of Quantum Chemistry, pp. 1–10, 2013.

doi: 10.1002/qua.24518.

[42] K. P. S. Hussan and al, "Synthesis , spectroscopic , chemical reactivity , molecular docking , dft calculations and in-vitro anticancer activity studies of a novel ionic liquid ; metforminium ibuprofenate," Journal of Molecular Liquids, vol. 364, 2022.

doi: 10.1016/j.molliq.2022.120046.

[43] M. L. Vueba and al, "Conformational stability of ibuprofen : assessed by dft calculations and optical vibrational spectroscopy," Journal of Pharmaceutical Sciences, vol. 97, no. 2, pp. 845–859, 2008.

doi: 10.1002/jps.

[44] V. Butera, "Density functional theory methods applied to homogeneous and heterogeneous catalysis: a short review and a practical user guide," Phys. Chem., vol. 26, pp. 7950–7970, 2024.

doi: 10.1039/d4cp00266k.

[45] T. Hickel, "Density functional theory in materials science," WIREs Comput Mol Sci, vol. 3, no. October2013, pp. 438–448, 2013.

doi: 10.1002/wcms.1125.

[46] M. Tayyab and al, "Next-generation materials discovery using dft : functional innovation , solar energy , catalysis , and eco toxicity modelling," Sch J Eng Tech, vol. 9523, no. 7, pp. 454–486, 2025.

doi: 10.36347/sjet.2025.v13i07.003.

[47] M. Shah and al, "Computational transformation in drug discovery : A comprehensive study on molecular docking and quantitative structure activity relationship (QSAR)," Intell. Pharm., vol. 2, no. 5, pp. 589–595, 2024.

doi: 10.1016/j.ipha.2024.03.001.

[48] H. K. Nivatya and al, "Assessing molecular docking tools : understanding drug discovery and design," Future Journal of Pharmaceutical Sciences, vol. 11, 2025.

doi: 10.1186/s43094-025-00862-y.

[49] F. Azam and al, "NSAIDs as potential treatment option for preventing amyloid β toxicity in Alzheimer ' s disease : an investigation by docking , molecular dynamics , and dft studies," J. Biomol. Struct. Dyn., vol. 36, no. 8, pp. 1–19, 2018.

doi: 10.1080/07391102.2017.1338164.

[50] N. Hammoudi and al., "In silico drug discovery of IKK- β inhibitors from pyridine derivatives based on QSAR , docking , molecular dynamics and drug-likeness evaluation studies," J. Biomol. Struct. Dyn., vol. 0, no. 0, pp. 1–17, 2020.

doi: 10.1080/07391102.2020.1819878.

[51] J. M. Paggi, A. Pandit, and R. O. Dror, "The Art and Science of Molecular Docking," Annu. Rev. Biochem., vol. 93, pp. 389–410, 2024.

doi: /10.1146/annurev-biochem-030222- 120000.

[52] N. C. Oguanobi and al, "Modeling and kinetics investigation of adsorptive properties and regeneration of modified clay on azo dyes removal from aqueous solution using artificial intelligence (ANN , ANFIS) and RSM," Sigma J Eng Nat Sci, vol. 43, no. 1, pp. 316–339, 2025.

doi: 10.14744/sigma.2025.000.

[53] D. Bulanga and al, "Water hyacinth-derived adsorbent for removal of diclofenac sodium from aqueous solution : Modeling and optimization via RSM-ANN / ANFIS hybrid," Next Mater., vol. 9, no. July, p. 100997, 2025.

doi: 10.1016/j.nxmate.2025.100997.

[54] S. Automatisés and al, "An overview of the study of ANN-GA , ANN-PSO , ANFIS-GA , ANFIS-PSO and ANFIS- FCM predictions analysis on tool wear during machining process," Journal Européen des Systèmes Automatisés, vol. 56, no. 2, pp. 269–280, 2023.

doi: 10.18280/jesa.560212.

[55] S. Nemakanga and al, "Ultrasound-assisted synthesis of zeolite from bentonite clay : optimization using response surface methodology," Bull. Mater. Sci., vol. 0123456789, 2025.

doi: 10.1007/s12034-025-03447-w.

[56] A. Al-ali and U. Qidwai, "Rule-based modeling of low-dimensional data with pca and binary particle swarm optimization (BPSO) in ANFIS", Elsevier, arXiv : 2502 . 03895v1 [cs . CV] no. 6 Feb 2025," pp. 1–41, 2025.

[57] M. S. Narassima and al, "Reliability assessment of friction stir welds in AA100 aluminium alloy using ANN and ANFIS predictive models," nature portfolio; scientificreports, vol. 15:33297, pp. 1–25, 2025.

doi: 10.1038/s41598-025-04694-x 1.

[58] K. T. Edİlmesİ, "Lstm and anfis machine learning algorithms in estimating the sea water temperature in türkiye at various sea locations," Kahramanmaras Sutcu Imam University Journal of Engineering Sciences, KSU J Eng Sci, vol. 8, no. 1, pp. 322–333, 2025.

[59] S. Kumari and al., "An exploration of RSM , ANN , and ANFIS models for methylene blue dye adsorption using oryza sativa straw biomass : a comparative approach," nature portfolio; scientific reports, pp. 1–15, 2025.

doi: 10.1038/s41598-025-87274-3.

[60] A. Sadeghpour and G. Ozay, "Investigating the predictive capabilities of ANN , RSM , and ANFIS in assessing the collapse potential of RC structures," Arab. J. Sci. Eng., vol. 50, no. 16, pp. 13169–13190, 2025.

doi: 10.1007/s13369-024-09618-x.

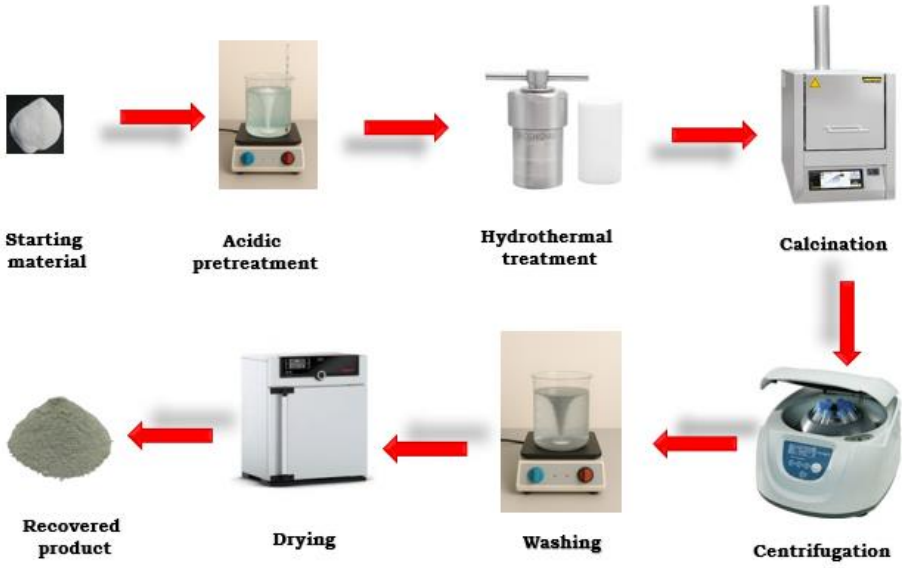
[61] A. Susaimanickam and al, "A comprehensive review on RSM - coupled optimization techniques and its applications," Arch. Comput. Methods Eng., vol. 30, no. 8, pp. 4831–4853, 2023.

doi: 10.1007/s11831-023-09963-4.

Chapter 2

Materials and methodologies for synthesis and analysis

In drug delivery research



1. Materials and methods

1.1 Chemicals

The starting material used in this study was Algerian expanded perlite and the bentonite (maghnite), which served as the source of silica and alumina for the synthesis of zeolite P and of sodalite, under hydrothermal and alkali fusion-hydrothermal conditions, respectively. Sodium hydroxide (NaOH), $CaCl_2$ $2H_2O$, $FeCl_3$ $6H_2O$, $Na_2CO_3^{2-}$ and hydrochloric acid (HCl) were purchased from Sigma Aldrich, while silver nitrate ($AgNO_3$) was obtained from BioChem. Ibuprofen with a purity of 99% was supplied by the Arab Pharm Laboratory (Ouled Saber, Setif, Algeria).

1.2 Preparation of zeolite P from expanded perlite

1.2.1 Pretreatment

Firstly, 10 g of expanded perlite was mixed with 100 ml of 0.1 M HCl solution and continuously stirred for 3 hours at 75°C. The solid obtained after filtration was washed several times with distilled water and tested with $AgNO_3$ to confirm the removal of chloride ions. The resulting solid powder was then dried overnight at 60°C and subsequently calcined at 800°C for 1 hour.

1.2.2 Hydrothermal synthesis of zeolite P

The recovered calcined powder was added to a 1 M NaOH solution with a solid to liquid ratio of 1:5 (g/ml). The mixture was stirred continuously for 24 hours to ensure complete homogenization and dissolution of reactive species. It was then transferred into a Teflon-lined stainless-steel autoclave and subjected to hydrothermal treatment at 100°C under atmospheric pressure for 4 days. The resulting solid product was filtered, washed repeatedly with distilled water until the filtrate reached neutral pH (≈7), and subsequently dried at 60°C for 24 hours to obtain the synthesized zeolite P powder.

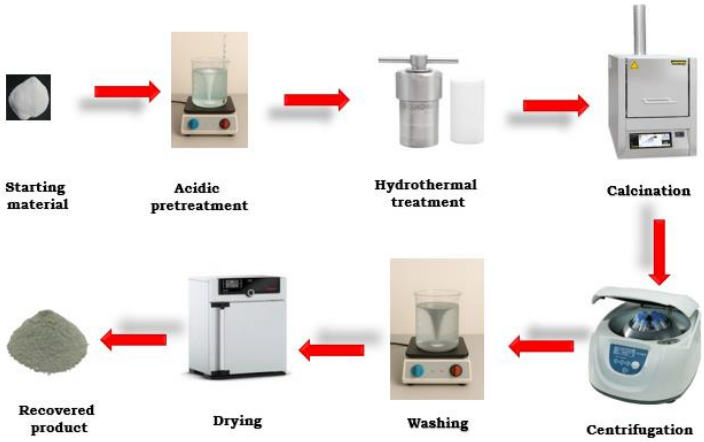


Figure 1: Hydrothermal synthesis of zeolite P from expanded perlite.

1.2.3 Photodeposition of zeolite P by 1% of silver

Our experimental protocol was based on the photodeposition method routinely used in our laboratory, as previously described [1- 3]. A weight of 15.75 mg of $AgNO_3$ was dissolved in 500 ml of distilled water in the dark for 15 minutes to prevent any premature photoreduction of silver ions. Then, 1 g of the synthesized zeolite P was added to the solution. The mixture was stirred for 2 hours under illumination from a 300 W xenon lamp to promote the photoreduction of Ag^+ to metallic Ag^0. The resulting solid was recovered by centrifugation and dried overnight at 60°C.

1.3 Preparation of sodalite from raw bentonite

Sodalite was prepared from Algerian bentonite via two important steps; the first step involved the fusion alkaline method, based on mixing the same quantity of bentonite and the NaOH and was calcined at 550°C for one hour. Then, the recovered calcined product was ground and sieved. After that, the powder was recalcined at 550°C for two hours and was also ground and sieved. In the second step of the hydrothermal treatment, the recovered powder was mixed with distilled water under continuous stirring for 72 hours to obtain gel. This gel was transferred into autoclave and reacted at 150°C for 48 hours. Finally, the obtained powder was filtered, washed several times by distilled water to obtain pH = 7 and was dried at 60°C for overnight.

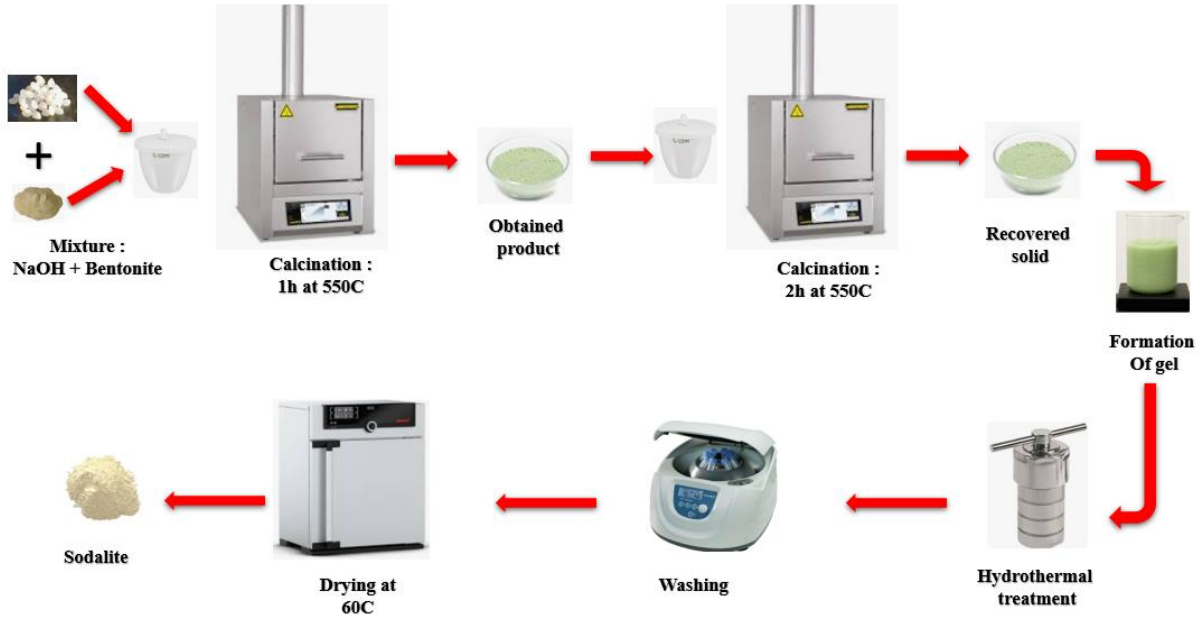


Figure 2: synthesis of sodalite from raw bentonite.

1.4 Synthesis of Layered Double Hydroxides LDH

The LDH was synthetized via co-precipitation method in alkaline medium at constant pH and also constant stirring [4, 5]. Succinctly, the synthesis of CaFe-CO_3^{2-}- LDH using the molar ratio $2 = \frac{M2+}{M3+}$ with M^{2+}: represented the divalent metal (Ca^{2+}) and M^{3+} for the trivalent metal such as the Fe^{3+}, via the co-precipitation method was based on the preparation of three solution; S_1, S_2 and S_3. Firstly, the preparation of aqueous solution (100 ml) contained the mixture of metal salts [S_1], then the dissolution of 8g of NaOH in 200 ml of distilled water for the concentration of 1M [S_2] and finally the solution of $Na_2CO_3^{2-}$ was prepared in 200 ml with 2M concentration [S_3]. The solution S_2 and S_3 were added drop by drop to the mixture S_1 under constant stirring and at pH adjusted to 10.5 for 4 hours. The mixture recovered after 4 hours was heated in an oil bath at 65°C under continuous stirring for 18 hours. Finally, the product slurry was filtered, washed several times with distilled water to remove the chloride which tested by $AgNO_3$ 1M and was dried overnight in oven vacuum at 65°C. A quantity of the LDH obtained was calcined at 450°C and at 550°C for 3 hours.

1.5 Drug loading

1.5.1 Loading of ibuprofen into zeolite P

Khodaverdi et al [6- 9], reported the loading of ibuprofen into zeolite using the solvent evaporation method. In the present study, 1 g of zeolite P was dehydrated at 60°C overnight to remove residual moisture from the pores. Subsequently, 100 mg of pure ibuprofen was dissolved in 20 ml of methanol, and 1 g of the dehydrated zeolite P was added to the resulting alcoholic solution under continuous stirring at 400 rpm and room temperature for 48 hours. The mixture was then filtered, and the obtained solid was dried in an oven at 30°C overnight, which was sufficient to evaporate the methanol solvent. The ibuprofen loaded zeolite P was finally stored in a desiccator until further use.

1.5.2 Loading of ibuprofen into sodalite

In the present work, a non-steroidal anti-inflammatory drug was selected as a representative pharmaceutical compound to investigate release behavior under varying pH conditions. Ibuprofen was chosen as the model drug and incorporated into the sodalite matrix using a solvent evaporation assisted loading strategy. Specifically, 100 mg of ibuprofen was first solubilized in 25 ml of methanol under continuous agitation to ensure complete dissolution. Subsequently, 1 g of sodalite was introduced into the drug solution, and the resulting suspension was maintained under stirring at 350 rpm for a duration of 48 h. This prolonged contact period facilitated the diffusion and adsorption of ibuprofen molecules into the porous structure of sodalite. Following solvent removal, the drug-loaded material was obtained, enabling subsequent evaluation of its release performance in media of different pH values.

1.5.3 Loading of ibuprofen into LDH

For loading of ibuprofen in LDH, two methods were used:

1.5.3.1 Physical mixture: in this method, a weight of 100 mg of ibuprofen was mixed with 1g of LDH in a mortar and pestle to obtain the physical mixture.

1.5.3.2 Dissolution of ibuprofen in alcoholic medium: Prior to drug loading, the layered double hydroxide (LDH) material was thermally treated at 60ºC overnight to eliminate physically adsorbed moisture within its pore structure. For the loading process, 100 mg of ibuprofen was

completely dissolved in 25 ml of ethanol to obtain a homogeneous solution. Subsequently, 1 g of the pretreated LDH was gradually introduced into the alcoholic medium and the suspension was maintained under continuous agitation at 450 rpm for 48 h at ambient temperature to facilitate effective drug incorporation. After completion of the loading step, the solid product was separated by filtration and dried in an oven at 30°C overnight. The resulting ibuprofen-loaded LDH was then preserved in a desiccator to prevent moisture uptake prior to further characterization and analysis.

1.6 Dissolution studies

1.6.1 Release of ibuprofen from zeolite P and LDH

This study was performed in accordance with the procedures described in the United States Pharmacopeia (USP) [8]. The dissolution of pure ibuprofen and the release profile of ibuprofen loaded into zeolite P and LDH samples (corresponding to an equivalent of 100 mg of ibuprofen) were investigated under simulated gastrointestinal conditions. The experiments were first conducted in simulated gastric fluid (SGF, pH 1.2, adjusted with HCl solution) for 2 hours, followed by simulated intestinal fluid (SIF, pH 6.8, adjusted with NaOH solution) for an additional 8 hours. All experiments were carried out in 900 ml of distilled water maintained at 37°C to simulate body temperature, under magnetic stirring at 100 rpm. At predetermined time intervals, 4 ml aliquots of the dissolution medium were withdrawn and immediately replaced with an equal volume of fresh simulated medium to maintain constant volume and concentration. The collected samples were then centrifuged at 4500 rpm for 5 minutes, and the amount of released ibuprofen was quantified using UV-visible spectrophotometry at a wavelength of 221 nm.

1.6.2 Release of ibuprofen from sodalite

The in vitro release behavior of ibuprofen incorporated into sodalite was investigated using a standardized dissolution procedure. The drug-loaded composite, prepared with an ibuprofen to sodalite mass ratio of 1:10 (mg/mg), was dispersed in 900 ml of simulated physiological media adjusted to different pH values. At predetermined time intervals, aliquots were withdrawn and subjected to centrifugation at 4500 rpm for 5 minutes to separate the solid phase from the release medium. The concentration of ibuprofen released into the supernatant was quantitatively determined using ultraviolet-visible (UV-Vis) spectroscopy by monitoring absorbance at a wavelength of 221 nm.

1.7 Physico-chemical characterizations

The elemental composition of both untreated and acid-modified expanded perlite samples was analyzed using wavelength dispersive X-ray fluorescence (XRF) spectroscopy. The quantitative results obtained from this analysis were reported in terms of oxide concentrations expressed as weight percentages.

The crystalline structure and phase identification of the synthesized zeolite P derived from the expanded perlite of the Bousaada deposit (Algeria), and the structural morphology of sodalite synthesized from raw bentonite sourced from Maghnia, Algeria, were analyzed by X-ray diffraction (XRD) using a Bruker D8 Discover diffractometer (Bruker Co., Germany). The instrument employed Cu Kα radiation (λ = 1.5406 Å) operated at 40 kV and 40 mA, with a step size of 0.02° over a 2θ range of 4 to 80°.

The SEM/EDS analysis was used to investigate the morphology, particle size, and chemical composition of the zeolite samples. Scanning Electron Microscopy (SEM) provides high resolution images that allow for detailed examination of the surface structure and morphology of the particles. Energy Dispersive X-ray Spectroscopy (EDS) complements this by providing elemental analysis, enabling the identification of the chemical composition of the samples. By metallizing the zeolite with gold, the surface characteristics can be enhanced for better imaging and analysis.

The Fourier transform infrared (FTIR) spectra were recorded using a PerkinElmer Spectrum 1000 spectrometer in the range of 400 to 4000 cm^{-1} to identify the functional groups and bonding characteristics of the zeolite framework.

Thermogravimetric analysis (TGA) and differential scanning calorimetry (DSC) were conducted using a METTLER TOLEDO TGA/DSC thermal analyzer. The samples, in small quantities, were placed in alumina crucibles and subjected to heating in a temperature range up to 1200 °C. The heating was carried out at a constant rate of 10 °C/min under a nitrogen atmosphere with a flow rate of 50 ml/min. This analysis aims to evaluate the thermal stability, weight changes, and thermal transitions of the samples, providing insights into their thermal properties and behavior under elevated temperatures.

The Micromeritics ASAP 2020 Plus, version 1.03, was utilized to study nitrogen adsorption and desorption isotherms at -196.204 °C, focusing on the pore volume, pore size, and surface area of the samples. Initially, the samples were measured and degassed under vacuum at approximately 400 °C for six hours. The total surface area was calculated using the BET method, while the pore volume was determined by the t-plot method based on a single point adsorption of nitrogen (N_2). This analysis aims to provide a detailed understanding of the textural properties of the samples.

Zeta potential and the size distribution of the samples were examined by the Malvern Zeta sizer nano Zs ZEN 3600 instrument with zeta sizer of 7.12 software. Where the samples were run in triplicates at 25ºC and at pH = 7.12.

Determining the pH point of zero charge is essential for understanding the specific charge characteristics of the sample. The experimental method involved preparing a 0.1 M NaCl solution to maintain a neutral working medium. From this stock solution, six Erlenmeyer flasks were prepared, each containing 50 ml of the solution with adjusted pH values of 2, 4, 6, 8, 10, and 12, using HCl and NaOH for adjustments. To each flask, 50 mg of zeolite was added, and the mixtures were stirred at 250 rpm for 24 hours to reach equilibrium. The final pH values were measured, and the pH_{pzc} was determined from the point where the initial and final pH values were equal. This procedure allows for accurate determination of the point of zero charge.

1.8 The antimicrobial activity of zeolite P:

The antimicrobial activities were prepared at the applied microbiology laboratory, department of microbiology, faculty of natural and life sciences, Ferhat ABBAS university of Setif 1.

1.8.1 The antibacterial activity:

1.8.1.1 Bacterial strains and chemical product:

The antibacterial activity of the samples was evaluated using four American Type Culture Collection (ATCC) reference strains. The Gram positive bacteria included *Staphylococcus aureus methicillin resistant* (MRSA, ATCC 43300) and *Bacillus subtilis* (ATCC 6633), while the Gram negative bacteria were *Escherichia coli* (ATCC 7839) and *Pseudomonas aeruginosa* (ATCC 27853). The antibacterial assays were conducted using a 96 well microplate (Greiner, VWR) and Mueller Hinton Agar (MHA) as the growth medium. The experiments required an incubator (Memmert BE 500), distilled water, a UV-visible spectrophotometer (JENWAY 6300, UK), and

the tested materials: zeolite P (S1) and silver doped zeolite P (S-Ag). The 2,3,5-triphenyltetrazolium chloride (TTC, 2 mg/ml) solution (Merck, Germany) was used as a viability indicator to assess bacterial metabolic activity.

1.8.2 Well diffusion method for the antibacterial activity of our zeolite P:

The antibacterial activity of the zeolite samples was evaluated using the agar well diffusion method**.** Nutrient agar was prepared according to the manufacturer's instructions and sterilized in an autoclave at 121 °C for 20 minutes. The sterilized agar was poured into sterile Petri dishes and allowed to solidify. Bacterial strains were cultured on sterile agar for 18 hours at 37 °C**.** Subsequently, bacterial suspensions with a turbidity equivalent to 0.5 McFarland standard (≈10^8 CFU/ml) were prepared from fresh (18 hour old) pure cultures. This turbidity corresponds to an optical density of 0.08 to 0.1 at 625 nm, measured using a UV-visible spectrophotometer. The turbidity was adjusted, when necessary, by adding more bacterial culture or by diluting the suspension with sterile medium.

A sterile cotton swab was used for uniform inoculation of the bacteria over the surface of the agar plates. Wells of 6 mm in diameter were made in the agar using a sterile Pasteur pipette. Each well was filled with 100 µl of zeolite suspension in nutrient broth at four different concentrations (100, 50, 25, and 10 mg/ml). The Petri dishes were then incubated at 37 °C for 24 hours, and the diameter of the inhibition zone around each well was measured to assess the antibacterial activity of the samples.

1.8.3 Determination of the minimum inhibitory concentration (MIC) of zeolite P:

The minimum inhibitory concentration (MIC) was determined to evaluate the antibacterial efficacy of the synthesized zeolite samples. This method identifies the lowest concentration of zeolite P at which no visible bacterial growth is observed after 24 hours of incubation. The 96 well microplate technique was employed using the microdilution method, with serial twofold dilutions prepared within the selected concentration range. The samples, zeolite P (S1) and silver doped zeolite P (S-Ag), were dispersed in distilled water using a vortex mixer and subsequently diluted twofold (v/v). Each well of the microplate was inoculated with 50 µl of bacterial suspension and 50 µl of the diluted sample solution, followed by incubation at 37°C for 24 hours. After incubation, the wells

were visually inspected for turbidity. To confirm bacterial growth, 40 µl of 2,3,5-triphenyltetrazolium chloride (TTC, 2 mg/ml) was added as a colorimetric indicator, and the plate was incubated again at 37°C for 2 hours. The MIC value was defined as the lowest concentration of the tested sample that inhibited visible bacterial growth, indicated by the absence of red coloration in the wells.

1.9 The minimum antifungal concentration of zeolite P:

1.9.1 Preparation of the Spore Suspension for Antifungal Evaluation:

The antifungal activity of the samples was evaluated to determine their effectiveness in inhibiting fungal growth. For this purpose, two toxigenic fungal strains were used: *Aspergillus niger* (ATCC 16888) and *Penicillium expansum* (ATCC 7861).

The spore suspension was prepared from fungal cultures grown on Czapek Dox agar slants and incubated at 22 ± 1°C for 5 days. A sterile Tween 80 solution (0.01%, v/v) was added to each slant to facilitate spore collection and to prepare the conidial suspension. The surface of the culture was then gently scraped with a sterile loop to release the spores into the suspension. The final spore inoculum concentration was adjusted to approximately 10^5 colony forming units per milliliter (CFU/ml), as determined using a Burker Türk counting chamber (hemocytometer).

1.9.2 Determination of the Minimal antifungal concentration (MFC):

The minimum fungicidal concentration (MFC) of zeolite P (S1) and silver doped zeolite P (S-Ag) was determined as the lowest concentration at which no visible fungal growth was observed after 72 hours of incubation. The assay was performed using a 96 well microplate following the microdilution method, with serial twofold dilutions prepared within the selected concentration range. The samples were dispersed in distilled water using a vortex mixer and subsequently diluted twofold (v/v). Each well was inoculated with 100 µl of fungal spore suspension and 100 µl of the diluted sample solution, then incubated at 37°C for 72 hours. The MFC value was defined as the lowest concentration of the sample that completely inhibited visible fungal growth.

2. Computational method:

2.1 DFT calculations:

Quantum chemical calculations were carried out using the Gaussian 09 software package employing the Density Functional Theory (DFT) method. The geometry of the ibuprofen molecule ($C_{13}H_{18}O_2$), considered in its neutral and isolated state, was first optimized using the B3LYP functional (Becke's three parameter hybrid functional combined with the Lee Yang Parr correlation functional) and the 6-311G (d, p) basis set.

The DFT method was employed to describe various molecular properties of ibuprofen, including its molecular electrostatic potential (MEP), vibrational frequencies, thermochemical parameters, molecular geometry, and the energies of the highest occupied molecular orbital (HOMO) and lowest unoccupied molecular orbital (LUMO). The optimized structure and electronic properties were used to compute several global reactivity descriptors: the energy band gap (ΔE) [Equation (a)], chemical hardness (η) [Equation (b)], chemical softness (δ) [Equation (c)], and chemical potential (μ) [Equation (d)] [10- 13].

$$\Delta E = E_{LUMO} - E_{HOMO} \quad \text{equation (a)}$$

$$\eta = \frac{1}{2}\Delta E \quad \text{equation (b)}$$

$$\delta = \frac{1}{\eta} \quad \text{equation (c)}$$

$$Cp = \frac{E(HOMO) - E(LUMO)}{2} \quad \text{equation (d)}$$

The energy gap (ΔE) is directly related to the chemical reactivity and selectivity of a molecule. The chemical hardness (η), defined as half the energy difference between the HOMO and LUMO, reflects the resistance of a molecule or atom to charge transfer. In contrast, the chemical softness (δ), also referred to as electronic polarizability, describes the ability of a molecule to accept

electrons [10]. A smaller energy gap corresponds to higher chemical reactivity and lower molecular stability, indicating that the molecule can more readily undergo electronic transitions. Conversely, a larger HOMO-LUMO energy gap is associated with greater stability, lower reactivity, and higher chemical hardness. Therefore, molecules exhibiting low hardness and high softness tend to be more reactive and more easily polarized [11].

2.2 Molecular docking

In this study, AutoDock Vina, AutoDock Tools, and Discovery Studio software were employed to perform molecular docking simulations in order to investigate the binding interactions between the pharmaceutical compound (ibuprofen, ligand) and the active site of the 5F1A protein (receptor). The three- dimensional structure of the 5F1A protein was obtained from the Protein Data Bank (PDB). The protein was prepared by removing water molecules and co-crystallized ligands, followed by energy minimization and addition of hydrogen atoms to correct the valence and protonation states. The ibuprofen molecule was constructed using ChemDraw 3D software and optimized prior to docking. The active site of the 5F1A receptor was identified using Discovery Studio, and a grid box defining the docking region was generated using AutoDock Tools. Molecular docking was then carried out with AutoDock Vina to estimate the binding affinities and interaction energies between ibuprofen and the target protein. The resulting docking complexes were further analyzed using Discovery Studio to identify the types of interactions involved, including hydrogen bonds, hydrophobic contacts, and van der Waals interactions [11, 14].

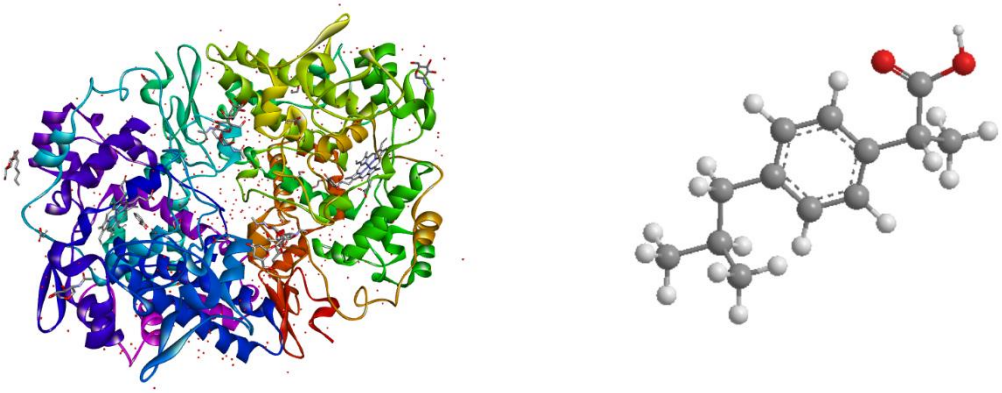


Figure 3: The crystal structure of 5f1a ibuprofen's receptor, and the ibuprofen structure on 3D.

3. Artificial Intelligence

3.1 Response surface methodology

The release behavior was systematically examined using response surface methodology (RSM) based on a central composite design (CCD). Three process parameters namely pH, contact time, and stirring speed were selected as independent variables. Each factor was investigated at three coded levels (-1, 0, and +1), as summarized in **Table 1**.

Table 1: Factors levels of independent variables for the release of ibuprofen.

Factor	Levels of variables		
	Low (-1)	medium (0)	High (+1)
pH	1	4.5	8
time (min)	20	70	120
Stirring rate (RPM)	50	75	100

The selection of the experimental domain was guided by preliminary batch experiments as well as findings reported in earlier studies [15]. In this investigation, the removal efficiency was considered as the response (dependent) variable. The total number of experimental runs required for the design, denoted as N, was calculated using **Equation (1)**, in accordance with established methodology [16, 17]:

$$\mathbf{N = 2^n + 2n + n_e} \quad \textbf{Equation (1)}$$

Where n is the number of input factors.

The phrases 2^n, 2n, and n_e represent the factorial (core) points, axial (star) points, and center points, respectively. To improve the robustness and reliability of the experimental design, both factorial and axial runs were performed in triplicate. Overall, eighteen experimental datasets were generated for the RSM analysis, including six center (null) points. The factorial points ensured a balanced distribution of low (-1), intermediate (0), and high (+1) factor levels, while the axial points were introduced to maintain uniform prediction variance at equal distances from the design center. The center points were incorporated to evaluate experimental reproducibility [18]. To minimize systematic bias, all experiments were carried out in a randomized sequence.

A second-order polynomial model was employed to describe the relationship between the response and the operating variables, as expressed in **Equation (2)**:

$$\mathbf{Y = \alpha_0 + \sum_{i=1}^{k} \alpha_i x_i + \sum_{i=1}^{k-1} \sum_{j=i+1}^{k} \alpha_i X_i X_j + \sum_{i=1}^{k} \alpha_{ii} x_{ii}^2} \quad \textbf{Equation (2)}$$

Y represents the estimated response; α0 is the model constant, while α_i, α_{ii}, and α_{ij} are the coefficients derived from the polynomial equation for the linear, pure quadratic, and interaction terms of x_i, x_i^2, and $x_i x_j$, respectively. Multivariate regression analysis utilizing the empirical model in **Equation (2)** was conducted to get the complete quadratic model in **Equation (3)**.

$$\mathbf{Y = \alpha_0 + \alpha_1 X_1 + \alpha_2 X_2 + \alpha_3 X_3 + \alpha_{11} X_1^2 + \alpha_{22} X_2^2 + \alpha_{33} X_3^2 + \alpha_{12} X_1 X_2 + \alpha_{13} X_1 X_2 + \alpha_{23} X_2 X_3 + \varepsilon} \quad \textbf{Equation (3)}$$

In the present study, Design-Expert software (version 13.0.5.0) was employed to construct the experimental design, perform regression analysis, conduct analysis of variance (ANOVA), and optimize the process variables governing ibuprofen release from sodalite. The adequacy and reliability of the proposed model were evaluated using the coefficient of determination (R^2) and ANOVA derived p-values (with significance assessed at levels below 5%).

3.2 Artificial neural network

The experimental dataset generated through response surface methodology (RSM) was considered adequate for initial evaluation of the artificial neural network (ANN) model [18]. However, it is well established that ANN performance improves with increased data volume. To enhance model

learning and predictive accuracy, the original RSM dataset was replicated, yielding a total of 125 data points for ANN implementation. Neural network simulations were carried out using MATLAB software (version R2014a, 8.3.0.532). A multilayer perceptron (MLP) architecture was selected for network training, employing a backpropagation algorithm to iteratively adjust network weights. The ANN structure consisted of an input layer, a single hidden layer comprising multiple neurons, and an output layer. The input variables included solution pH, contact time (min), and stirring speed (RPM), while the output neuron corresponded to the measured absorbance, as depicted in **Figure 4**.

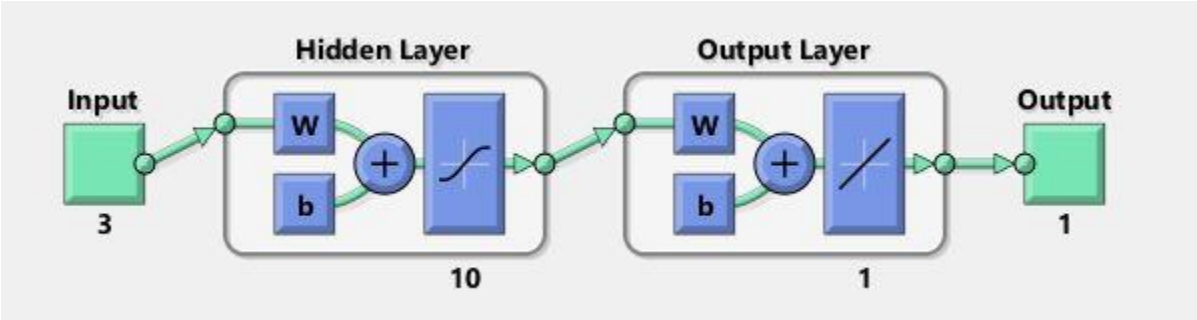


Figure 4: ANN architecture structure of ibuprofen release.

The selection of an appropriate number of neurons in the hidden layer was achieved through repeated evaluation of multiple network configurations, with the objective of obtaining the minimum mean square error (MSE) alongside the highest coefficient of determination (R^2). This optimization strategy was intended to reduce discrepancies between predicted and experimental values while preventing model overfitting. Both excessively large and insufficient hidden-layer sizes were deliberately avoided, as they may lead to over-parameterization or slow convergence behavior, respectively [19]. The available dataset was partitioned into three subsets, with approximately 70% assigned for training, 15% reserved for testing, and the remaining 15% used for validation. Allocating a greater proportion of data to the training phase contributed to improved learning efficiency and reduced computational time. The testing subset provided an unbiased evaluation of model performance, whereas the validation subset monitored the network's ability to generalize, terminating training when further improvements were no longer observed [20]. The

Trainlm algorithm was selected as the learning function to regulate bias adjustment during training. To further enhance convergence and minimize prediction error, all input variables and output responses were scaled to a normalized range between 0 and 1 prior to network training [21, 22].

3.3 Adaptive neuro fuzzy inference system

Adaptive Neuro-Fuzzy Inference Systems (ANFIS) constitute a powerful hybrid modeling approach that combines the learning capability of artificial neural networks with the reasoning framework of fuzzy logic, making it particularly effective for rapid simulation of complex nonlinear processes [23]. In the present work, the same set of 125 data points used for ANN training was consistently employed for the development of the ANFIS model.

The ANFIS architecture was configured as a five-layer computational structure based on fuzzy inference principles. As depicted in **Figure 5**, the first and final layers correspond to the system inputs pH, contact time (min), and stirring speed (RPM) and the system output, namely the release response. The constructed model follows a first-order Sugeno-type inference scheme. In the second layer, input variables are transformed into fuzzy values using predefined membership functions through the fuzzification process. The third layer applies a set of fuzzy logic rules to generate intermediate inference results. These inferred values are subsequently converted into crisp numerical outputs during the defuzzification step in the fourth layer using output membership functions [24]. Finally, the fifth layer consists of a single computational node that aggregates all incoming signals to produce the overall predicted release value.

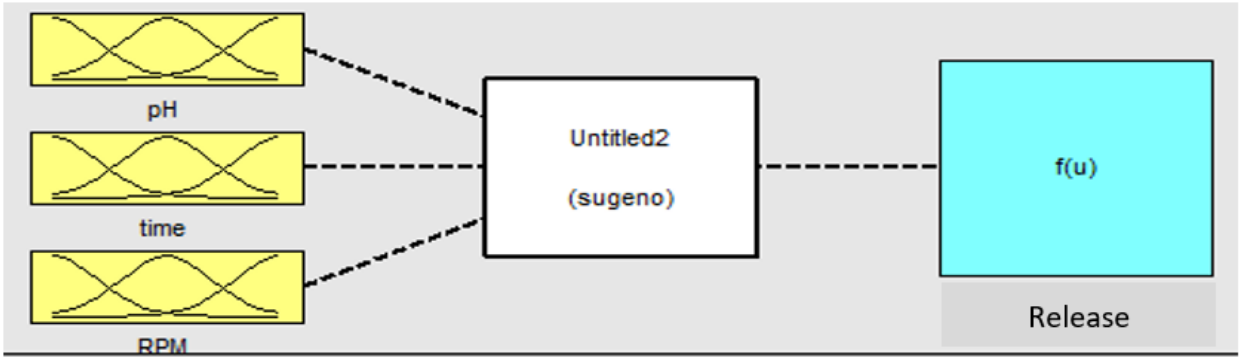


Figure 5: ANFIS structure of the ibuprofen release.

3.4 Model performance indices

The predictive effectiveness of the RSM, ANN, and ANFIS models was systematically examined using a set of quantitative performance indicators to determine the most accurate modeling approach for representing the experimental observations. A total of seven advanced statistical error metrics were applied in this evaluation, as summarized in **Table 2**. These assessment criteria were selected based on the inherent characteristics and distribution of the experimental dataset [24]. In addition to numerical analysis, a comparative parity plot was generated to visually assess deviations between model predicted values and corresponding experimental measurements, thereby highlighting localized discrepancies among the RSM, ANN, and ANFIS predictions.

Table 2: Statistical error functions.

Error function	Equation	Eq. Num.	Ref.
Hybrid fractional error function	$HYBRID\ (\%) = \frac{1}{N-P}\sum[\frac{(P_{R,i,exp} - P_{R,i,cal})^2}{P_{R,i,exp}}]*100$	4	[25]
Average relative error	$ARE\ (\%)\ = \frac{100}{N}\sum_{i-1}^{N}[\frac{(P_{R,i,exp} - P_{R,i,cal})}{P_{R,i,exp}}]$	5	[25]
Correlation coefficient	$R^2 = \frac{\sum_{i-1}^{N}(P_{R,i,cal} - P_{R,i,ave})^2}{\sum_{i=1}^{N}(P_{R,i,cal} - P_{R,i,ave})^2 + \sum_{i=1}^{N}(P_{R,i,cal} - P_{R,i,exp})^2}$	6	[25]
Marquardt's percent standard error deviation	$MPSED\ (\%) = \sqrt{\frac{\sum(\frac{(P_{R,exp} - P_{R,cal})}{P_{R,exp}})^2}{N-P}} * 100$	7	[25]
Absolute average relative error	$AARE = \frac{1}{N}\sum_{i=1}^{N}(\left\|\frac{(P_{R,\exp\,(i)} - P_{R,cal(i)})}{P_{R,\exp\,(i)}}\right\|)$	8	[25]
Adjusted R^2	$Adj\ R^2 = 1 - [(1-R^2) * \frac{N-1}{N-P-2}]$	9	[25]
Root mean square error	$AARE = \sqrt{\sum_{i=1}^{N}\frac{1}{N}(\frac{(P_{R,\exp\,(i)} - P_{R,cal(i)})}{P_{R,\exp\,(i)}})^2}$	10	[25]

In this context, the symbol N represents the total count of experimental trials carried out in the study. The notation $PR_{exp(i)}$, $PR_{e, i, exp}$ and $PR_{i, exp}$, refer to the measured response values obtained experimentally for each individual run. Correspondingly, $PR_{cal(i)}$, $PR_{e, i, cal}$ and $PR_{i, cal}$, denote the response values estimated by the predictive models for the same set of experiments. The term $PR_{exp,ave}$ indicates the average response calculated from all experimental measurements. Additionally, P corresponds to the number of independent input parameters included in the experimental design.

References:

[1] M. K. Guediri and al., "Interfacial coupling effects on adsorptive and photocatalytic performances for photoresponsive graphene wrapped-SrTiO 3 @ Ag under UV-visible light : experimental and DFT approach To cite this version : hal Id : hal-03589904," 2022. doi.org/10.1007/s11356-021-17543-x.

[2] A. Guediri and al, "Molecular dynamic simulation and DFT computational studies on the adsorption performances of methylene blue in aqueous solutions by orange peel-modi fi ed phosphoric acid," J. Mol. Struct., vol. 1202, p. 127290, 2020. doi: 10.1016/j.molstruc.2019.127290.

[3] M. K. Guediri and al, "Novel Fe2TiO5/reduced graphene oxide heterojunction photocatalyst with improved adsorption capacity and visible light photoactivity: experimental and DFT approach," Environmental Science and Pollution Research, 28 (7). 10.1007/s11356-020-11221-0. hal-02996413, pp.8507-8519, 2021.

[4] M. A. Woo, and al, " Phosphate-intercalated Ca – Fe-layered double hydroxides : Crystal structure , bonding character , and release kinetics of phosphate," J. Solid State Chem., vol. 184, no. 1, pp. 171–176, 2011. doi: 10.1016/j.jssc.2010.11.003.

[5] K. Imene and al., "Thermal treatment of Cu-doped hydrotalcite-like adsorbents for improved removal of methyl orange from water," Sep. Purif. Technol., vol. 365, no. March, p. 132656, 2025. doi: 10.1016/j.seppur.2025.132656.

[6] E. Khodaverdi and al, "Synthetic zeolites as controlled-release delivery systems for anti-inflammatory drugs," Chem. Biol. Drug Des., vol. 87, no. 6, pp. 849–857, 2016. doi: 10.1111/cbdd.12716.

[7] E. Khodaverdi and al, "Evaluation of synthetic zeolites as oral delivery vehicle for anti-inflammatory drugs," Iran J Basic Med Sci, vol. 17, no. 3, pp 337-343, 2014.

[8] M. G. Rimoli et al., "Synthetic zeolites as a new tool for drug delivery," 2007. doi: 10.1002/jbm.a.31763.

[9] N. Paradee and A. Sirivat, "Encapsulation of folic acid in zeolite y for controlled release via electric field," 2015.

doi: 10.1021/acs.molpharmaceut.5b00592.

[10] M. E. Ayalew, "DFT studies on molecular structure , thermodynamics parameters , HOMO-LUMO and spectral analysis of pharmaceuticals compound quinoline (benzo [b] pyridine)," pp. 29–42, 2022.
doi: 10.4236/jbpc.2022.133003.

[11] O. E. Oyeneyin and al, "Structural modification of ibuprofen as new nsaids via DFT , molecular docking and pharmacokinetics studies," vol. 33, no. 4, pp. 614–626, 2021.
doi: 10.7240/jeps.928422.

[12] Y. Wei and P. Liu, "Analysis of the nature of interaction between AlN nanocage and ibuprofen using quantum chemical study," Structural Chemistry, vol.32, pp. 1685–1692, 2021.
https://doi.org/10.1007/s11224-021-01750-w

[13] N. E. Binbay, "Analysis of ibuprofen and naproxen based two nsaid candidates with theoretical dft calculations," journal of health, medicine and nursing, vol. 78, pp. 18–26, 2020.
doi: 10.7176/JHMN/78-03.

[14] R. Wang and al, "Comparison of three molecular simulation approaches for cyclodextrin-ibuprofen complexation," journal of nanomaterials. Hindawi, vol. 2015, 2015.
doi: 10.1155/2015/193049.

[15] C. E. Onu and al, "Evaluation of optimization techniques in predicting optimum moisture content reduction in drying potato slices," Artif. Intell. Agric., vol. 4, pp. 39–47, 2020.
doi: 10.1016/j.aiia.2020.04.001.

[16] A. S. Thajeel, "Modeling and optimization of adsorption of heavy metal ions onto local activated carbon," Aquat. Sci. Technol., vol. 1, no. 2, 2013,
doi: 10.5296/ast.v1i2.3890.

[17] M. Arulkumar and al, "Optimization of orange g dye adsorption by activated carbon of thespesia populnea pods using response surface methodology," J. Hazard. Mater., vol. 186, no. 1, pp. 827–834, 2011.
doi: 10.1016/j.jhazmat.2010.11.067.

[18] J. N. Sahu and al, "Optimization of production conditions for activated carbons from Tamarind wood by zinc chloride using response surface methodology," Bioresour.

Technol., vol. 101, no. 6, pp. 1974–1982, 2010.
doi: 10.1016/j.biortech.2009.10.031.

[19] M. Fan and al., "Artificial neural network modeling and genetic algorithm optimization for cadmium removal from aqueous solutions by reduced graphene oxide-supported nanoscale zero-valent iron (nZVI/rGO) composites," Materials (Basel)., vol. 10, no. 5, p. 544, 2017. doi: 10.3390/ma10050544.

[20] O. Chijioke Elijah and al, "Application of modified agricultural waste in the adsorption of bromocresol green dye," Asian J. Chem. Sci., pp. 15–24, 2020.
doi: 10.9734/ajocs/2020/v7i119011.

[21] P. E. Ohale and al, "Optimal factor evaluation for the dissolution of alumina from Azaraegbelu clay in acid solution using RSM and ANN comparative analysis," South African J. Chem. Eng., vol. 24, pp. 43–54, 2017.
doi: 10.1016/j.sajce.2017.06.003.

[22] M. Mourabet and al, "Comparative study of artificial neural network and response surface methodology for modelling and optimization the adsorption capacity of fluoride onto apatitic tricalcium phosphate," Univers. J. Appl. Math., vol. 2, no. 2, pp. 84–91, 2014.
doi: 10.13189/ujam.2014.020202.

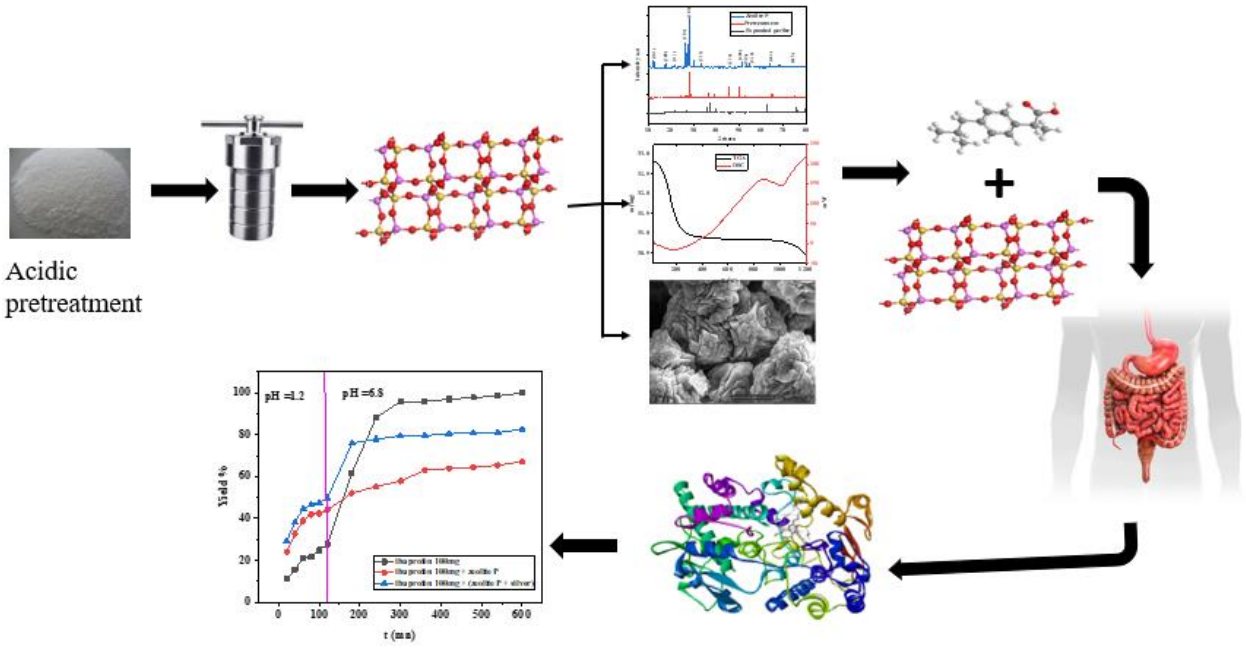
[23] R. T. Gonzalez del Cerro and al, "Modelling the daily reference evapotranspiration in semi-arid region of South India: A case study comparing ANFIS and empirical models," Inf. Process. Agric., vol. 8, no. 1, pp. 173–184, 2021.
doi: 10.1016/j.inpa.2020.02.003.

[24] M. S. Zaghloul and al, "Comparison of adaptive neuro-fuzzy inference systems (ANFIS) and support vector regression (SVR) for data-driven modelling of aerobic granular sludge reactors," J. Environ. Chem. Eng., vol. 8, no. 3, p. 103742, 2020.
doi: 10.1016/j.jece.2020.103742.

[25] H. A. M. Atta, "Artificial Neural Network [ANN] modeling for tetracycline adsorption on rice husk using continuous system," Desalin. Water Treat., vol. 317, no. December 2023, p. 100026, 2024.
doi: 10.1016/j.dwt.2024.100026.

Chapter 3

New synthesis of zeolite P from expanded perlite for gastrointestinal drug release using ibuprofen as a NSAID model. DFT calculation, molecular docking and antimicrobial activity



The objective of this study is to synthesize zeolite P via the hydrothermal method using natural raw materials as the aluminosilicate source. Expanded perlite from the Bousaada deposit (Algeria) was selected as the starting material owing to its suitable composition and local abundance. The synthesized zeolite P was investigated for its potential pharmaceutical application as a carrier for the controlled release of ibuprofen in simulated gastrointestinal fluid. In parallel, computational studies were conducted on the ibuprofen molecule to complement the experimental results. Density Functional Theory (DFT) calculations were used to optimize its molecular geometry, evaluate the energy gap, and analyze its electronic and vibrational properties. Additionally, molecular docking simulations were carried out to investigate the interaction of ibuprofen with its biological targets, providing insight into its binding affinity and interaction mechanisms. Furthermore, the antibacterial activity of the synthesized zeolite P and Ag-doped zeolite P (1 wt% Ag) was evaluated against selected bacterial strains. The incorporation of silver into the zeolite framework aimed to enhance its antimicrobial properties while maintaining its structural integrity. Comparative analysis between the undoped and Ag-doped samples demonstrated the influence of silver on the antibacterial efficiency of zeolite P, confirming its potential use in biomedical and pharmaceutical applications.

Results and discussion

1. Physico-chemical characterizations

1.1 The X-ray fluorescence (XRF) analysis

The oxide composition of the starting material was quantified by X-ray fluorescence (XRF) analysis, and the results are summarized in **Table 1** as weight percentages.

Table 1: The chemical compositions of expanded perlite.

Component	SiO_2	Al_2O_3	Na_2O	K_2O	CaO	Fe_2O_3	MgO
%	74.9	13.6	4.05	4	1.53	1.21	0.226

TiO_2	P_2O_5	MnO	Cl	SO_3	SrO	ZrO_2	Rb_2O	Ag_2O
0.147	0.119	0.0677	0.0478	0.0444	0.0176	0.0124	0.0124	0.0072

1.2 X-ray diffraction (XRD) analysis

Figure 1a presents the X-ray diffraction (XRD) pattern of zeolite P synthesized from expanded perlite, used as a natural aluminosilicate source, after pretreatment with 0.1 M HCl at 75 °C for 3h. The obtained diffraction pattern shows good agreement with previously reported data, and the crystalline phases were identified by comparing the experimental results with standard reference files using the HighScore Plus program.

The zeolite P sample displays characteristic diffraction peaks at 2θ values of 12.4509°, 17.7475°, 21.6934°, 28.0247°, 33.3936°, 44.1551°, 45.7457°, 51.4584°, 53.2866°, 54.9129°, 64.0709°, and 74.4163°, which are indexed to the (101), (200), (112), (103), (312), (224), (105), (404), (503), (424), (444), and (615) planes, respectively. These reflections confirm the formation of the typical tetragonal crystal structure of zeolite P **(PDF No. 01-080-0699)**, with the composition $Na_{3.552}(Al_{3.6}Si_{12.4}O_{32})\cdot(H_2O)_{10.656}$.

In addition, a peak at 2θ = 26.6°, corresponding to the (101) plane, indicates the presence of quartz as a minor secondary phase within the zeolitic material **(PDF No. 01-083-2465)**.

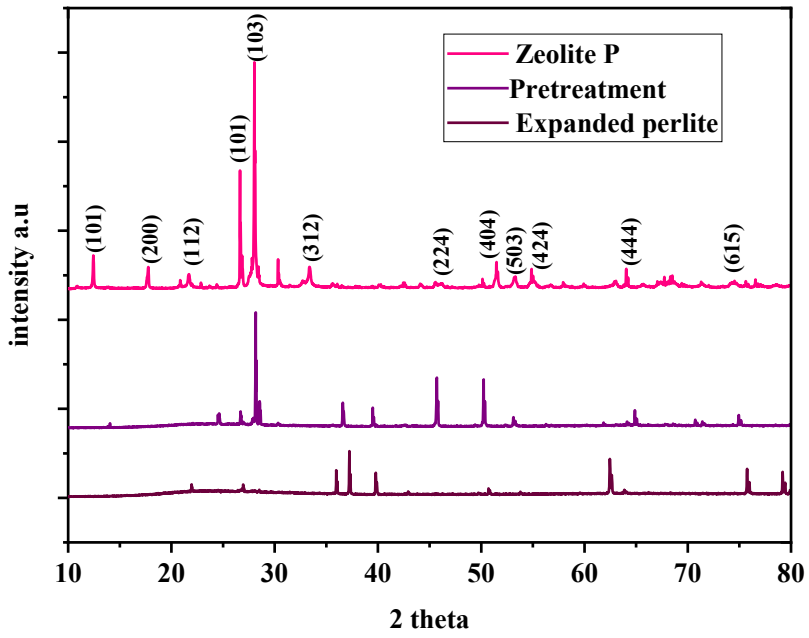


Figure 1 a: XRD of the zeolite P synthesized from expanded perlite after it pretreatment with 0.1M HCl at 75°C for 3hours.

The crystallite size of the synthesized zeolite P was evaluated from the XRD data using HighScore Plus software. The mean crystallite size was obtained by analyzing the broadening of the diffraction peaks and applying the Scherrer equation: $D = \frac{K\lambda}{\beta(cos\theta)}$, where;

D is the crystallite size,

K is the shape factor (taken as 0.9),

λ is the X-ray wavelength (Cu Kα = 1.5406 Å),

β is the full width at half maximum (FWHM, in radians), and θ is the Bragg angle [1].

Peak broadening parameters were extracted in HighScore Plus, and the crystallite size was determined by averaging values from multiple well-defined reflections including (101), (200), (112), (103), (312), (224), (404), (503), (424), (444), and (615) (**Figure 3 a**) rather than relying on a single peak, ensuring a more representative estimation.

The resulting average crystallite size of 77.72 nm indicates the formation of a highly crystalline zeolite P structure derived from expanded perlite through hydrothermal synthesis. This nanoscale crystallite size aligns with the high degree of crystallinity observed in both SEM images and the sharp, intense XRD peaks.

Rietveld refinement of the powder XRD pattern (**Figure 1b**) further supports these findings. Quantitative phase analysis revealed that the product consists of 96.3 wt% zeolite P and 3.7 wt% quartz. This confirms that zeolite P is the predominant phase, with only a minor quartz impurity, which is expected given the natural mineral composition of expanded perlite.

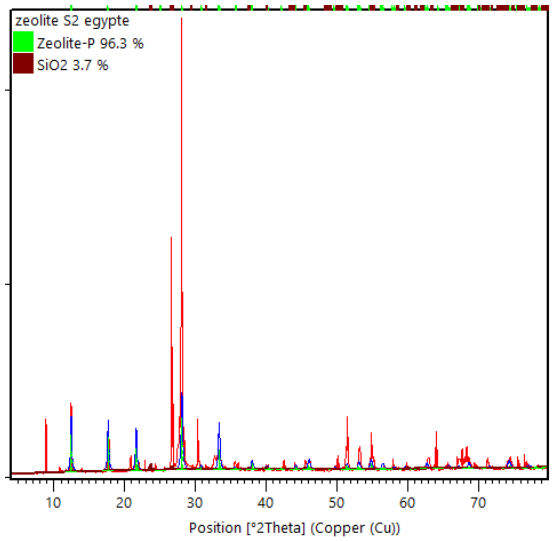


Figure 1 b: The percent of various phase in XRD by Rietveld method.

1.3 Scanning electron microscopy (SEM) and EDS analysis of zeolite P

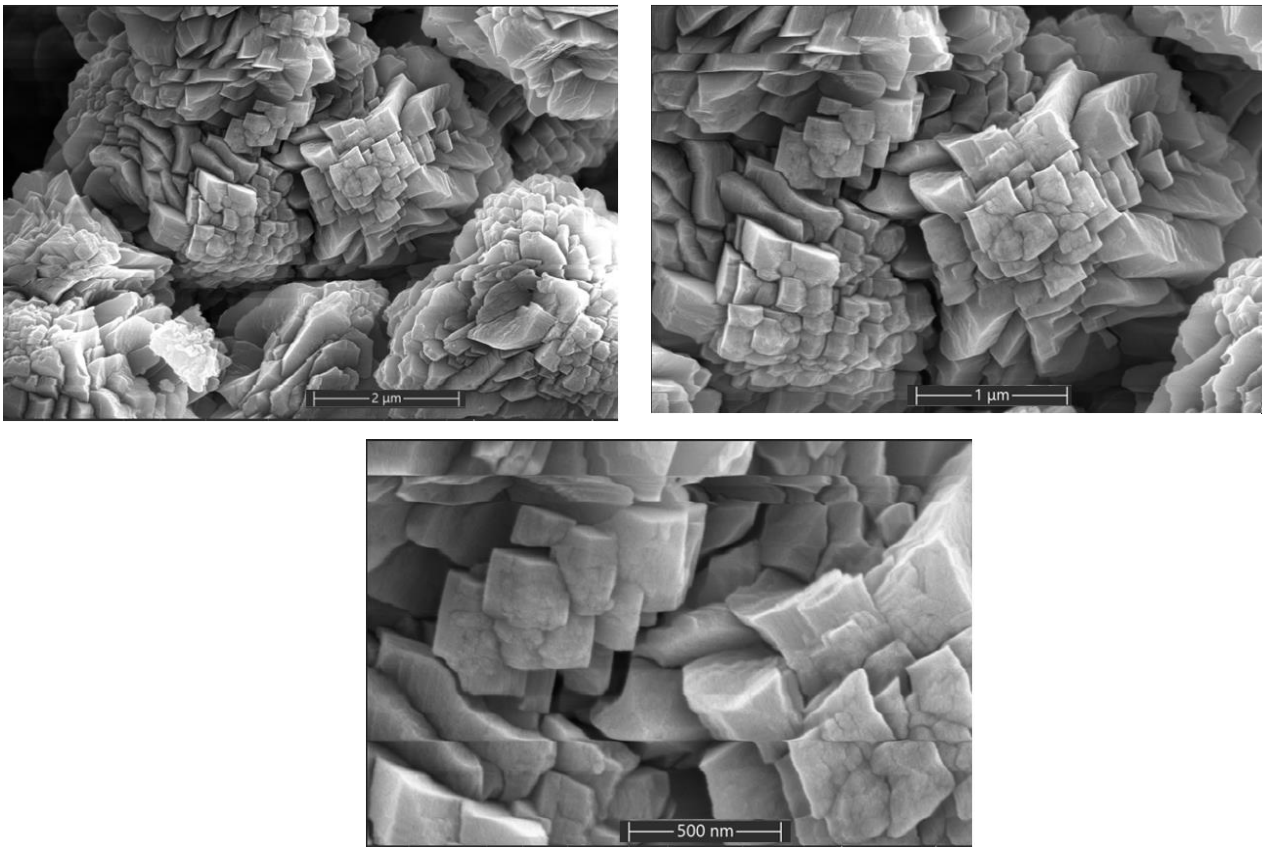
As illustrated in **Figure 2a**, and following the XRD confirmation of the zeolite P phase, scanning electron microscopy (SEM) was used to investigate the morphology of the synthesized material. The SEM micrographs show that the zeolite P crystals possess a tetragonal, diamond like morphology with well-defined facets and sharp crystal edges, characteristic of the Na-P1 zeolite

(GIS type) framework. This diamond shaped appearance reflects the prismatic or rhombohedral habit typically associated with crystals formed under hydrothermal conditions. Alongside these primary diamond-like structures, some particles exhibit a cactus like form composed of intergrown or radially oriented crystals, suggesting secondary nucleation events and continued crystal growth on existing surfaces [2]. These morphological observations collectively indicate the formation of a highly crystalline zeolite P produced through hydrothermal synthesis using expanded perlite as the aluminosilicate precursor.

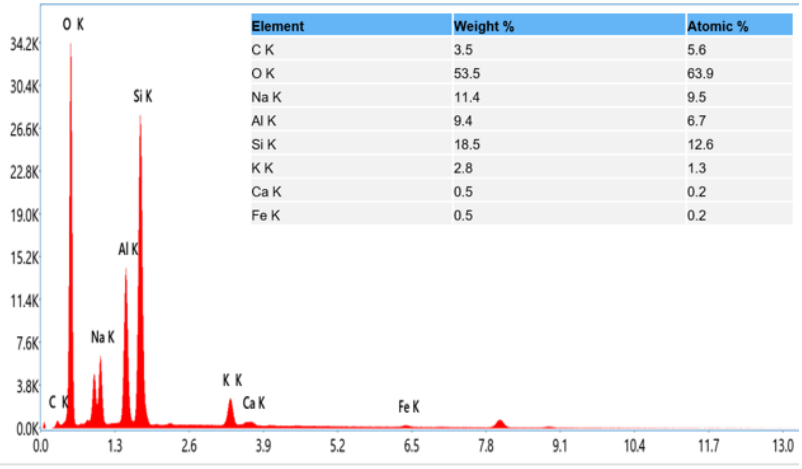
The accompanying energy dispersive X-ray (EDX) spectrum, shown in **Figure 2b**, provides the elemental composition of the sample in both weight percent and atomic percent. From this analysis, a SiO_2/Al_2O_3 ratio of 2.23 was obtained, which aligns well with previously reported values and further validates the successful formation of zeolite P from a natural aluminosilicate source.

Additionally, the EDX results indicate a Si/Al atomic ratio of about 1.97, a value consistent with the known compositional range of Na-P1 zeolite (Si/Al < 2.2). This compositional agreement, together with the tetragonal structure identified by XRD, reinforces the conclusion that zeolite P was effectively synthesized from expanded perlite [3].

a



b



Element	Weight %	Atomic %
C K	3.5	5.6
O K	53.5	63.9
Na K	11.4	9.5
Al K	9.4	6.7
Si K	18.5	12.6
K K	2.8	1.3
Ca K	0.5	0.2
Fe K	0.5	0.2

Figure 2: SEM images (a) and the EDS analysis (b) of zeolite P.

1.4 Fourier Transform Infra-Red (FTIR)

The Fourier Transform Infrared (FTIR) spectra of the various samples are shown in **Figure 3**. The spectrum of the untreated raw material, collected from the Bousaada deposit in Algeria, represents the natural aluminosilicate precursor used for the synthesis of zeolite P following acid pretreatment with 0.1 M HCl at 75 °C for 3 h. The FTIR spectra of pure zeolite P, silver photodeposited zeolite P (1 wt% Ag), pure ibuprofen, and ibuprofen-loaded zeolite P are also included in **Figure 3** for comparison.

In these spectra, the band at 1638 cm^{-1} is associated with the bending vibration of physically adsorbed water molecules. The broad bands detected within the 1000 to 1035 cm^{-1} region correspond to the asymmetric stretching modes of Si-O-Si and Al-O-Al groups that form the primary framework of the zeolite structure. Absorption bands appearing between 694 and 790 cm^{-1} are attributed to Si-O-Al stretching vibrations, whereas those in the 411 to 445 cm^{-1} region are assigned to Si-O bending modes, which further reflect the structural characteristics of the zeolite framework [4-6].

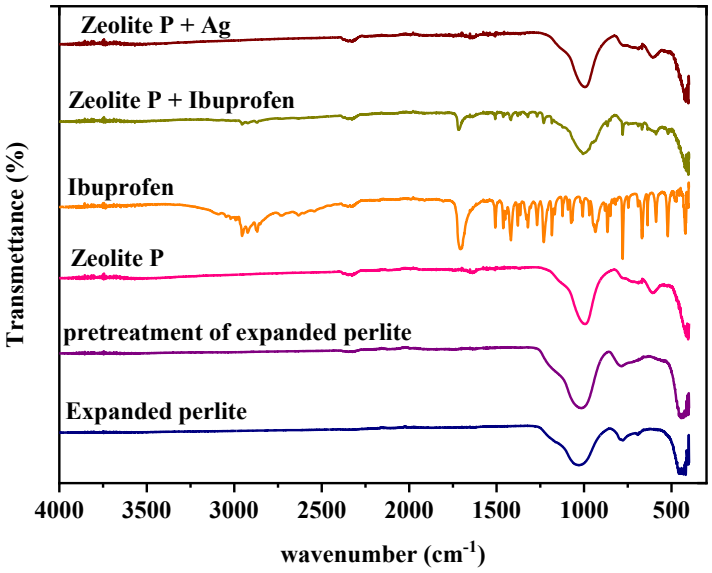


Figure 3: FTIR spectra of the zeolite P synthesized from expanded perlite after its pretreatment by 0.1M HCl at 75^0C for 3 hours, loaded by ibuprofen and its photodeposition by Ag.

1.5 Point of pH zero charge pH_{PZC}

Based on the curve presented in **Figure 4**, the point of zero charge (pH_{pzc}) was identified at the point where the diagonal line intersects the pHf versus pHi plot. The pH_{pzc} point was determined to be 7.93, which divides the curve into two distinct behavioral regions.

At solution pH values below the pH_{pzc}, the surface functional groups of the material undergo protonation due to the higher concentration of H^+ ions. As a result, the surface acquires a net positive charge, which enhances its affinity toward anionic species.

In contrast, when the solution pH exceeds the pH_{pzc}, deprotonation of the surface groups occurs because of the abundance of OH^- ions, giving the surface a negative charge and promoting the adsorption of cationic species[7]. The pH_{pzc} value of 7.93 obtained in this study implies that zeolite P can interact favorably with both anionic and cationic molecules, since this value is close to neutral pH, indicating a nearly balanced surface charge under typical physiological conditions.

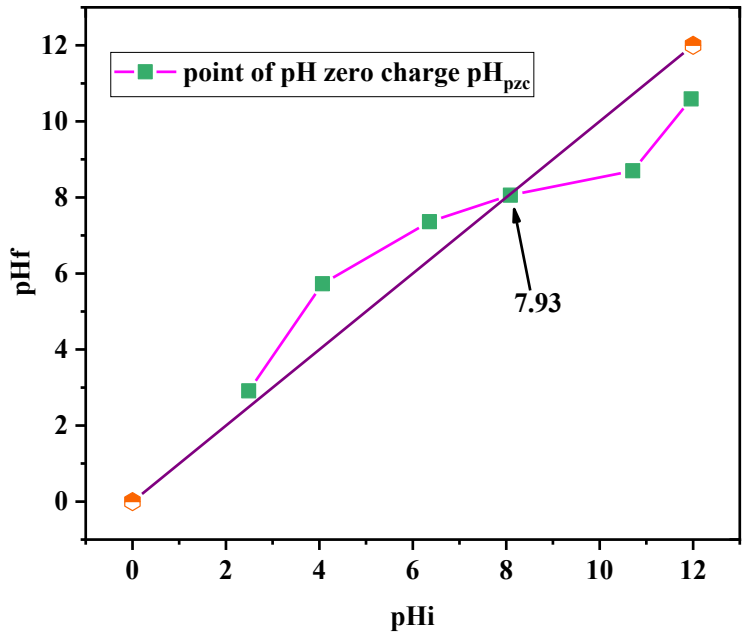


Figure 4: Point of zero charge pH_{PZC} of synthetic zeolite P (pH = from 2 to 12, Speed = 250rpm, v = 50ml, m = 50mg).

1.6 Thermogravimetric analysis TGA and differential scanning calorimetry DSC

Thermogravimetric analysis (TGA) was carried out to assess the thermal stability and decomposition behavior of zeolite P across a temperature range of 33°C to 1200°C (**Figure 5a**). In parallel, differential scanning calorimetry (DSC) was performed to identify thermal transitions, with particular attention to the endothermic events related to the release of water molecules and the processes associated with template removal during calcination [8, 9] .

As shown in the TGA curve in **Figure 5a**, the first major weight loss of 5.799% occurs between 33°C and 400°C. This mass reduction is attributed to the removal of physically adsorbed water located on the external surface and within the internal channels of the zeolite. During the second stage, from 400°C to 900°C, the weight loss becomes minimal compared with the initial and final stages, indicating that the majority of water molecules had already been eliminated in the early phase of heating. This confirms that zeolite P undergoes complete dehydration by approximately 400°C [9].

In the third stage, spanning 900°C to 1200°C, the material exhibited an additional weight loss of approximately 1.3%. This loss may be attributed to the release of remaining volatile species, partial decomposition of the framework, or structural transformations occurring within the zeolite lattice.

The DSC results corroborate the TGA observations. An endothermic peak near 200°C corresponds to the removal of adsorbed water molecules, aligning with the initial mass-loss region observed in the TGA curve. The absence of notable thermal events between 400°C and 900°C further indicates that zeolite P maintains strong thermal stability throughout this temperature interval. An exothermic signal detected between 900°C and 1200°C suggests the formation of new crystalline phases or the onset of structural degradation of the zeolite framework.

Collectively, the combined TGA/DSC analyses demonstrate that zeolite P synthesized from expanded perlite possesses high thermal stability.

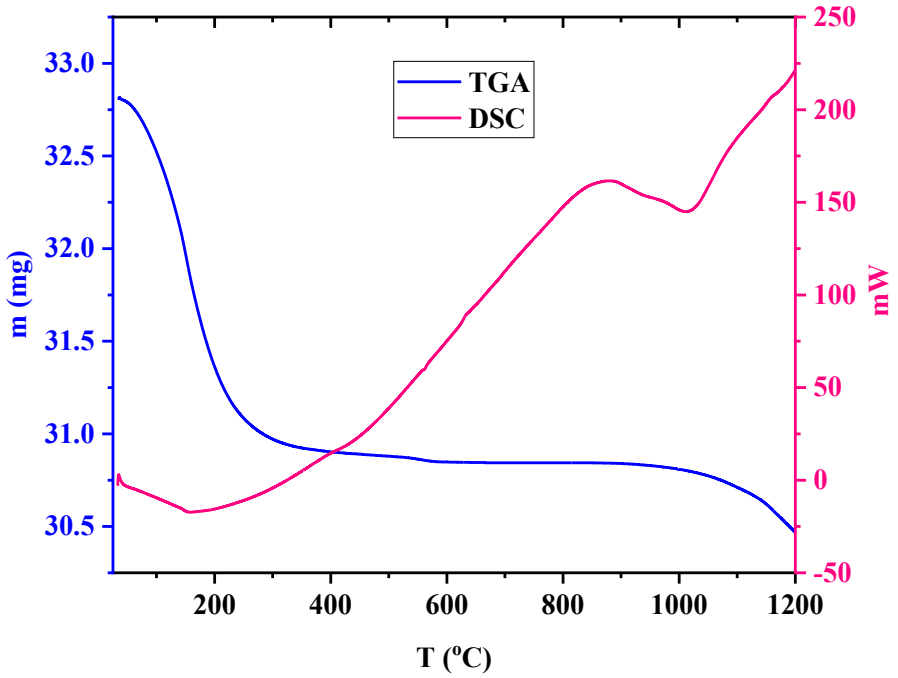
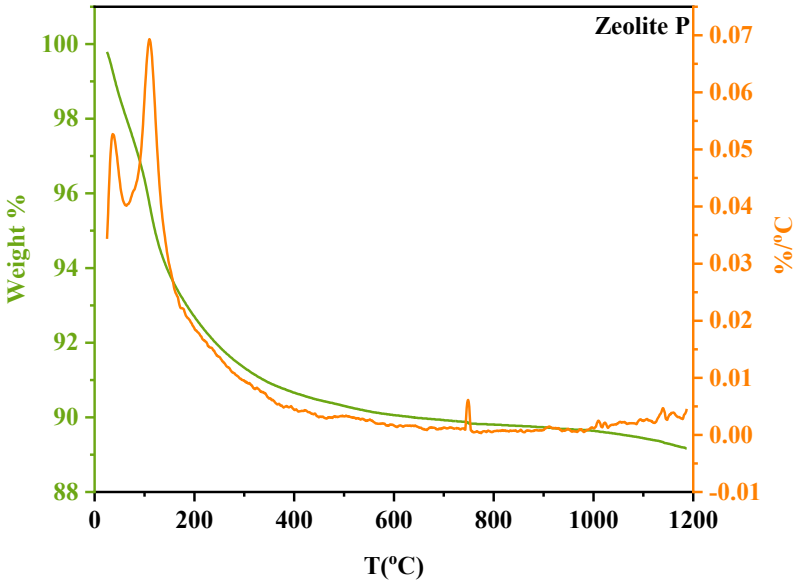
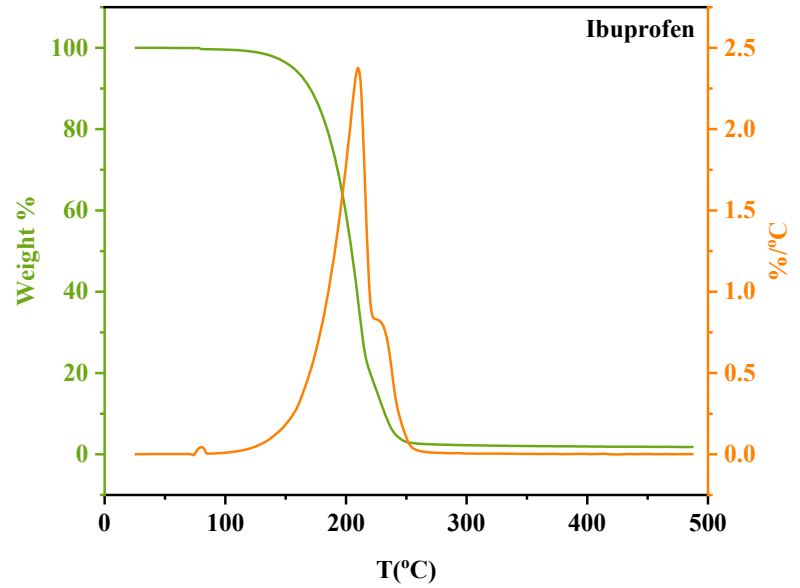


Figure 5 a: TGA / DSC analysis of zeolite P.

The ibuprofen content in the zeolite P-ibuprofen composite was determined using thermogravimetric analysis. Pure ibuprofen showed a pronounced mass loss between 150 and 250°C, leaving virtually no residue, whereas zeolite P alone exhibited a mass reduction of approximately 11 to 12%, attributed mainly to the release of adsorbed water. In contrast, the zeolite P-ibuprofen composite displayed a total mass loss of about 37 to 38% up to 650-700°C. By subtracting the intrinsic weight loss of the zeolite from that of the composite, the ibuprofen loading was calculated to be around 27 wt% (± 2 to 3 wt%), indicating substantial drug uptake within the zeolite structure.

This measured loading capacity closely aligns with the findings of Khodaverdi et al. (2014) [10], who reported that FAU type zeolites (NaX and NaY) could incorporate ibuprofen at levels ranging from 25.28 to 26.32 wt%. The similarity between these values demonstrates that zeolite P despite being synthesized from a natural aluminosilicate precursor such as expanded perlite possesses a drug loading performance comparable to that of conventionally synthesized FAU type zeolites.


Zeolite P
Weight %
%/°C
T(°C)
100
98
96
94
92
90
88
0.07
0.06
0.05
0.04
0.03
0.02
0.01
0.00
-0.01
0
200
400
600
800
1000
1200


Ibuprofen
Weight %
%/°C
T(°C)
100
80
60
40
20
0
2.5
2.0
1.5
1.0
0.5
0.0
0
100
200
300
400
500

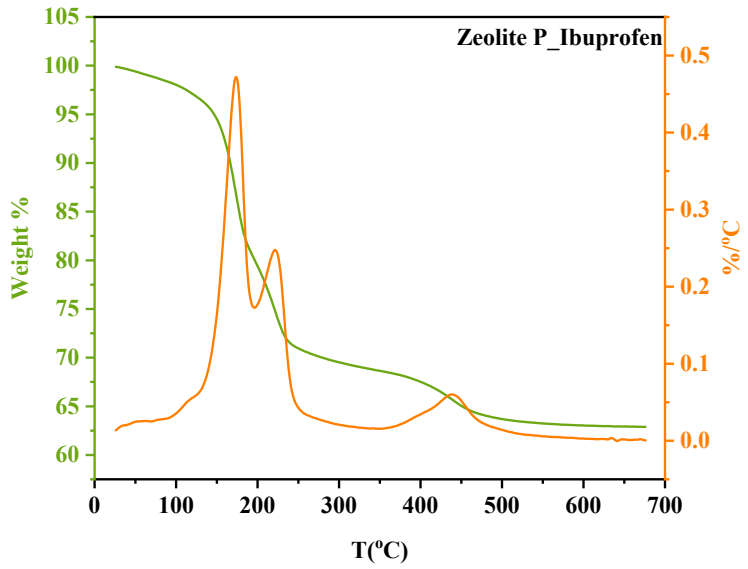


Figure 5 b: TGA and DTG analysis of zeolite P, ibuprofen and zeolite P-ibuprofen.

1.7 N_2 adsorption/desorption isotherm of zeolite P

The textural characteristics of zeolite P were examined through nitrogen adsorption-desorption isotherms, and the resulting data were interpreted using the Brunauer Emmett Teller (BET) and Barrett Joyner Halenda (BJH) models. As summarized in **Table 2**, the BET analysis revealed that zeolite P possesses a specific surface area of 81.21 m^2/g. The total pore volume, obtained from single point adsorption at $P/P_0 = 0.99$, was 0.0476 cm^3/g, and the average pore diameter was measured to be 2.35 nm. According to the IUPAC classification, this pore size confirms the mesoporous nature of the material.

These values exceed those typically reported for Na-P zeolite, which generally displays a surface area of about 45 m^2/g and pore diameters between 1 and 8 nm [11]. The enhanced surface area observed in this work may be attributed to the use of expanded perlite as the aluminosilicate precursor and to the hydrothermal synthesis route, which facilitated the formation of a more open and uniform pore structure. Moreover, in the absence of additional chemical agents during synthesis, the inherent textural features of perlite were retained, contributing to a well ordered and accessible pore network.

Overall, the obtained results demonstrate that the synthesized zeolite P exhibits a highly developed mesoporous framework, making it a promising candidate for adsorption-based processes and drug delivery applications.

Table 2: The BET parameters of zeolite P.

Specific surface area (m^2/g)	81.2138
Total pore volume (cm^3/g)	0.047635
Average pore diameter (nm)	2.3462

The nitrogen adsorption-desorption isotherm presented in **Figure 6a** depicts the variation in the amount of adsorbed N_2 (mmol/g of zeolite) as a function of relative pressure (P/P_0), where P denotes the equilibrium pressure and P_0 the saturation pressure, measured at 196.19°C. The resulting curve corresponds to a type IV isotherm, according to IUPAC classification, which is characteristic of mesoporous materials. The average pore diameter of 2.35 nm further confirms the mesoporous nature of zeolite P.

At very low relative pressures ($P/P_0 < 0.1$), the isotherm shows a linear rise in N_2 uptake, indicating a strong interaction between nitrogen molecules and the zeolite surface through physisorption. The type IV isotherm, accompanied by an H4 hysteresis loop, reveals three distinct adsorption regions:

- ✓ $P/P_0 < 0.1$: corresponding to the initial filling of microporous sites within zeolite P;
- ✓ $0.2 \leq P/P_0 \leq 0.9$: representing multilayer adsorption occurring within the material's mesoporous network;
- ✓ $P/P_0 > 0.9$: associated with capillary condensation in the larger mesopores.

The presence of an H4 hysteresis loop typically linked to slit shaped pores supports the conclusion that zeolite P possesses a combined micro/mesoporous structural framework [12-14].

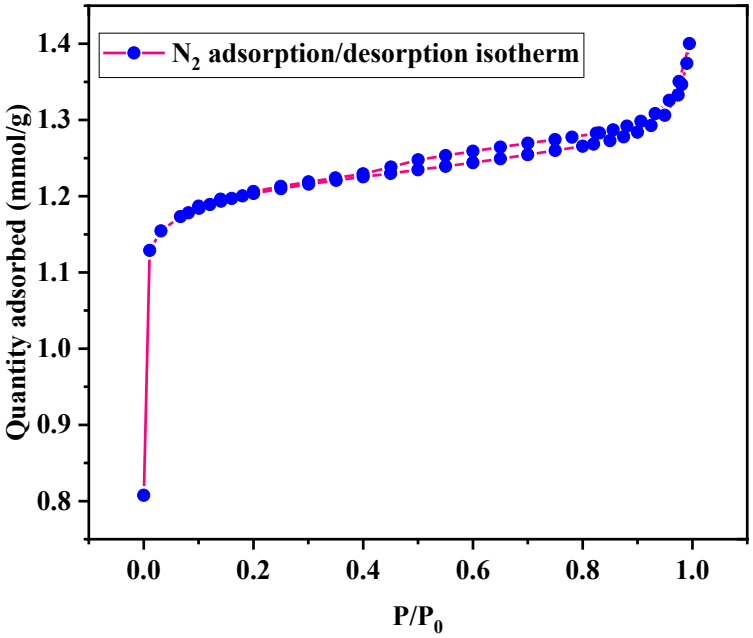


Figure 6 a: N_2 adsorption / desorption isotherm of zeolite P.

The pore size distribution curve of the synthesized zeolite P, derived from the nitrogen adsorption-desorption isotherm data (**Figure 6b**), reveals a narrow pore size distribution, with most pores concentrated within the 2 to 10 nm range. The pronounced peak at pore diameters below 10 nm indicates the dominance of mesopores, consistent with the type IV isotherm and the H4 hysteresis loop observed in the corresponding adsorption–desorption profile (**Figure 6a**).

These findings confirm that the synthesized zeolite P exhibits a mesoporous framework characterized by slit like pores that form between aggregated crystalline platelets. This mesoporosity contributes to the material's relatively high specific surface area (81.12 m^2/g) and enhances molecular diffusion and adsorption processes. The narrow pore distribution further suggests a uniform and well-organized pore system, which is advantageous for applications involving controlled drug loading and release. Overall, the BJH (Barrett Joyner Halenda) analysis demonstrates that the hydrothermally synthesized zeolite P from expanded perlite possesses a homogeneous mesoporous network, consistent with the structural features typically associated with zeolite P.

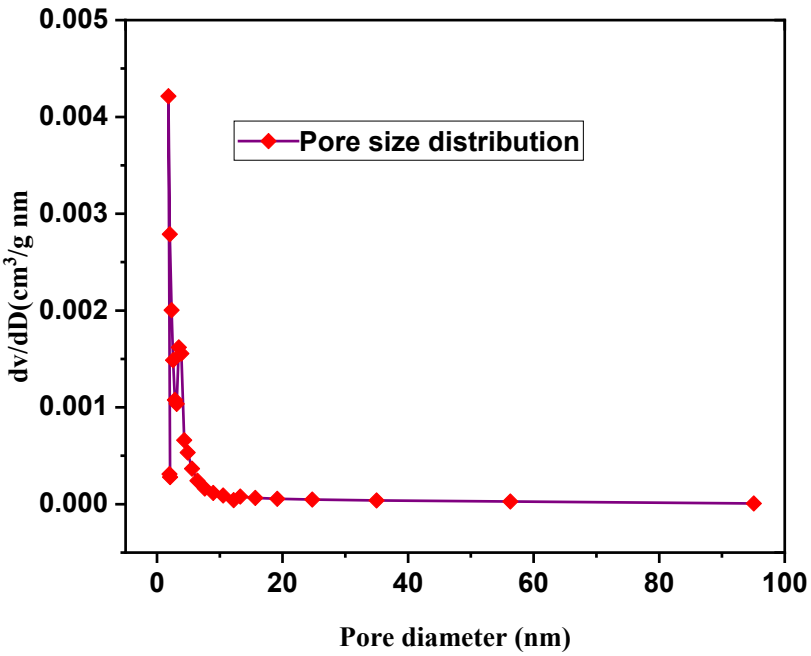


Figure 6 b: Pore size distribution of zeolite P.

2 Theoretical calculations: DFT and molecular docking studie

2.1 DFT calculations results of ibuprofen

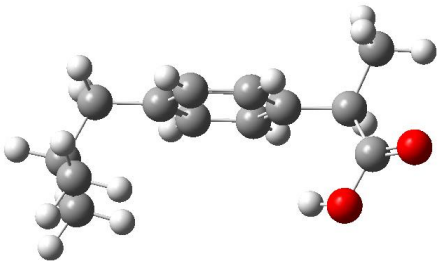
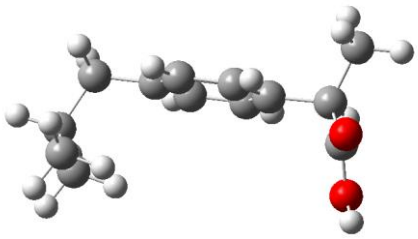
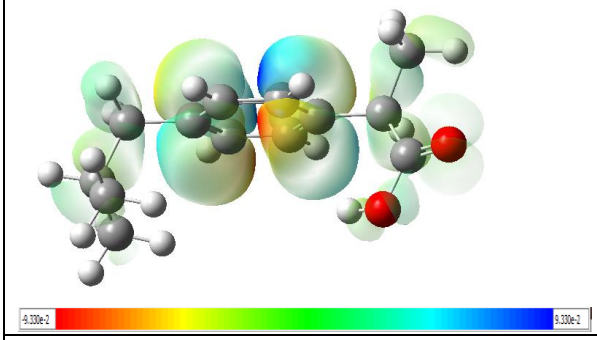
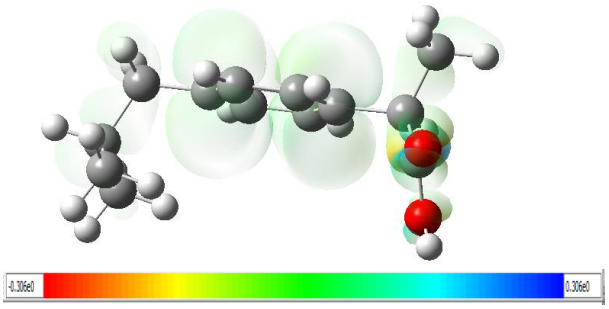
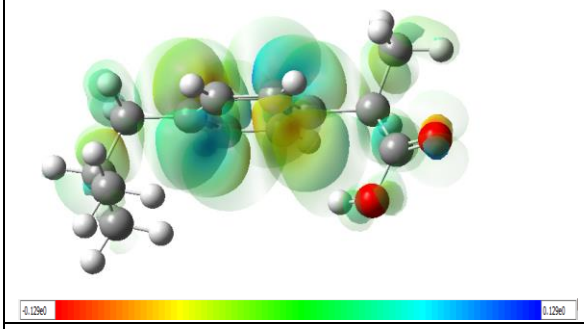
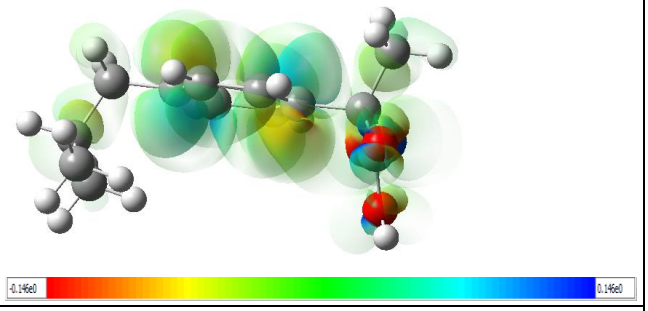
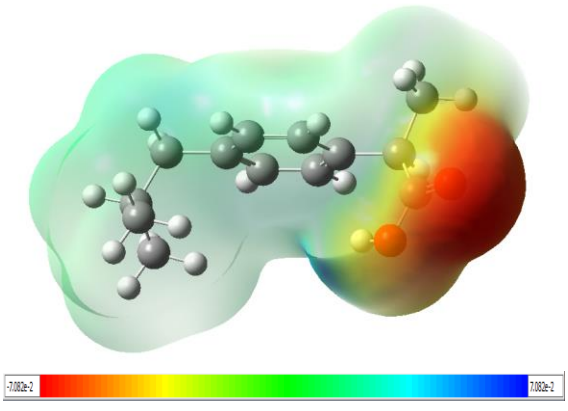
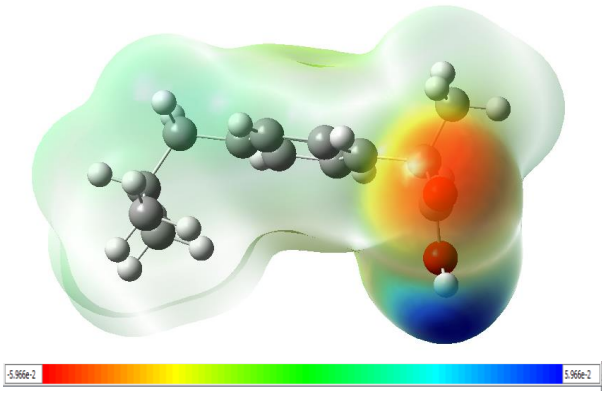
Quantum chemical calculations were carried out using the Gaussian 09 software package, and the resulting data were examined and visualized with GaussView 6.0. The optimized molecular geometry of ibuprofen was obtained using Density Functional Theory (DFT) at the B3LYP/6-311G(d,p) level. The computed values of E_{HOMO}, E_{LUMO}, ΔE, η, δ, and μ (chemical potential) are illustrated in **Figure 7**, while the thermochemical and electronic parameters are summarized in **Tables 3** and **4**.

The energies of the lowest unoccupied molecular orbital (LUMO), which represent the electron accepting capability of the molecule, were calculated to be -0.01329 eV, -0.01783 eV, -0.00975 eV, and -0.01047 eV for ibuprofen structures 1 through 4, respectively. Conversely, the highest occupied molecular orbital (HOMO), reflecting electron donating ability, exhibited the energies of -0.2413 eV, -0.23665 eV, -0.23424 eV, and -0.23385 eV for the same sequence of structures.

The corresponding HOMO-LUMO energy gaps (ΔE) were determined as 0.22801 eV, 0.21882 eV, 0.22449 eV, and 0.22338 eV for ibuprofen 1 and 4, respectively. Among these, ibuprofen 2 presented the smallest gap, suggesting enhanced chemical reactivity and reduced molecular stability. This observation is further supported by the calculated chemical hardness (η) values were 0.1140 eV, 0.1094 eV, 0.1122 eV, and 0.1117 eV, where ibuprofen 2 again shows the lowest value, indicating a greater propensity for electronic reactivity. The chemical potential (μ) values measured as -0.1273 eV, -0.12724 eV, -0.11225 eV, and -0.11169 eV show that ibuprofen 1 and 2 possess nearly identical potentials, slightly lower than those of structures 3 and 4.

Additionally, the chemical softness (δ) values were calculated to be 8.7715 eV, 9.1399 eV, 8.9091 eV, and 8.9534 eV with ibuprofen 2 displaying the highest softness further confirming its increased ability to accept electrons and enhanced chemical reactivity.

Overall, the computational findings demonstrate that ibuprofen 2 is the least stable and the most chemically reactive of the four investigated structures, based on its lowest HOMO-LUMO gap, reduced hardness, and highest softness **[15, 16]**.

	
Ibuprofen 1	Ibuprofen 2
	
HOMO	HOMO
	
LUMO	LUMO
	
MEP	MEP

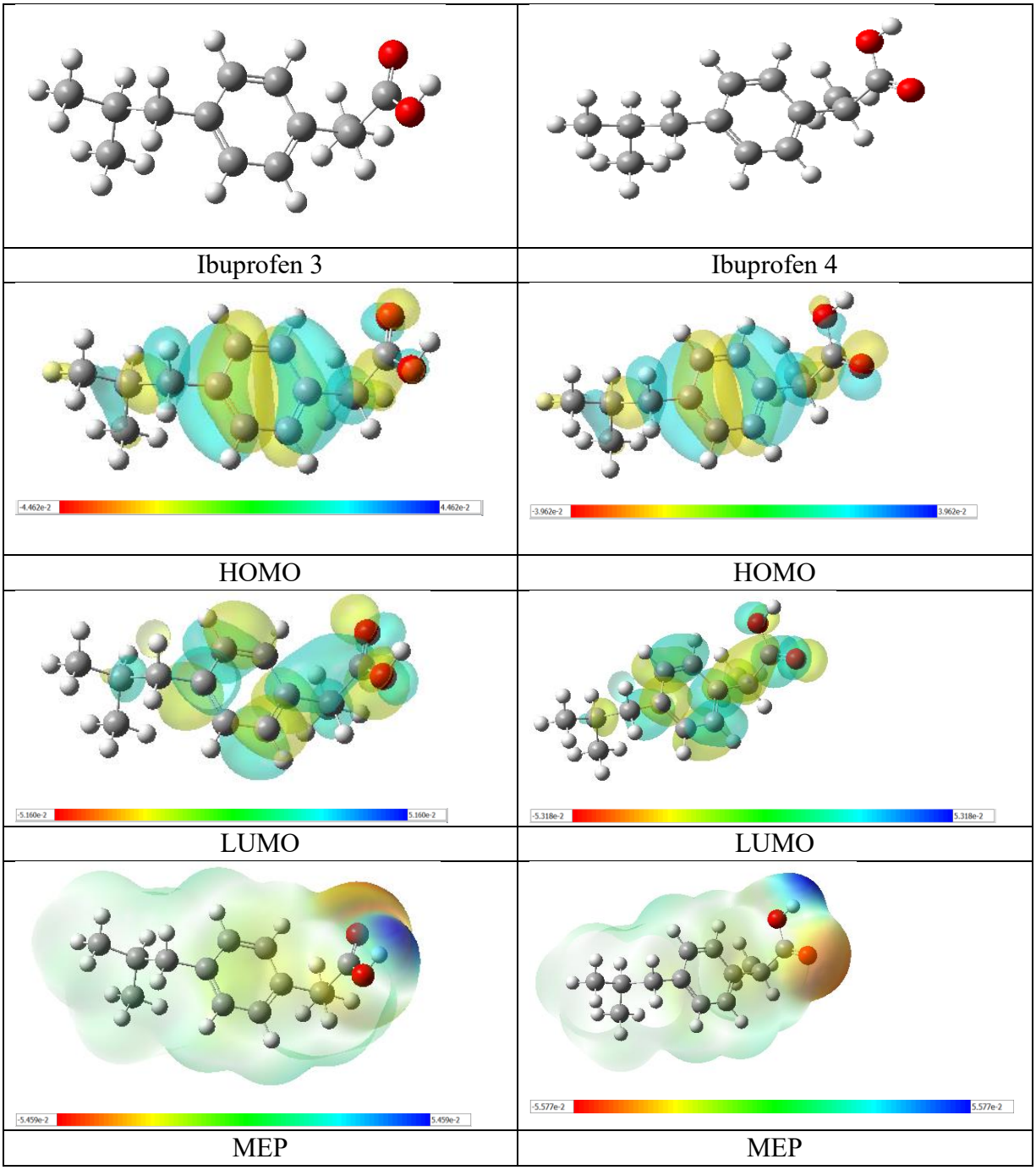


Figure 7: The geometry optimization using DFT calculations of ibuprofen.

Table 3: The obtained results of the quantum chemical parameters of ibuprofen molecule using the DFT-B3LYP-6-311G (d, p) method.

	Ibuprofen 1	Ibuprofen 2	Ibuprofen 3	Ibuprofen 4
E_{HOMO} (eV)	-0.2413	-0.23665	-0.23424	-0.23385
E_{LUMO} (eV)	-0.01329	-0.01783	-0.00975	-0.01047
ΔE (eV)	0.22801	0.21882	0.22449	0.22338
η (eV)	0.114005	0.10941	0.112245	0.11169
δ (eV)	8.771545	9.139932	8.909082	8.953353
Cp (eV)	-0.1273	-0.12724	-0.112245	-0.11169

The thermochemical properties of the various ibuprofen conformations obtained from the DFT calculations are presented in **Figure 7**, providing insight into the chemical and thermal behavior of each optimized molecular structure.

Table 4: The thermochemistry and electronic properties of ibuprofen molecule using the DFT-B3LYP-6-311G (d, p) method.

	Ibu 1	Ibu 2	Ibu3	Ibu 4
Zero-point correction (Hartree/particle)	0.284612	0.287290	0.285181	0.285169
Thermal correction to energy	0.300281	0.302734	0.300890	0.300872
Thermal correction to enthalpy	0.301225	0.303678	0.301834	0.301816
Thermal correction to Gibbs free energy	0.239789	0.243159	0.240560	0.240482
Electronic energy (Hartree)	-656.736528	-656.526815	-656.734302	-656.73237
Dipole moment (Debye)	6.011217	1.604113	1.404092	1.902141
Polarizability α (a.u)	182.401619	137.130096	141.744043	142.056640

2.2 Molecular docking results of ibuprofen

The molecular docking analysis of ibuprofen, shown in **Figure 8**, was employed to investigate interaction mechanisms between the ligand and the 5F1A protein, as well as to estimate the binding

affinity using Auto Dock Vina. The simulation produced a binding energy of -7.2 kcal/mol, indicating a strong binding affinity and favorable interaction between ibuprofen and the receptor.

The docking results indicated that ibuprofen forms multiple van der Waals interactions with the amino acid residues SER A:335, ARG A:120, MET A:522, PHE A:518, TRP A:387, TYR A:348, and PHE A:381. A carbon-hydrogen bond is additionally observed with SER A:530.

Furthermore, π type interactions were identified, including π-σ interactions (highlighted in purple) with ALA A:529 and LEU A:362, and an amide-π stacked interaction (shown in pink) involving GLY A:526. The ligand additionally established alkyl interactions with VAL A:349, VAL A:523, LEU A:531, VAL A:116, and TYR A:355, thereby enhancing the stability of the complex.

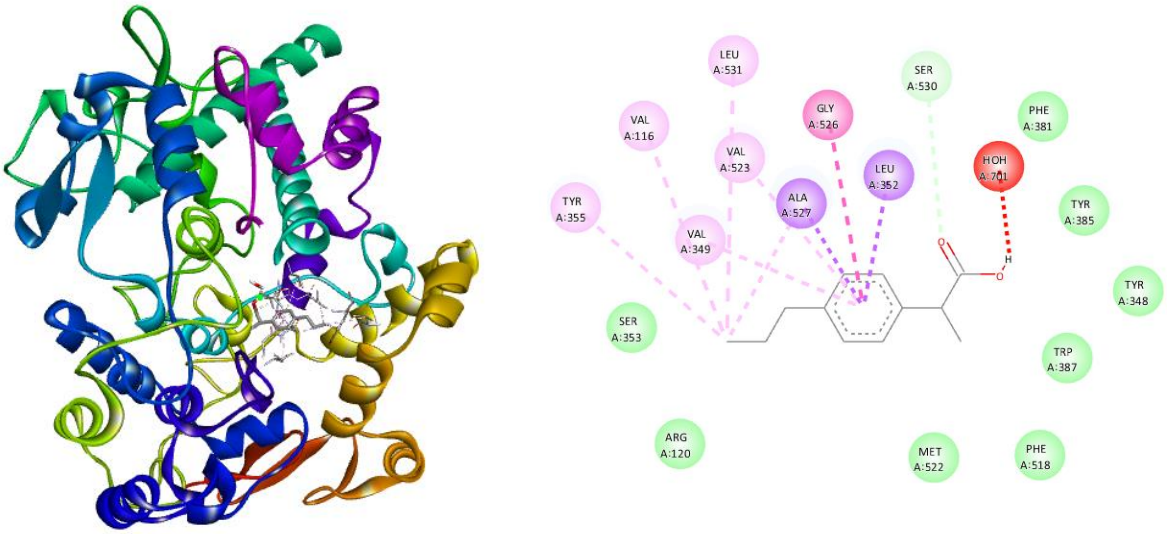


Figure 8: Interactions types between ibuprofen and 5f1a.

Table 5: Binding affinity and interaction types between ibuprofen and 5f1a receptor.

Binding affinity (Kcal/mol)	Amino acid	Interaction
-7.2	SER A:335, ARG A:120, MET A:522, PHE A:518, TRP A:387, TYR A:348 and PHE A:381	Van Der Waals
	SER A:530	carbon hydrogen bond
	ALA A:529 and LEU A:362	Pi-sigma
	GLY A:526	amide-Pi stacked
	VAL A:349, VAL A:523, LEU A:531, VAL A:116 and TYR A:355.	alkyl, Pi alkyl

3. Drug release profiles

Figure 9 presents the ibuprofen release profiles in a simulated gastrointestinal environment, at pH 1.2 representing the gastric medium and pH 6.8 representing the intestinal medium. The bleu curve corresponds to the control test (pure ibuprofen), which showed a rapid drug release in the acidic medium, with 27.65% of ibuprofen released during the initial 2 hours. In comparison, the ibuprofen-zeolite P matrix (pink curve) released 44.01%, while the ibuprofen-zeolite P-Ag matrix (green curve) exhibited the highest release rate of 49.66% under the same conditions.

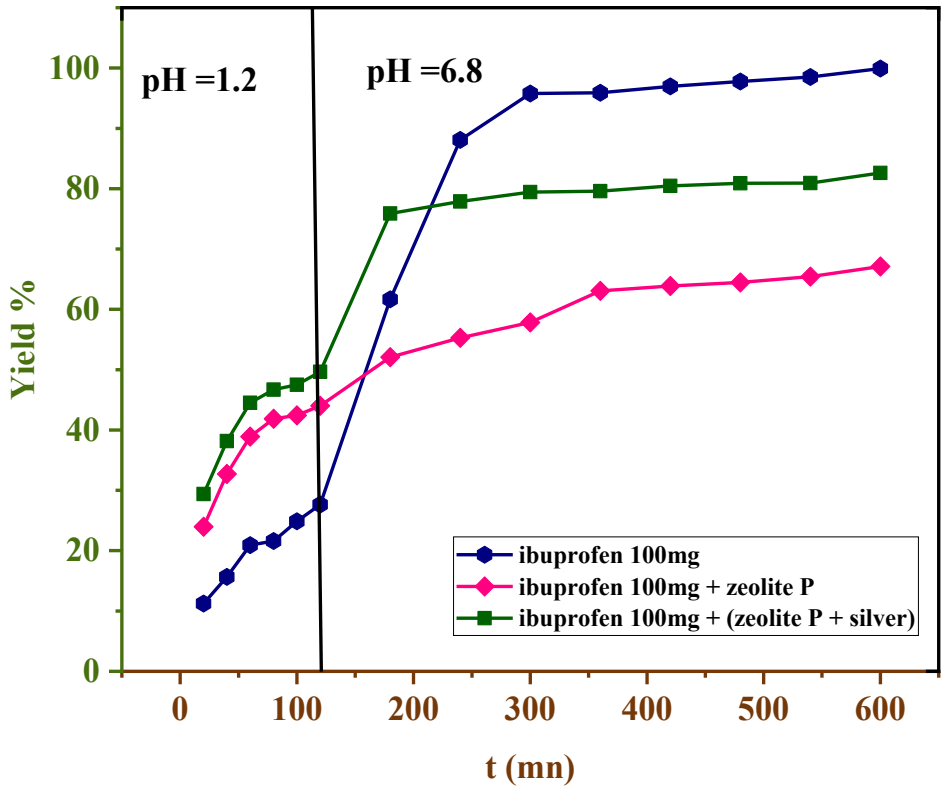


Figure 9: Ibuprofen release profiles in simulated gastrointestinal medium (v = 900ml, speed = 100rpm, pH = 1.2 for 2h and 6.8 for 8h).

After two hours of dissolution testing in the intestinal pH environment (pH 6.8), the samples exhibited a progressive increase in drug release over the time range of 2 to 10 hours. The cumulative amounts of ibuprofen released in the intestinal medium were 99.90% for the control sample, 67.11% for the ibuprofen-zeolite P matrix, and 82.62% for the ibuprofen-zeolite P-Ag matrix. These findings demostrate that silver modification of zeolite P via the photodeposition method enhanced the drug release behavior of the composite in the simulated gastrointestinal medium when compared to the unmodified zeolite P matrix.

For comparison, Khodaverdi et al. (2014) [10] reported the release of ibuprofen from FAU-type zeolites (NaX and NaY), showing 30 to 35% release at gastric pH (1.2) within 2 hours, followed by 70 to 80% cumulative release at intestinal pH (6.8) over 8 hours. In our study, the ibuprofen-

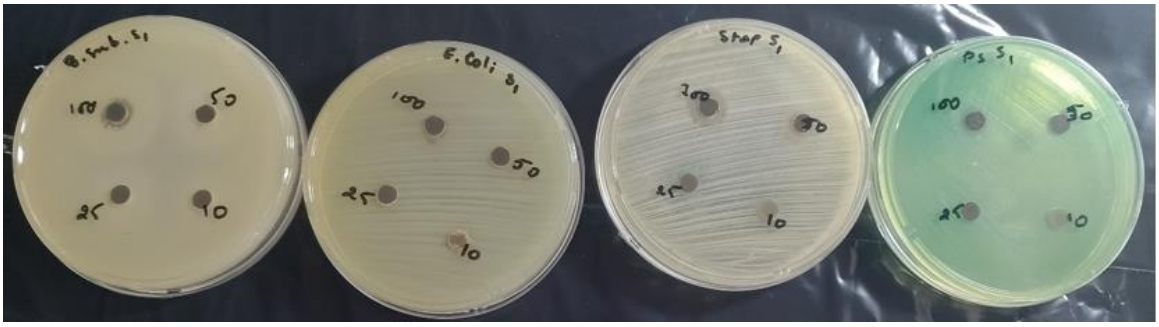
zeolite P system exhibited 44.01% release at pH 1.2 and 67.11% at pH 6.8, while the silver-modified zeolite P demonstrated enhanced release behavior with 49.66% at pH 1.2 and 82.62% at pH 6.8. These findings suggest that zeolite P, especially when modified with silver, provides a competitive or superior release profile compared to FAU-type zeolites, particularly in acidic gastric conditions.

4. Antimicrobial activity of zeolite P

4.1 The antibacterial activity:

According to the results obtained from the agar well diffusion method, presented in the figure below and summarized in the table, limited inhibition zones were detected around the wells, suggesting that zeolite P (S1) can diffuse through the agar medium and inhibit bacterial growth at high concentrations. For the Gram-positive strains, the inhibition zones were 14 mm for *Staphylococcus aureus methicillin* resistant (MRSA) ATCC 43300 and 11 mm for *Bacillus subtilis* ATCC 6633. For the Gram-negative strains, the inhibition zones were 9 mm for *Pseudomonas aeruginosa* ATCC 27853 and 8 mm for *Escherichia coli* ATCC 7839 at a concentration of 100 mg/ml. In contrast, the silver doped zeolite P (S-Ag) exhibited enhanced antibacterial activity, producing significantly larger inhibition zones against both Gram positive and Gram-negative bacteria across all tested concentrations. The increase in inhibition zone diameter at higher concentrations demonstrated that the antibacterial activity of both zeolite P and zeolite P-Ag was dose dependent.

(a)



(b)

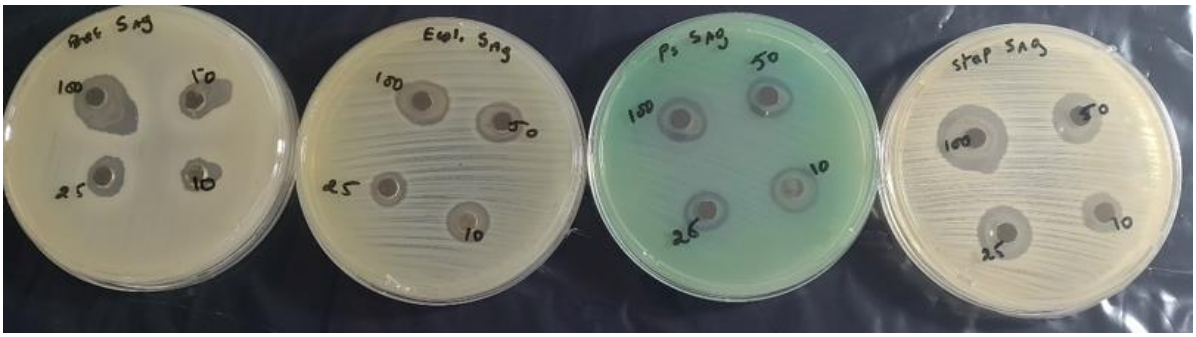


Figure 10: The antibacterial activity of **(a)** zeolite P (S_1) and **(b)** dopped zeolite P with 1% silver (S Ag)

The measured diameters of the inhibition zones, presented in the table, confirm that zeolite P possesses antibacterial activity and is capable of inhibiting bacterial growth.

Table 6: The diameters of the inhibition zones of zeolite P (S_1) and dopped zeolite P (S Ag).

		100 mg/ml	50 mg/ml	25 mg/ml	10 mg/ml
Bacillus subtilis ATCC 6633	S_1	11 mm	/	/	/
	S Ag	23 mm	18 mm	13 mm	12 mm
Pseudomonas aeruginosa ATCC 27853	S_1	9 mm	7 mm	/	/
	S Ag	16 mm	15 mm	14 mm	13.5 mm
Staphylococcus aureus methicillin resistant (MRSA)ATCC 43300	S_1	14 mm	9 mm	7 mm	/
	S Ag	23 mm	17 mm	16 mm	12 mm
Escherichia coli ATCC 7839	S_1	8 mm	7.5 mm	/	/
	S Ag	18 mm	16 mm	11 mm	13.5 mm

The minimum inhibitory concentration (MIC) was defined as the lowest concentration of zeolite capable of inhibiting bacterial growth after 24 hours of incubation, as determined using the 96 well microplate dilution method. The obtained results are presented in the table below.

These findings demonstrate that zeolite P inhibited bacterial growth only at high concentrations, consistent with the inhibition zones observed in the agar well diffusion assay and further confirmed by the MIC test. In contrast, the silver doped zeolite P (1% Ag) exhibited a MIC value of 0.625 mg/ml, indicating a significantly enhanced antibacterial effect. However, at this concentration, the material showed no inhibitory activity against *Bacillus subtilis* ATCC 6633, as presented in the **table 7**.

Table 7: the minimum inhibitory concentration MIC of zeolite P

	Sample	MIC
Escherichia coli ATCC 7839	S_1	/
	S Ag	0.625 mg/ml
Pseudomonas aeruginosa ATCC 27853	S_1	/
	S Ag	0.625 mg/ml
Staphylococcus aureus methicillin resistant (MRSA)ATCC 43300	S_1	/
	S Ag	0.625 mg/ml
Bacillus subtilis ATCC 6633	S_1	/
	S Ag	/

Table 8: Comparison of the antibacterial activity from literature

Carrier	C of sample	Silver loading method	microorganism	Zone of inhibition (mm)	MIC (mg/ml)	Reference
Synthesized zeolite Na-P from expanded perlite	100 (mg/ml)	Photodeposition 1%Ag ($AgNO_3$ aqueuse, 300W Xe lamp, 2h)	S aureus (MRSA, ATCC 43300), Bacillus subtilis (ATCC 6633), E coli (ATCC 7839), Pseudomonas aeruginosa (ATCC 27853).	23 23 18 16		**This study**
Na-Y zeolite	0,12 g	Ion exchange 25%Ag	E coli S aureus	18.3 18.3	0.25 0.25	**[17]**
Zeolite X	0.016 mg/ml	Ion exchange 42.7%Ag	E coli Pseudomonas Bacillus S aureus	/ / / /	0.064 0.016 0.064 0.032	**[18]**
Faujasite zeolite X	0.01 to 0.1 mg/ml	Ion exchange 9.75%Ag	E coli Bacillus	/ /	0.3 0.3	**[19]**
Faujasite zeolite Y	0.01 to 0.1 mg/ml	Ion exchange 9.75%Ag	E coli Bacillus	/ /	0.2 0.2	**[19]**

4.2 The minimum antifungal concentration MFC of zeolite P (S_1) and dopped zeolite by silver (S Ag):

The results presented in **Figure 11**, obtained from the determination of the minimum fungicidal concentration (MFC) using the 96-well microdilution method, indicate that both zeolite P and silver-doped zeolite P (1% Ag) exhibited antifungal activity against *Aspergillus niger* (ATCC 16888) and *Penicillium expansum* (ATCC 7861). The corresponding MFC values are summarized in the table below.

(a) **(b)**



Figure 11: determination of the MFC of zeolite P (S) and dopped zeolite P with silver (S_2 Ag)**.**

Zeolite P exhibited a moderate minimum fungicidal concentration (MFC) of 25 mg/ml against both *Aspergillus niger* (ATCC 16888) and *Penicillium expansum* (ATCC 7861). This relatively high value may be attributed to the low solubility of zeolite P in distilled water, which limits its dispersion and interaction with fungal cells in the medium.

In contrast, the modified zeolite P doped with 1% silver showed significantly lower MFC values, measured at 0.39 mg/ml for *Aspergillus niger* and 0.024 mg/ml for *Penicillium expansum*. These results indicate that silver modification substantially enhanced the antifungal activity of zeolite P, suggesting its promising potential for biomedical applications.

Table 9: the Minimal antifungal concentration (MFC) of zeolite P

	Sample	MFC
Aspergillus Niger (ATTC 16888)	S_1	25 mg/ml
	S Ag	0.39 mg/ml
Penicillium Expansum (ATTC 7861)	S_1	25 mg/ml
	S Ag	0.024 mg/ml

When compared with literature, Ag exchanged zeolite X containing 42.7 wt% Ag reported an MFC of 0.016 mg/ml against A. niger [18], while Ag zeolite A with 25.6 wt% Ag showed an MFC of 0.031 mg/ml against related fungal strains. Although these studies used 25 to 40 times more silver than our material, the antifungal efficiency of the Ag zeolite P prepared in this work is of the same order of magnitude. This clearly indicates that the photodeposition route leads to highly active Ag^0 nanoparticles with superior silver utilization efficiency. Therefore, zeolite P synthesized from natural perlite and modified with only 1 wt% Ag represents a cost effective, low silver alternative to conventional Ag zeolites, while maintaining strong antifungal properties against both Aspergillus niger and Penicillium expansum.

5 Conclusion

Zeolite P was successfully prepared from expanded perlite, a natural aluminosilicate source, using the hydrothermal method. The synthesized zeolite P exhibited efficient drug loading and release properties of ibuprofen, which used as a model anti-inflammatory drug in simulated gastrointestinal fluids. To enhance its antimicrobial activity and drug release rate, zeolite P was further modified by photodeposition with 1% silver.

As a novel drug carrier in the biopharmaceutical field, zeolite P facilitates the controlled release of ibuprofen in the gastrointestinal environment, thereby protecting the drug from gastric acidity and, conversely, to shield the stomach from the acidic nature of ibuprofen, which is known to cause gastric irritation and ulcers.

Furthermore, DFT/B3LYP/6-311G calculations were performed to predict the molecular properties of four ibuprofen conformations, while molecular docking simulations were carried out to explore the binding affinities and interaction types between ibuprofen (ligand) and the 5F1A protein (receptor).

References

[1] H. Ghaedrahmat, "Synthesis of zeolite / ZIF-8 composite as a catalyst for aldol condensation reaction," Journal of Nanopores Systems, 2025.

[2] H. Ghaedrahmat and al, "Synthesize and characterization of ZIF-8 / NaP zeolite composites as a stable acid-base catalyst for organic reactions," Polyhedron, vol. 236, no. March, p. 116372, 2023.

doi: 10.1016/j.poly.2023.116372.

[3] J. Li and al, "Regulation of the Si/Al ratios and Al distributions of zeolites and their impact on properties," Chemical Science, pp. 1935–1959, 2023.

doi: 10.1039/d2sc06010h.

[4] Y. K. Krisnandi and al, "Synthesis and characterization of ZSM-5 zeolite from dealuminated and fragmentated bayat- klaten natural zeolite". Journal of Physics: Conf. Series 1095, 2018.

doi :10.1088/1742-6596/1095/1/012044.

[5] P. F. Corregidor and al, "Green synthesis of ZSM-5 zeolite prepared by hydrothermal treatment of perlite. effect of chemical composition and characterization of the product," Science of Advanced Materials, vol. 6, pp. 1203–1214, 2014.

doi: 10.1166/sam.2014.1894.

[6] M. Khatamian and al, "Synthesis and characterization of zeolite A , - Fe $_3$ O $_4$ / zeolite A , and - Fe $_2$ O $_3$ / zeolite A nanocomposites and investigation of their arsenic removal performance," J. Iran. Chem. Soc., vol. 20, no. 7, pp. 1657–1670, 2023.

doi: 10.1007/s13738-023-02787-w.

[7] M. Kragović and al., "Influence of alginate encapsulation on point of zero charge (pH_{pcz}) and thermodynamic properties of the natural and Fe (III)-modified zeolite," Procedia Manuf., vol. 32, pp. 286–293, 2019.

doi: 10.1016/j.promfg.2019.02.216.

[8] M. Nicholas and al, “Thermal stability studies of zeolites A and X synthesized from South African coal fly ash,” Res Chem Intermed, pp. 575–582, 2015.

doi: 10.1007/s11164-013-1211-3.

[9] W. Henao-Sierra and al, “Water vapor adsorption performance of Ag and Ni modified 5A zeolite,” Microporous Mesoporous Mater., vol. 265, no. February, pp. 250–257, 2018.

doi: 10.1016/j.micromeso.2018.02.036.

[10] E. Khodaverdi and al, “Evaluation of synthetic zeolites as oral delivery vehicle for anti-inflammatory drugs,” Iran J Basic Med Sci, no. 3, 2014.

[11] Z. Mortezaei and al, “Synthesis and characterization of functionalized NaP Zeolite@CoFe2O4 hybrid materials: a micro–meso-structure catalyst for aldol condensation,” Research on Chemical Intermediates, pp. 2169–2193, 2020.

doi: 10.1007/s11164-020-04085-z.

[12] M. Thommes and al., “Physisorption of gases , with special reference to the evaluation of surface area and pore size distribution (IUPAC Technical Report),” Pure Appl. Chem, vol. 87, pp. 1051–1069, 2015.

doi: 10.1515/pac-2014-1117.

[13] K. S. W. SING, “Provisional international union of pure and applied chemistry commission on colloid and surface chemistry subcommittee on reporting gas adsorption data * reporting physisorption data for gas / solid systems with special reference to the determination of surface area and porosity,” Pure & Appl.Chem, vol. 54, no. 11, 1982.

[14] M. D. U. Donohue and G. L. Aranovich, “Classification of Gibbs adsorption isotherms,” Advances in Colloid and Interface Science, pp. 137–152, 1998.

[15] O. E. Oyeneyin and al, “Structural modification of ibuprofen as new nsaids via dft , molecular docking and pharmacokinetics studies,” Int. J. Adv. Eng. Pure Sci, vol. 33, no.

4, pp. 614–626, 2021.

doi: 10.7240/jeps.928422.

[16] Y. Wei and P. Liu, “Analysis of the nature of interaction between AlN nanocage and ibuprofen using quantum chemical study,” Structural Chemistry, pp. 1685–1692, 2021.

doi: 10.1007/s11224-021-01750-w.

[17] S. Aishah and al, “Amine-functionalized , silver-exchanged zeolite NaY : Preparation , characterization and antibacterial activity,” Appl. Surf. Sci., vol. 360, pp. 121–130, 2016.

doi: 10.1016/j.apsusc.2015.11.010.

[18] S. Demirci and al, “Antimicrobial properties of zeolite-x and zeolite-a ion-exchanged with silver , copper , and zinc against a broad range of microorganisms,” Appl Biochem Biotechnol, pp. 1652–1662, 2014.

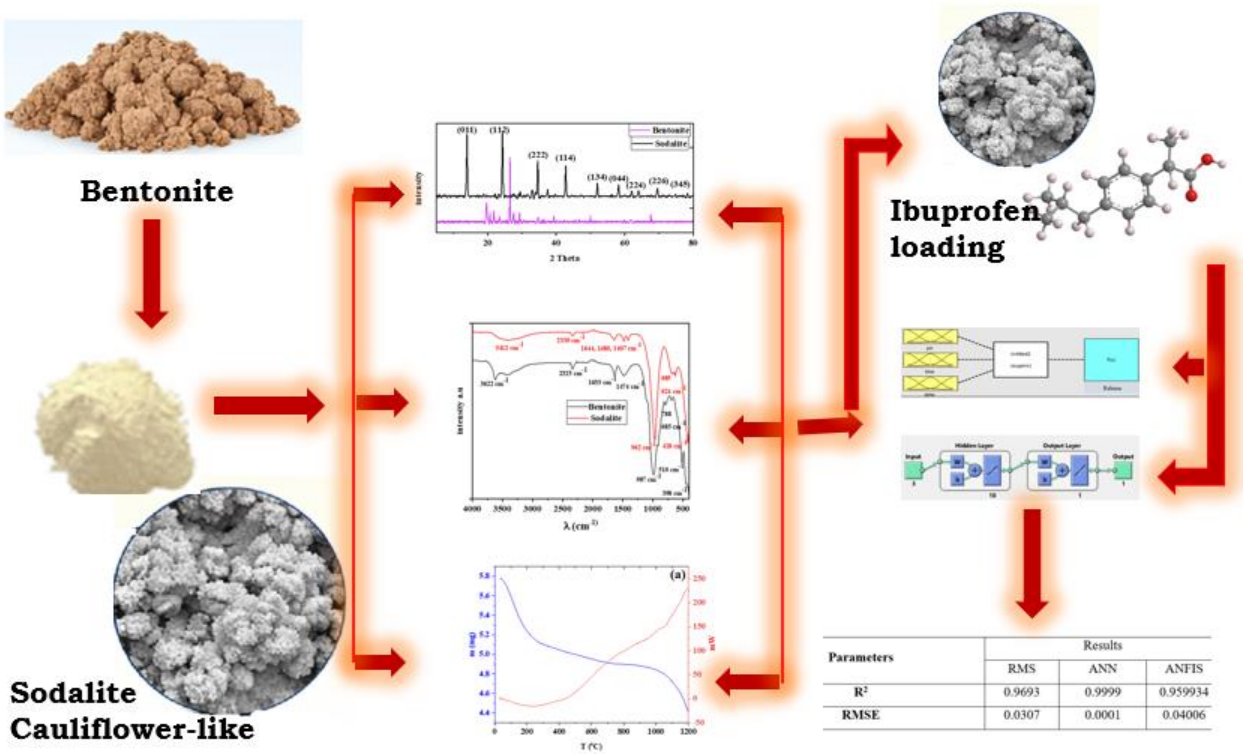
doi: 10.1007/s12010-013-0647-7.

[19] L. Ferreira and al, “Antimicrobial activity of faujasite zeolites doped with silver,” Microporous Mesoporous Mater., vol. 160, pp. 126–132, 2012.

doi: 10.1016/j.micromeso.2012.05.006.

Chapter 4

From Maghnite to Sodalite: Characterization and Comparative Artificial Intelligence Based Modeling of Ibuprofen Release using RSM, ANN and ANFIS.



The objective of the present work is the preparation of sodalite zeolite using raw bentonite (Maghnite) as a low-cost and environmentally sustainable aluminosilicate source, followed by an evaluation of its suitability as a delivery matrix for the controlled release of ibuprofen under simulated physiological conditions. To enable a systematic analysis and optimization of both the synthesis process and drug release behavior, an integrated modeling strategy combining statistical methods and artificial intelligence techniques was adopted. A Box-Behnken experimental framework was established with the aid of Design-Expert software, and the resulting experimental data were interpreted using response surface methodology (RSM). Furthermore, advanced computational intelligence tools, including artificial neural networks (ANN), adaptive neuro-fuzzy inference systems (ANFIS), and genetic algorithms (GA), were employed to model system responses, predict performance trends, and identify optimal operating conditions. A comparative evaluation of these modeling approaches was carried out to determine the most reliable and effective method for accurately describing and optimizing the ibuprofen release characteristics of the synthesized sodalite zeolite.

1. Results and discussion

1.1 Physico-chemical characterizations of synthetized sodalite

1.1.1 The XRD analysis

The phase composition and crystallographic features of the sodalite obtained from bentonite were examined by X-ray diffraction (XRD), with the corresponding diffraction profile presented in **Figure 1**. Peak identification and phase assignment were carried out using HighScore Plus software through comparison of the experimental diffraction data with reference patterns from the International Centre for Diffraction Data (ICDD) database. The crystalline phase was identified as sodalite type zeolite, confirmed using the reference file **PDF: 96-900-3329**.

The characteristic diffraction peaks observed at 2θ values of 13.9443°, 24.3114°, 34.6243°, 37.5456°, 42.7697°, 51.9495°, 58.2352°, 62.2071°, 63.9943°, 69.4617°, and 74.877° correspond to the (011), (112), (123), (114), (134), (044), (244), (235), (226), and (345) planes, respectively. These peaks match well with the reference pattern, confirming the successful transformation of bentonite into sodalite.

The sharp and well-defined peaks indicate that the synthesized material possesses a high degree of crystallinity. Overall, the results demonstrate the effectiveness of the applied synthesis conditions in converting the clay mineral structure into a zeolitic sodalite framework.

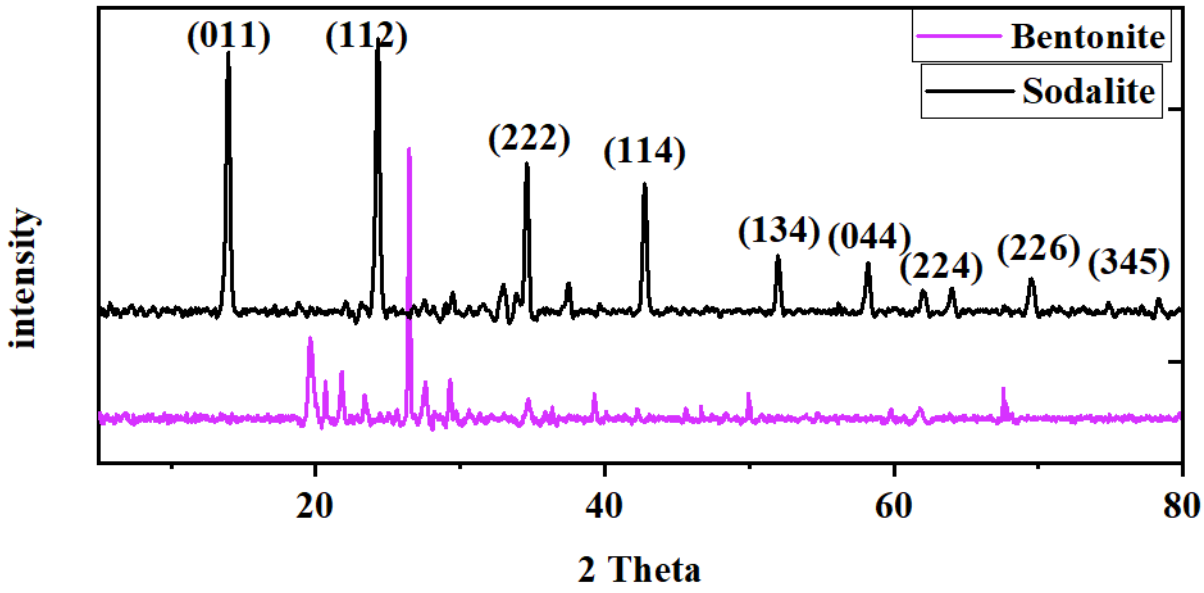


Figure 1: XRD analysis of synthetic zeolite sodalite from bentonite.

1.1.2 The FTIR analysis

The FTIR spectrum presented in **Figure 2**, shows several structural transformations of maghnite (raw bentonite of Maghnia, Algeria) into sodalite under fusion alkaline and hydrothermal treatment in basic medium of NaOH and without any adding of chemical product.

Fourier Transform Infrared (FTIR) spectroscopy was utilized to analyze the structural changes that occurred during the hydrothermal transformation of raw bentonite clay into sodalite zeolite. The spectra, collected over the wavenumber range of 4000 to 400 cm^{-1}, displayed characteristic vibrational bands corresponding to the molecular and structural features of both materials, thereby confirming the successful conversion from a layered clay structure to a three-dimensional zeolitic framework.

The FTIR spectrum of the raw bentonite (**Figure 2**, **black curve**) displays the characteristic vibrational features of a dioctahedral smectite. The absorption bands at 3622 cm^{-1} and 916 cm^{-1} correspond to structural O-H stretching and Al-Al-OH bending modes, confirming the dioctahedral nature of the smectite.

Additional peaks at 3670 cm^{-1} and 848 cm^{-1}, assigned to Al-OH-Mg vibrations, along with the weaker band at 788 cm^{-1} associated with Fe^{3+}-OH-Mg bonding, indicate that the bentonite is Mg-rich and relatively depleted in Fe^{3+}. The bands located at 628 cm^{-1} and 670 cm^{-1} arise from Si-O-Al and Si-O-Mg stretching, respectively, suggesting that the octahedral layer charge is primarily generated through the substitution of trivalent cations (Al^{3+}, Fe^{3+}) by divalent Mg^{2+}. The broad band at 3446 cm^{-1} and the peak at 1645 cm^{-1} correspond to O-H stretching and H-O-H bending vibrations of interlayer or adsorbed water. The small feature near 2325 cm^{-1} originates from atmospheric CO_2 incorporated during pellet preparation. Collectively, these bands confirm that the starting material is a dioctahedral smectite dominated bentonite [1, 2].

Following hydrothermal synthesis, the FTIR spectrum of the resulting sodalite (**Figure 2, red curve**) shows clear structural changes that validate the transformation of bentonite into a sodalite type aluminosilicate framework. The strong bands observed in the 624 - 685 cm^{-1} region are characteristic of ring breathing vibrations of tetrahedral and octahedral units, indicating the formation of sodalite cages. The distinct band at 418 cm^{-1} is attributed to Si-O and Al-O bending modes within the newly formed framework, while the peak at 962 cm^{-1} corresponds to internal T-O-T (T = Si, Al) stretching vibrations, which are diagnostic of sodalite. The broad absorption at 3412 cm^{-1} and the peak at 1644 cm^{-1} arise from O-H stretching and bending of water molecules trapped within the sodalite cavities, reflecting the hygroscopic nature of the material. The band at 2330 cm^{-1} is associated with O-C-O vibrations from adsorbed CO_2 on the sample surface. These spectral features collectively confirm the successful conversion of bentonite to sodalite and demonstrate the establishment of its characteristic three dimensional aluminosilicate framework [2-4].

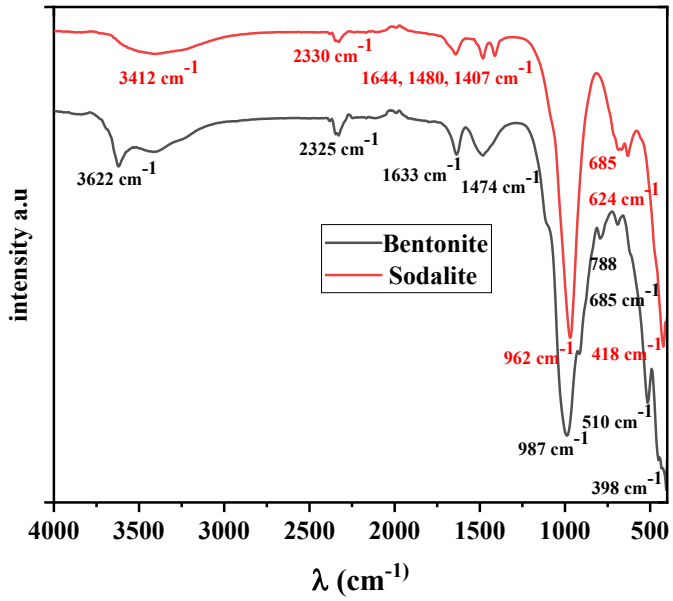


Figure 2: FTIR analysis of synthetic zeolite sodalite from bentonite.

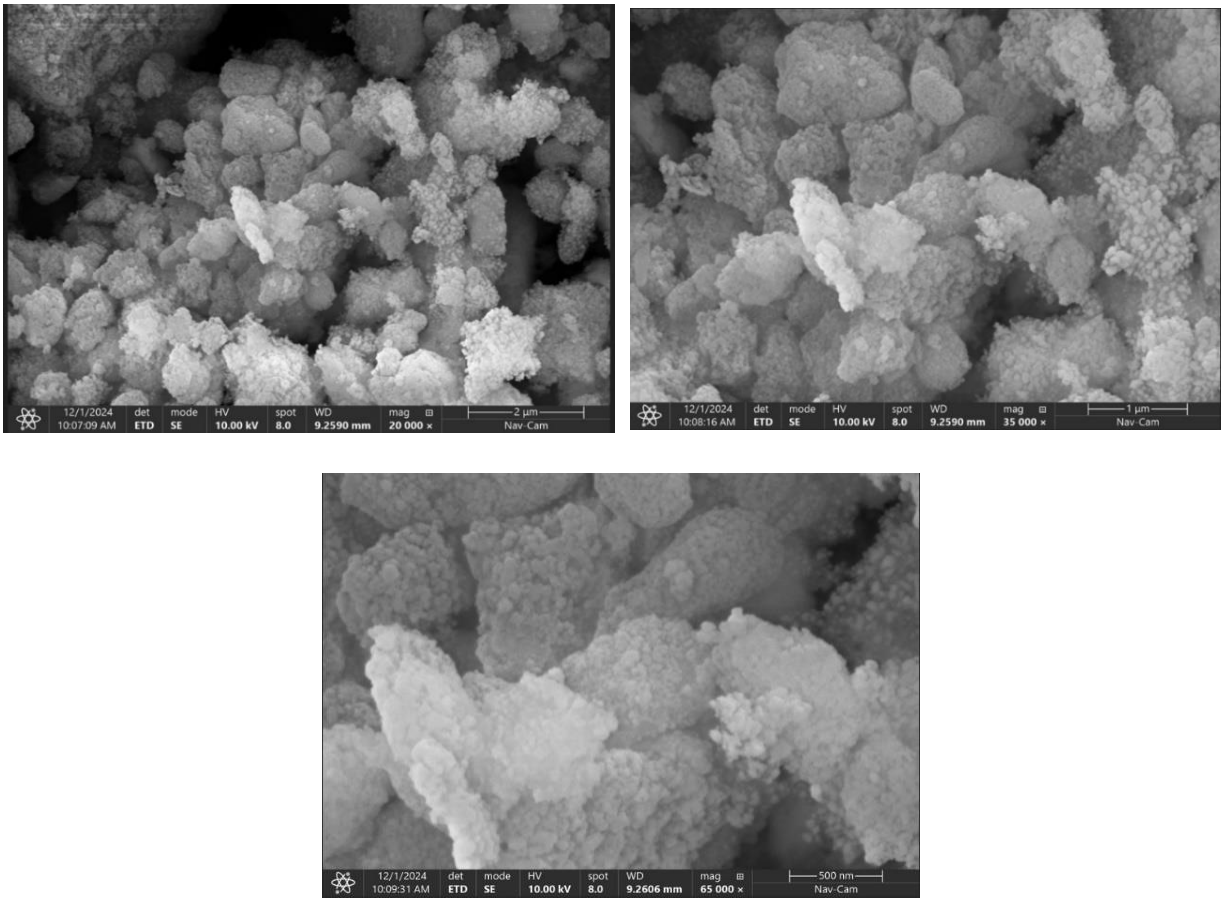
1.1.3 The SEM/EDS analysis

The SEM micrographs of the synthesized sodalite (**Figure 3a**) at different magnifications (2 µm, 1 µm and 500 nm) reveal that the material consists of highly aggregated submicron particles. At the micrometer scale, the product shows compact clusters of irregular grains (cauliflower like clusters), indicating the complete loss of the lamellar morphology typical of the bentonite precursor. As the magnification increases, the images reveal that these aggregates are composed of fine crystallites with rounded outlines and rough surfaces. At 500 nm, individual primary particles can be distinguished, confirming the formation of submicron or partially nanometric crystallites. This granular and agglomerated morphology is consistent with sodalite synthesized under hydrothermal conditions, where rapid nucleation is followed by the clustering of nanosized crystallites. The SEM observations therefore support the formation of fine sodalite particles assembled into dense aggregates [5, 6].

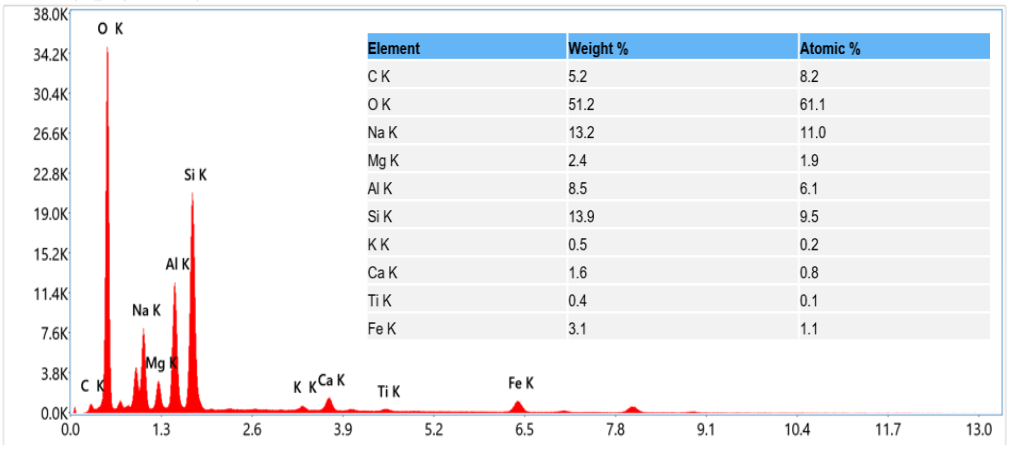
The EDX analysis confirms that the synthesized material is a sodium aluminosilicate zeolite dominated by 51.2% O, 13.9% Si, 8.5% Al and 13.2% Na. The approximate Si/Al = 1.63 ratio close to unity and the high Na content are characteristic of Na-sodalite. The presence of minor Mg, Fe, Ca, K and Ti is attributed to residual impurities from the natural bentonite precursor.

The compositional ratios obtained from EDX analysis in this work are Si/Al = 1.64 and Na/Al = 1.55. These values are higher than those reported in the literature, where Si/Al and Na/Al ratios of 1.34 and 0.48 [7], 1.06 and 1.12 [3], 1.10 and 1.00 [8] have been reported, while [6] indicates Si/Al values below 1.5. The elevated Si/Al ratio obtained in the present study indicates a silica rich sodalite framework, which is attributed to residual silica inherited from the natural bentonite precursor. Similarly, the higher Na/Al ratio reflects enhanced sodium incorporation under strong alkaline synthesis conditions. In contrast, [3] and [8] correspond to near stoichiometric sodalite, whereas [7] represents a Na deficient sodalite. Overall, the EDX results are in good agreement with the typical elemental composition of sodalite synthesized from clay based raw materials reported in the literature.

(a)



(b)



Element	Weight %	Atomic %
C K	5.2	8.2
O K	51.2	61.1
Na K	13.2	11.0
Mg K	2.4	1.9
Al K	8.5	6.1
Si K	13.9	9.5
K K	0.5	0.2
Ca K	1.6	0.8
Ti K	0.4	0.1
Fe K	3.1	1.1

Figure 3: SEM (a) and EDX (b) analysis of synthetic zeolite sodalite from bentonite.

1.1.4 The TGA/DSC analysis

The thermogravimetric analysis TGA and the differential scanning calorimetry DSC results were presented in the **Figure 4** which was revealed the decomposition characteristics and the thermal stability of our synthetized sodalite from raw bentonite via fusion alkaline and hydrothermal treatment, in the temperature range of 33 to 1200°C, ibuprofen from 25 to 488 °C and ibuprofen loaded into sodalite from 32 to 988 °C.

The TGA result of sodalite (**Figure 4 (a)),** was drawing by the blue curve, which was shown four steps of the decomposition of our sodalite. When the DSC analysis was observed by the red color, to understand the chemical processus of this thermal treatment and it was also presented in three stages.

The first step, was presented the mass loss in the temperature range of 33 to 300°C with an amount approximately 11.62% of the total sodalite mass, corresponding to the removal of the physiosorbed H_2O molecules from the sodalite cage structure. This dehydration was indicated the sodalite water content in their structure, and it was confirmed by the presence peak of water molecules in FTIR analysis [9, 10]. It was characterized by the exothermic peak in the DSC which was confirmed the desorbing of water molecules from the external surface of our sodalite [11]. The second step, observed between 300 and 916 °C, showed a slow mass loss of 3.18%, which is attributed to the continued removal of water molecules from the internal structure of the sodalite. This step confirmed the thermal stability of the material. Finally, the third step was identified at high temperatures, from 916 °C to 1200 °C.

This stage corresponded to the thermal decomposition or the formation of new phases within this temperature range, with a mass loss of 8.14%. The process was confirmed by the presence of an exothermic peak in the DSC curve.

According to the TGA-DSC results presented in **Figure 4b**, the TGA curve exhibits three distinct thermal steps. The first step, occurring between 25 and 100 °C, shows no detectable mass loss, confirming the absence of physiosorbed water molecules in the ibuprofen sample. The second step, between 100 and 256 °C, corresponds to the major decomposition event of ibuprofen, during which a substantial reduction in mass is observed. The final stage shows no additional mass loss, indicating the complete degradation of the organic material. The DSC curve displays two endothermic peaks. The first peak, at 79.97 °C, represents the melting transition of crystalline ibuprofen and occurs without any accompanying mass change [12]. The second endothermic peak, at 215.76 °C, is associated with a pronounced mass loss in the TGA curve. This combined thermal and gravimetric response is characteristic of the decomposition of ibuprofen, where volatilization and oxidative breakdown result in significant mass reduction. Beyond this decomposition region, the thermogram shows no further major mass loss, confirming the near complete degradation of the drug [13]. Overall, the TGA-DSC analysis verifies the absence of surface bound moisture, confirms the melting point of ibuprofen, and clearly delineates the onset and progression of its thermal degradation.

Thermogravimetric analysis (**Figure 4c**) was used to determine the loading of ibuprofen within the sodalite framework by comparing the mass loss profiles of pure sodalite (**Figure 4a**), pure ibuprofen (**Figure 4b**), and the ibuprofen loaded sodalite composite (**Figure 4c**). Pure sodalite exhibited two characteristic weight loss events: an 11.62% loss between 33-300 °C corresponding to the desorption of physically adsorbed and structural water, and an 8.14% loss between 916-1200 °C associated with the gradual breakdown of the aluminosilicate framework. These losses represent the intrinsic thermal behavior of the host material.

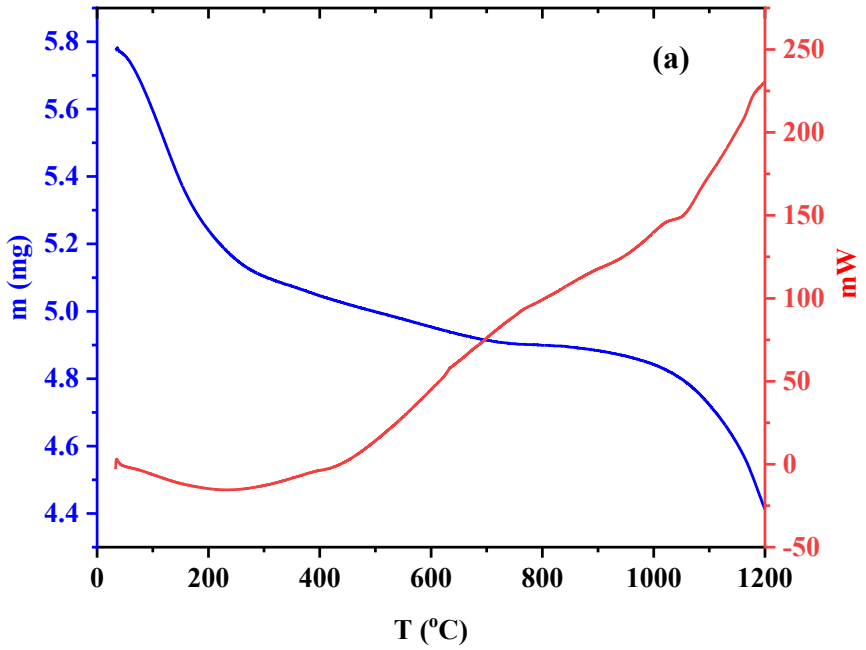
Pure ibuprofen, in contrast, undergoes nearly complete thermal decomposition (~100%) in a narrow range between 100-256 °C, which provides a distinct temperature window that can be used to quantify the organic content in the composite.

For the ibuprofen loaded sodalite sample, the total mass loss from 32-988 °C was 30.18%; however, this value includes overlapping contributions from sodalite dehydration, ibuprofen decomposition, and the onset of high temperature structural changes.

Because sodalite also loses water in the 33-300 °C region, which overlaps with the 100-256 °C decomposition interval of ibuprofen, total mass loss subtraction (composite minus sodalite) does not provide an accurate estimate of drug loading.

Instead, the ibuprofen content was calculated specifically from the 100-256 °C region, where pure ibuprofen decomposes completely and sodalite contributes only a small, predictable fraction of its dehydration loss. In this temperature window, the composite exhibited a mass loss of 7.46%, while pure sodalite contributes approximately 6.79% loss over the same interval. Subtracting the host contribution yields an ibuprofen related mass loss of 0.67%.

Since ibuprofen decomposes almost entirely within this range, the drug loading in the sodalite framework is therefore 0.67 wt%. This result indicates that only a small fraction of ibuprofen is retained within the sodalite pores under the synthesis conditions used, which is consistent with the limited pore volume and the hydrophilic nature of the sodalite framework.



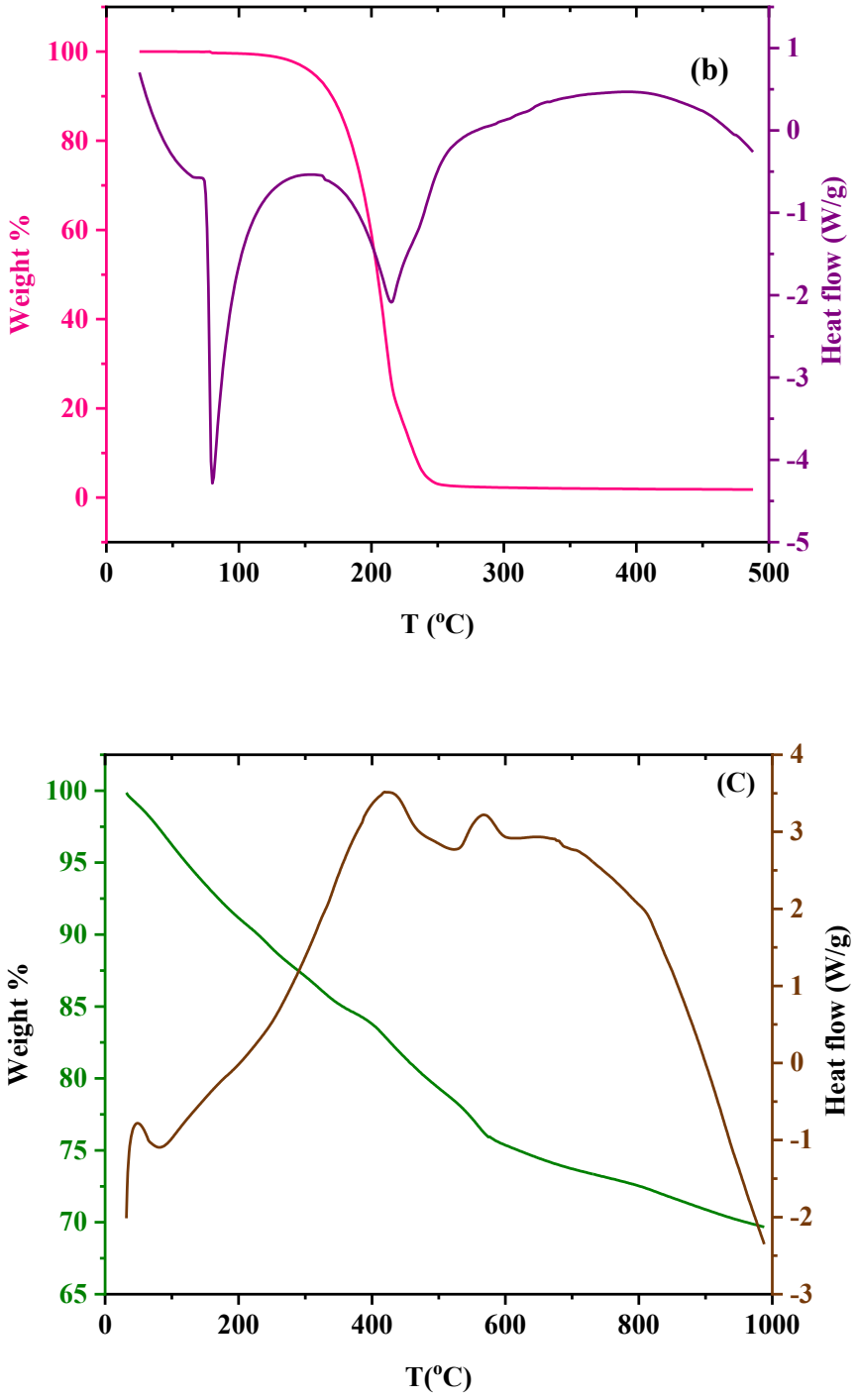


Figure 4: TGA/DSC analysis of (a): synthetic zeolite sodalite from bentonite, (b): ibuprofen and (c): ibuprofen loaded into sodalite.

1.1.5 The N_2 adsorption/desorption isotherm

Figure 5 illustrates the nitrogen adsorption-desorption behavior of the synthesized sodalite measured at -196.204 °C. Based on the IUPAC classification, the obtained isotherm corresponds to a Type IV profile, which is typically associated with mesostructured porous materials. The appearance of an H3-type hysteresis loop separating the adsorption and desorption curves indicates the existence of mesopores, commonly attributed to slit-like pore geometries or assemblies of plate-shaped particles [10]. Pronounced nitrogen uptake observed at intermediate relative pressures (P/P_0 between 0.4 and 0.9) further confirms the dominance of mesoporosity within the material. In contrast, the gradual adsorption recorded at lower relative pressures (P/P_0 below 0.3) suggests the presence of a microporous contribution. The steep rise in adsorption at high relative pressures ($P/P_0 > 0.9$) points to a hierarchical pore system, likely due to capillary condensation within large mesopores or small macropores. The observed hysteresis phenomenon reflects distinct adsorption and desorption pathways, indicative of complex pore-filling and pore-emptying mechanisms within the mesoporous network [11, 14]. The synthesized material exhibits a BET specific surface area of 205.85 m^2/g, indicative of a substantial surface typical of mesoporous materials with strong potential for adsorption and catalytic applications. The single-point surface area, determined at a relative pressure of $P/P_0 = 0.14$, yielded a comparable value of 202.47 m^2/g, demonstrating excellent agreement between the single-point and multipoint BET analyses. The pore volume data further clarify the material's textural characteristics. Using a single point adsorption method at $P/P_0 = 0.9897$, the total pore volume for pores up to approximately 190.5 nm was found to be 0.55207 cm^3/g. This substantial pore volume indicates a well-developed porous network with significant void space available for molecular accommodation, and it aligns well with the observed high surface area, confirming the material's hierarchical mesoporous-macroporous architecture. Because this measurement is made at a relative pressure close to saturation ($P/P_0 \approx 0.99$), nearly all accessible porosity including mesopores and small macropores is captured, giving a comprehensive estimate of the total void volume. Characterization of porous materials with mesopores (diameters between 2 and 50 nm) is most commonly performed by gas physisorption, using the same fundamental principles as the BET method under static volumetric conditions [15]. The average pore diameter analysis provides valuable insights into the dominant pore dimensions and geometric characteristics of the porous framework. The adsorption average pore diameter, calculated using the 4V/A relationship derived from BET data, was found to be 10.73 nm, while the desorption average pore diameter yielded a comparable value of 10.45 nm.

Both measurements fall well within the mesoporous range (2 - 50 nm), as defined by the IUPAC classification, confirming that the material's porosity is primarily governed by mesopores rather than micro or macropores. The 4V/A method is a widely accepted and reliable approach for estimating the mean mesopore diameter, particularly when the pore volume and surface area are determined from standard nitrogen adsorption-desorption analyses [16].

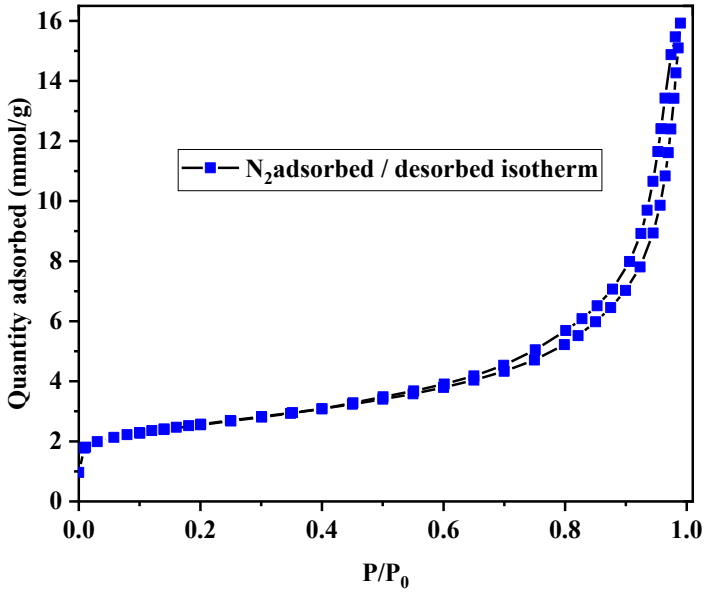


Figure 5: N_2 adsorbed-desorbed isotherm analysis of synthetic zeolite sodalite from bentonite.

The pore size distribution (PSD) of the sodalite synthesized from raw bentonite was derived from the desorption branch of its nitrogen adsorption-desorption isotherm (**Figure 6**) using the Barrett Joyner Halenda (BJH) method. The BJH method remains one of the most commonly employed approaches for characterizing mesoporous materials with pore diameters in the 2 to50 nm range [16-18]. The differential pore volume (dV/dD) as a function of pore diameter provides critical quantitative information about the statistical distribution and accessibility of pores within the material's structure. The obtained pore size distribution reveals an exponentially decreasing pattern extending over a wide range of approximately 2 to 160 nm, covering both the mesoporous domain (2 to 50 nm) and the lower macroporous region (>50 nm) as defined by the IUPAC classification. The curve reaches its highest differential pore volume of around 0.021 $cm^3\ g^{-1}\ nm^{-1}$ at the smallest detectable pore diameters (<5 nm).

This peak is followed by a rapid and continuous decline across the 2 to 30 nm interval, which then gradually transitions into a long, tapering tail toward larger pore sizes up to 160 nm, where the differential volumes become progressively smaller. Such a distribution pattern reflects a hierarchically organized porous structure, with most of the pore volume concentrated within the smaller mesoporous range, as indicated by the pronounced dV/dD values below 20 nm [18]. The hierarchical nature of the pore structure, characterized by the coexistence of small mesopores, larger mesopores, and macropores, offers significant functional advantages for practical applications [14, 16].

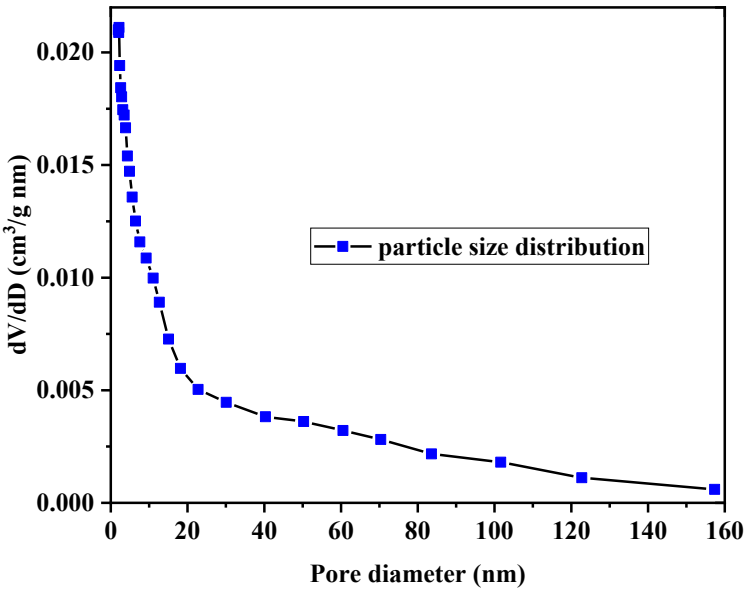


Figure 6: Particle size distribution of synthetic zeolite sodalite from bentonite.

1.1.6. Determination of the pH point zero charge

The point of zero charge (pH_{pzc}) corresponds to the pH value at which the net electrical charge on the surface of an adsorbent is neutral, resulting from an equal balance between positively and negatively charged surface sites. This parameter is fundamental for understanding the influence of surface charge on the adsorption behavior of contaminants in aqueous environments [19]. When the solution pH exceeds the pH_{pzc}, the adsorbent surface acquires a negative charge, thereby enhancing its affinity for positively charged species. In contrast, at solution pH values below the pH_{pzc}, the surface becomes positively charged, thereby favoring the uptake of negatively charged ions [20].

As illustrated in **Figure 7**, the pH_{pzc} of the synthesized material was experimentally determined to be 6.5, demonstrating that its surface charge is strongly dependent on the surrounding pH. At pH levels above 6.5, the surface exhibits a net negative charge, promoting cation adsorption, whereas at more acidic pH (pH < 6.5), the surface carries a positive charge, facilitating anion adsorption. The identified pH_{pzc} value indicates that the adsorbent exhibits amphoteric behavior, making it suitable for adsorption applications across slightly acidic to neutral pH ranges, depending on the ionic nature of the target pollutant.

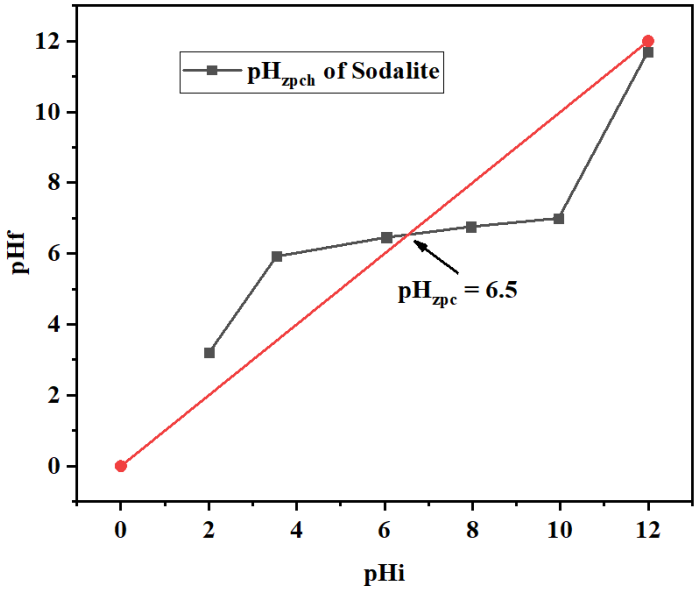


Figure 7: The pH point zero charge of sodalite (speed = 250rpm, v = 50ml, m = 50mg, t = 24h).

1.2 Experimental design result

The experimental design was employed to ascertain the individual and interaction impacts of the process factors. The outcome of the experimental design is presented in **Table 1**. The majority of the replies gathered from multiple trials were markedly outstanding, indicating that the input variables exerted a considerable influence on the response.

The maximum release of 0.715 was recorded at a pH of 1, duration of 20 minutes, and a stirring velocity of 75 revolutions per minute (rpm). The response varied from 0.401 to 0.715.

Table 1: RSM, ANFIS, and ANN models.

Runs	Process conditions			Release of ibuprofen (ABS)				
	pH	Time	Stirring rate	Exp	Model Predictions			
					RMS	Residual	ANN	AFNSI
1	1	20	75	0.715	0.7452	-0.0302	0.2122	0.2250
2	8	20	75	0.505	0.5578	0.0302	0.2120	0.2128
3	1	120	75	0.696	0.4858	0.0192	0.2855	0.2250
4	8	120	75	0.588	0.4613	0.0097	0.3035	0.3035
5	1	70	50	0.66	0.4748	-0.0098	0.7410	0.22508
6	8	70	50	0.441	0.4793	-0.0013	0.8658	0.8658
7	1	70	100	0.698	0.4703	0.0007	0.2255	0.2255
8	8	70	100	0.401	0.4703	-0.0013	0.2255	0.2255
9	4.5	20	50	0.452	0.6310	0.0290	0.8608	0.8610
10	4.5	120	50	0.465	0.4703	0.0007	0.4243	0.4243
11	4.5	20	100	0.471	0.4508	0.0012	0.3910	0.3899
12	4.5	120	100	0.478	0.7152	-0.0192	0.1118	0.1118
13	4.5	70	75	0.471	0.4703	0.0007	0.5053	0.5101
14	4.5	70	75	0.470	0.6775	0.0205	0.5053	0.5101
15	4.5	70	75	0.471	0.4703	-0.0003	0.5053	0.5101
16	4.5	70	75	0.470	0.4703	-0.0003	0.5053	0.5101
17	4.5	70	75	0.469	0.4300	-0.0290	0.5053	0.5101
18	4.5	70	75	0.471	0.4615	-0.0205	0.5053	0.5101

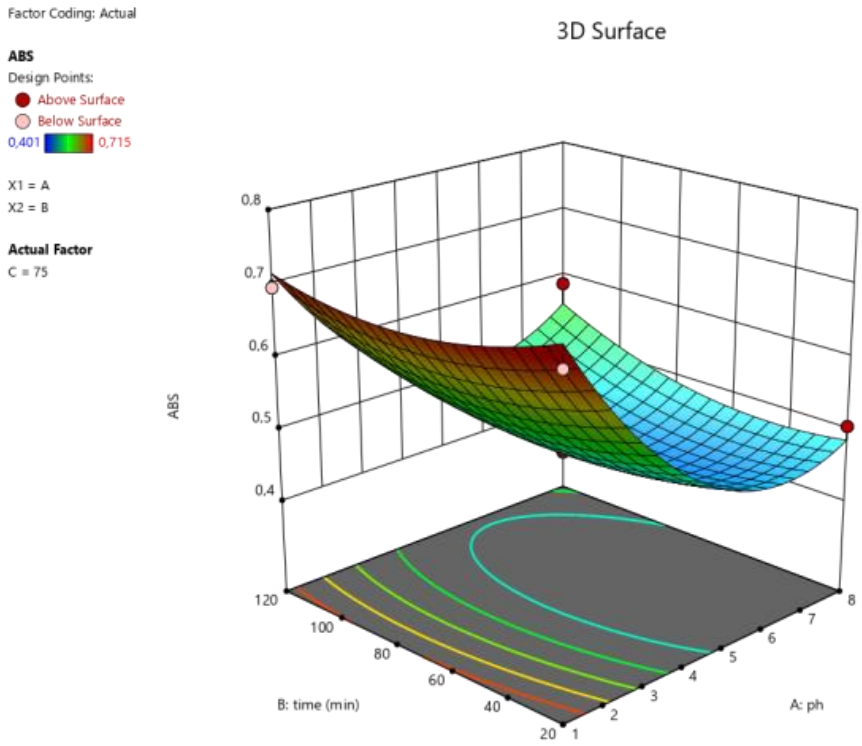
1.3 Interactive plots and sensitivity analysis

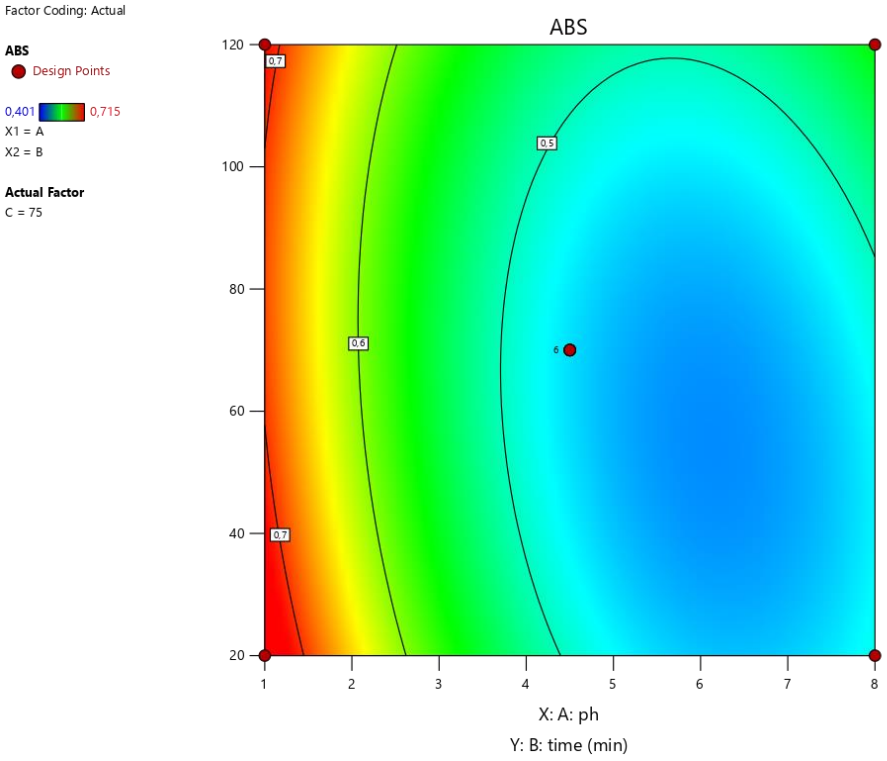
The combined influence of process variables on the response can be effectively analyzed through graphical visualization techniques, such as three-dimensional response surfaces and corresponding contour plots [21, 22]. These graphical representations are displayed in **Figure 8**. They were utilized to interpret the interactive and synergistic effects of the studied factors on ibuprofen release, which was monitored by measuring absorbance at 221 nm using UV spectroscopy. The response surface plots were generated by varying two independent parameters across their defined experimental ranges, while all remaining variables were fixed at their central (midpoint) levels.

The interaction influence of pH and time is illustrated in **Figure 8a** at a constant stirring rate of 75 rpm. It was noted that as pH and time increased concurrently, the release increase to a specific threshold before experiencing a minor decline. The release of drug diminished slightly after approximately 70.30 minutes, whereas it deteriorated beyond a pH of 4.75. The contour plot indicated that the optimal expected release was 0.715 at a contact period of 70 minutes and a pH of 4.5. The 3D graphic indicated a robust interaction link between time and pH.

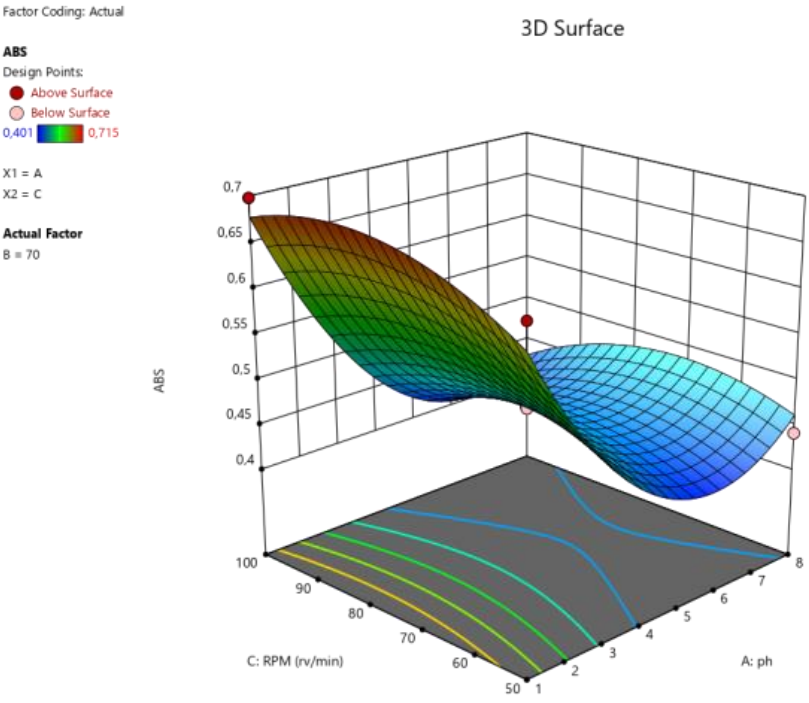
Figure 8b and **8c** illustrate the correlation between stirring rate and pH. The surface plot's shape revealed a minor reduction in the release following the initial decline. The optimal release of 0.401 was forecasted at a stirring velocity of 75 rpm and a pH of 4.5.

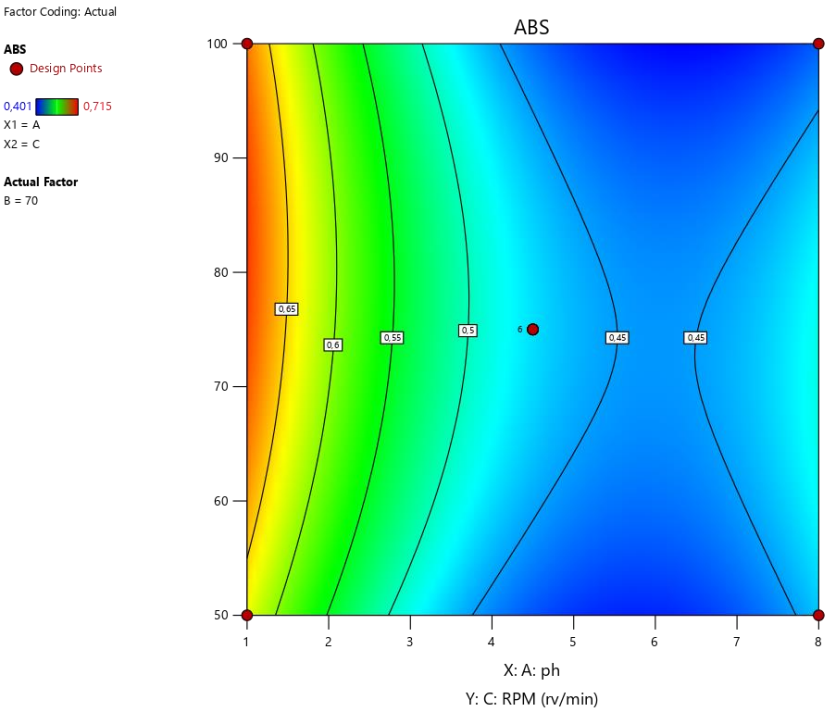
(a)



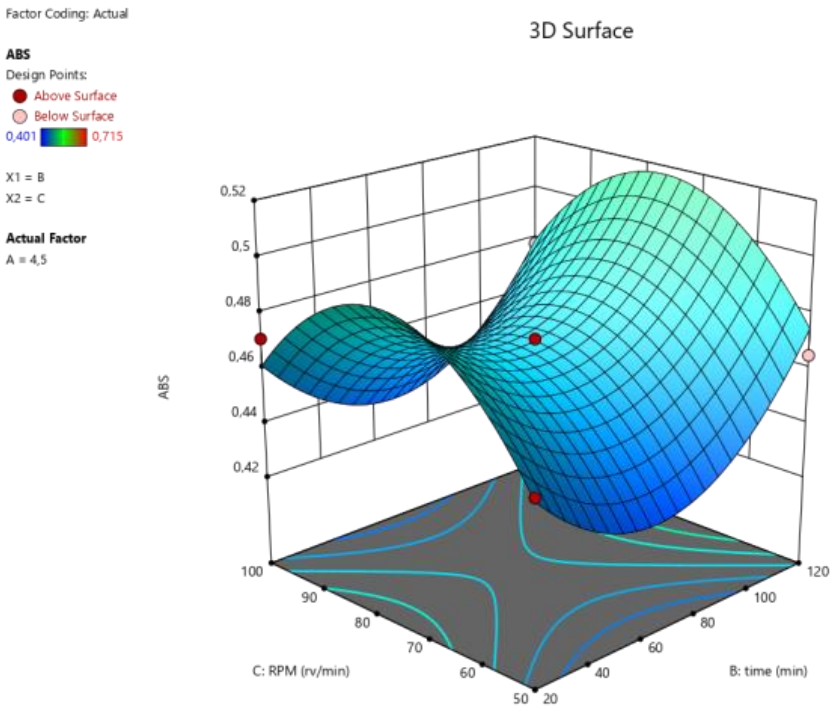

Factor Coding: Actual
ABS
Design Points
0,401
0,715
X1 = A
X2 = B
Actual Factor
C = 75
ABS
0,7
0,5
0,6
0,7
6
120
100
80
60
40
20
1
2
3
4
5
6
7
8
X: A: ph
Y: B: time (min)

(b)


Factor Coding: Actual
ABS
Design Points:
Above Surface
Below Surface
0,401
0,715
X1 = A
X2 = C
Actual Factor
B = 70
3D Surface
ABS
0,7
0,65
0,6
0,55
0,5
0,45
0,4
100
90
80
70
60
50
C: RPM (rv/min)
1
2
3
4
5
6
7
8
A: ph


Factor Coding: Actual
ABS
Design Points
0,401
0,715
X1 = A
X2 = C
Actual Factor
B = 70
ABS
100
90
80
70
60
50
1
2
3
4
5
6
7
8
0,65
0,6
0,55
0,5
0,45
0,45
X: A: ph
Y: C: RPM (rv/min)

(c)


Factor Coding: Actual
ABS
Design Points:
Above Surface
Below Surface
0,401
0,715
X1 = B
X2 = C
Actual Factor
A = 4,5
3D Surface
ABS
0,52
0,5
0,48
0,46
0,44
0,42
100
90
80
70
60
50
C: RPM (rv/min)
20
40
60
80
100
120
B: time (min)

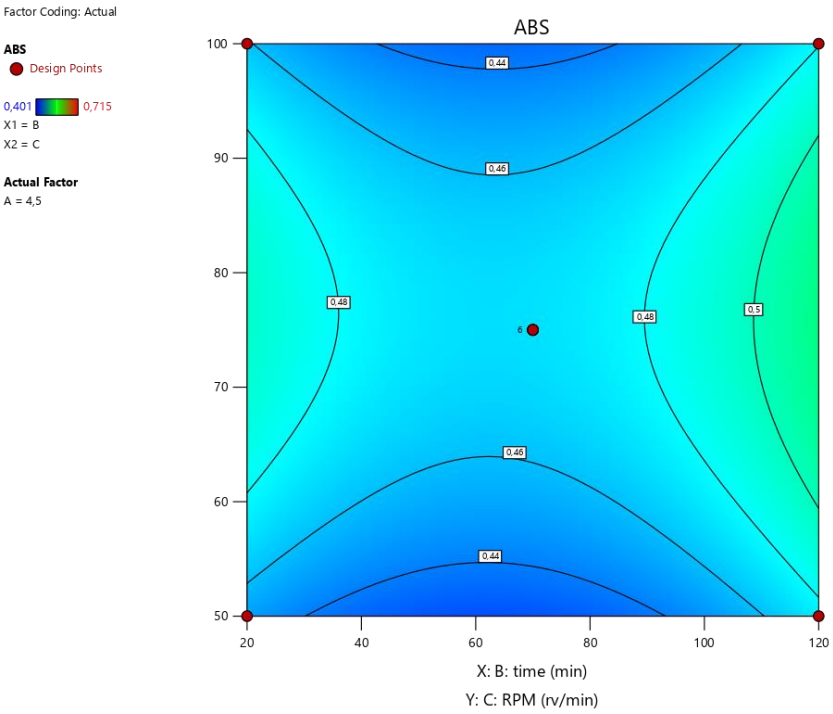


Figure 8: Surface (3D) and contour plots of the release of ibuprofen.

1.4 Box-Behnken Design (BBD) model analysis

Table 2 presents the regression coefficient (R^2), reflecting the model's goodness of fit. An R^2 value nearing 1 is advantageous. Thus, the regression coefficient value ($R^2 = 0.9693$) indicates that the model explains almost 95% of the total variance. The adjusted regression coefficient (adjusted $R^2 = 0.9347$) is high, signifying the model's considerable significance.

Table 2: Model Summary. Source: Authors.

Std. Dev.	0,0257		**R²**	0,9693
Mean	0,5218		**Adjusted R²**	0,9347
C.V. %	4,93		**Predicted R²**	0,5084
			Adeq Precision	16,4473

1.5 Response surface modeling

A central composite design (CCD) implemented through Design-Expert software was utilized within the response surface methodology (RSM) framework.

Model performance was assessed by comparing linear, quadratic, two-factor interaction (2FI), and cubic formulations to describe the relationship between the response variable and the selected process parameters. Model selection was guided by statistical criteria, namely a high coefficient of determination (R^2) combined with a low standard deviation, to ensure accurate representation of ibuprofen release behavior. The cubic model was excluded from consideration because the CCD structure does not provide a sufficient number of experimental runs to support full cubic regression analysis [23]. Among the evaluated models, the quadratic equation was identified as the most appropriate, exhibiting a standard deviation of 0.0257 and an R^2 value of 0.9693, as summarized in **Table 3**. In addition, the adjusted coefficient of determination (adjusted R^2) was calculated as 0.9347, closely matching the R^2 value and indicating a strong correlation between predicted and experimental responses, as well as statistical robustness of the model [24]. The adjusted R^2 accounts for the proportion of variability explained by the model while considering the number of independent variables included. Furthermore, the predicted R^2 value of 0.5084 differed from the adjusted R^2 by 0.4263, a difference within acceptable limits, confirming the adequacy of the model and the reliability of the experimental data [25].

Table 3: Statistical summary of the models investigated.

Source	Std.dev	R^2	Adjusted R^2	Predicted R^2	Press	
Linear	0,0775	0,5110	0,4062	0,0739	0,1594	
2FI	0,0853	0,5350	0,2813	-0,9904	0,3425	
Quadratic	**0,0257**	**0,9693**	**0,9347**	**0,5084**	**0,0846**	**Suggested**
Cubic	0,0008	1,0000	0,9999		*	Aliased

1.5.1 Analysis of variance

The analysis of variance (ANOVA) results are summarized in **Table 4** and were used to evaluate the statistical relevance of the quadratic regression model as well as the contribution of individual process variables. The statistical significance of each model term was determined based on corresponding p-values, applying a confidence interval of 95%. In this context, parameters associated with p-values greater than or equal to 0.05 were regarded as statistically insignificant, whereas those with lower p-values were identified as having a meaningful

influence on the response [26]. Model adequacy and the contribution of each independent variable were further examined using Fisher's F-test, which is defined as the ratio between the model mean square and the residual mean square. Elevated F-values for statistically significant terms indicate a stronger effect of those variables on the response behavior [27]. The robustness of the quadratic model was confirmed by an overall model p-value below 0.0001 and an F-statistic of 28.03, demonstrating strong statistical significance. According to the ANOVA findings, the linear effects of pH (A), contact time (B), and stirring rate (C) were significant, along with their pairwise interaction terms (AB, AC, and BC) and the quadratic components (A^2, B^2, and C^2). As only a limited number of non-significant terms were observed, model simplification was not required. Among the studied variables, pH exhibited the most dominant influence on ibuprofen release, while dosage and the interaction between pH and time showed the strongest effects among the quadratic and interaction terms, respectively. The resulting quadratic regression equation describing the release process as a function of the investigated parameters is provided in **Equation (11).**

$$\textbf{Release} = +0.4703 - 0.1042\,A + 0.0105\,B + 0.0037\,C + 0.0255AB - 0.0195\,AC - 0.0015BC + 0.1196A^2 + 0.0361B^2 - 0.0399C^2 \quad \textbf{Equation (11)}$$

The developed regression equation can be applied to estimate the response under specific combinations of process variables. In addition, it enables evaluation of the relative influence of each factor through comparison of the corresponding regression coefficients. In this context, model terms associated with positive coefficients indicate a cooperative (synergistic) contribution to the response, whereas negative coefficients reflect an opposing (antagonistic) influence. Based on the ANOVA results, the interaction terms AB, AC, and BC were identified as statistically non-significant. Consequently, these terms were removed from the regression model, and the refined equation describing the system behavior is presented in **Equation (12)**.

$$\textbf{Release} = +0.4703 - 0.1042\,A + 0.0105\,B + 0.0037\,C + 0.0255AB - 0.0195\,AC - 0.0015BC + 0.1196A^2 + 0.0361B^2 - 0.0399C^2 \quad \textbf{Equation (12)}$$

Table 4: ANOVA and model coefficients for the release process.

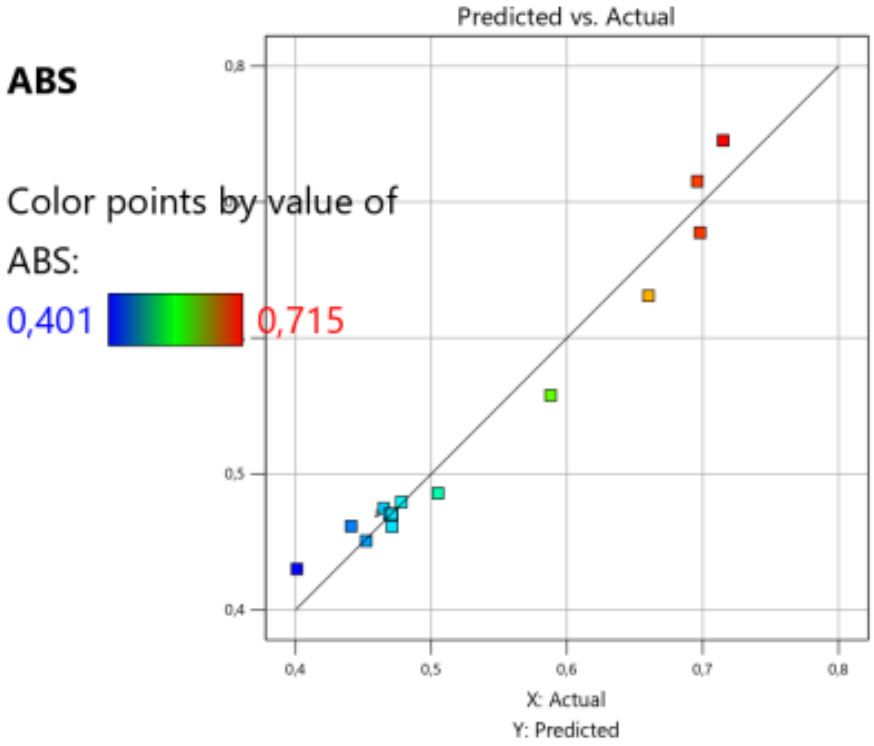
Source	Sum of squares	df	Mean square	F-value	P-value	
Model	0,1668	9	0,0185	28,03	< 0.0001	Significant
A-pH	0,0869	1	0,0869	131,48	< 0.0001	
B-time	0,0009	1	0,0009	1,33	0,2815	
C-RPM	0,0001	1	0,0001	0,1701	0,6908	
AB	0,0026	1	0,0026	3,93	0,0826	
AC	0,0015	1	0,0015	2,30	0,1678	
BC	9,000E-06	1	9,000E-06	0,0136	0,9100	
A^2	0,0624	1	0,0624	94,36	< 0.0001	
B^2	0,0057	1	0,0057	8,59	0,0190	
C^2	0,0070	1	0,0070	10,51	0,0118	
Residual	0,0053	8	0,0007			
Lack of Fit	0,0053	3	0,0018	2643,50	< 0.0001	Significant
Pure Error	3,333E-06	5	6,667E-07			
Cor Total	0,1721	17				

1.5.2 Diagnostic plots

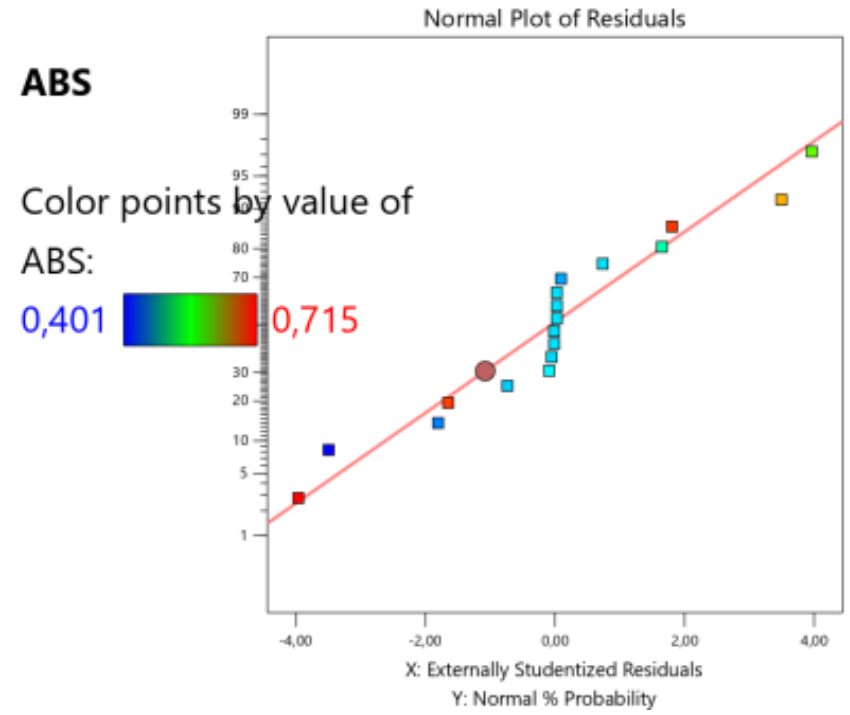
In addition to numerical correlation indicators, graphical diagnostic tools were employed to examine the behavior of residuals defined as the difference between experimentally observed and model predicted values as presented in **Figure 9**. Such analyses are critical for assessing the adequacy and reliability of the proposed model. **Figure 9a** compares experimental measurements with corresponding predicted values, whereas **Figure 9b** displays the distribution of residuals. The close clustering of data points along the 45° reference line in **Figure 9a** demonstrates a strong agreement between observed and predicted responses [22]. Furthermore, the residual distribution reveals that most values fall within the range of -1 to +1, indicating minimal deviation between experimental data and model estimates. These observations confirm that residual magnitudes are sufficiently small, eliminating the need for response transformation and validating the suitability of the quadratic regression model for describing the release behavior (ABS). The perturbation analysis, shown in **Figure 9c**, illustrates the sensitivity of the response to variations in each factor relative to a central reference point expressed in coded units.

The baseline response corresponded to a mean release value of 0.480. Among the studied parameters, pH (A) exhibited the most pronounced influence, with the response varying from 0.480 to 0.690 as the coded level shifted from -1 to +1. In contrast, stirring rate (C) produced only minor changes, with response values fluctuating between 0.430 and 0.440 over the same coded range, indicating a comparatively weaker effect on the release process.

(a)



(b)



(c)

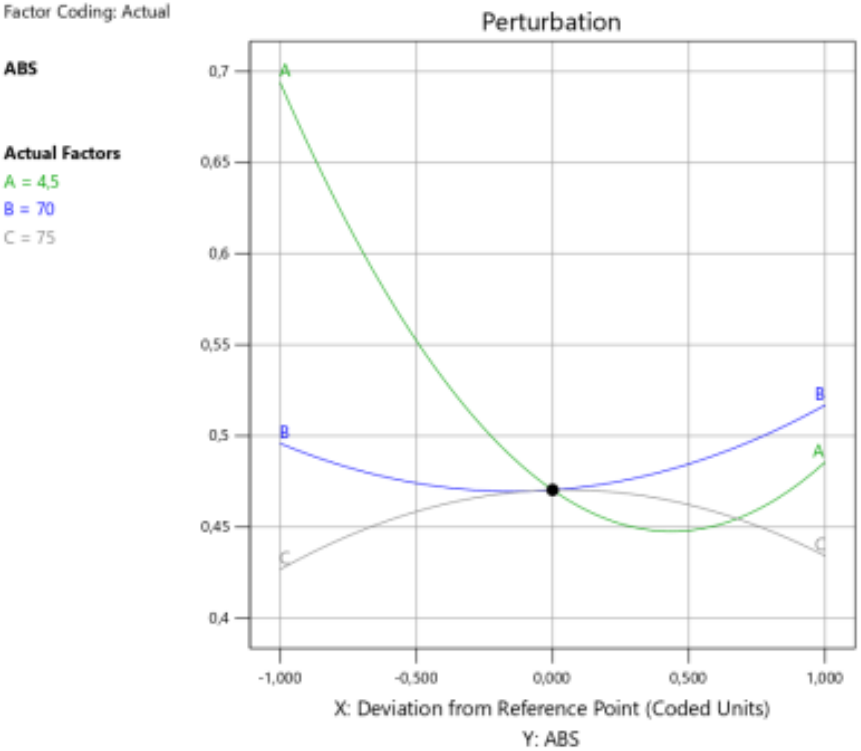


Figure 9: RSM diagnostic plots for (a) Predicted vs actual, (b) Normal plot of residual, and (c) Perturbation.

As illustrated in **Figure 10**, the residual analysis maintains a predominantly random distribution, with residual values fluctuating irregularly before stabilizing around a zero baseline and showing no evidence of statistically significant outliers. This pattern indicates the absence of systematic error and supports the adequacy of the proposed model. Additionally, the perturbation plot highlights the relationship between the independent variables and the response, clearly demonstrating how variations in the studied factors exert a pronounced influence on the system's behavior.

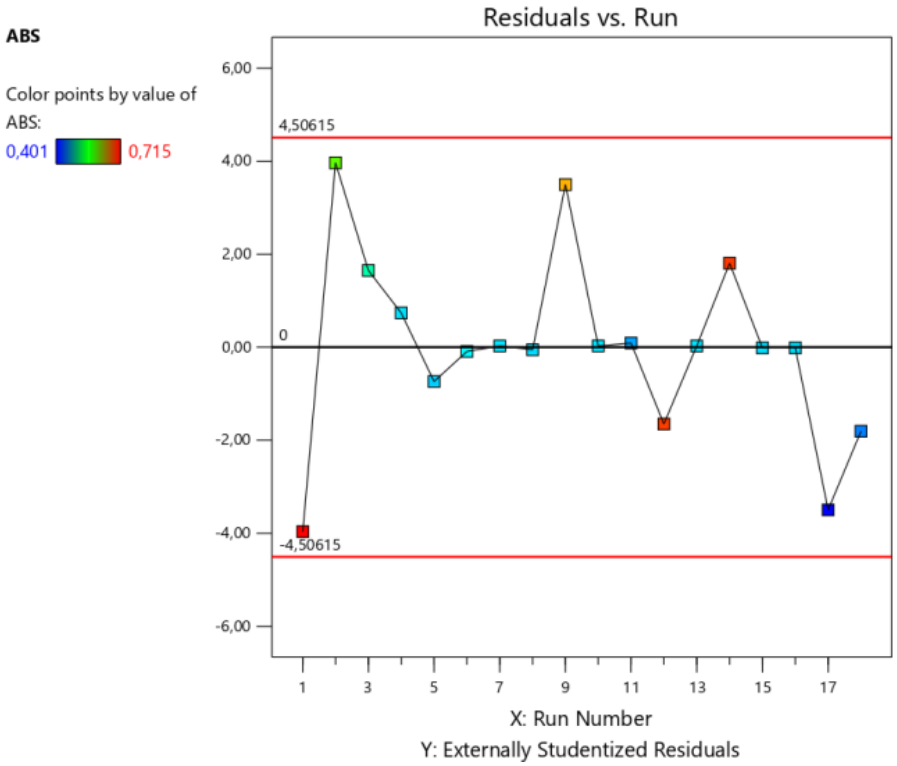


Figure 10: Plot of the experimental run order against the externally studentized residuals. Source: Authors.

1.6 Artificial neural network modeling

The artificial neural network (ANN) model was developed using the Levenberg-Marquardt (LM) backpropagation algorithm, which is widely applied in multi-layer perceptron (MLP) architectures to minimize prediction error.

To reduce the risk of overfitting and avoid excessive model complexity, the available data were systematically divided into training, validation, and testing subsets [28]. The neural network was trained using triplicate experimental runs corresponding to ibuprofen release measurements. Optimization of the network structure was achieved by identifying the number of hidden neurons that produced the lowest mean square error (MSE), which was determined to be ten using the Trainlm algorithm. Consequently, the finalized ANN architecture adopted a 3-10-1 configuration, consisting of three input neurons representing pH, contact time, and stirring rate, a single hidden layer containing ten neurons, and one output neuron corresponding to the ibuprofen release response. This configuration was selected to ensure optimal learning efficiency and predictive accuracy. In total, one hundred twenty-five (125) experimental data sets were used during the training phase to enable the network to generalize and predict outcomes for unseen input conditions [29]. Model performance was evaluated using the mean square error (MSE) and the coefficient of determination (R^2), which together quantify both prediction accuracy and the strength of the relationship between input variables and the output response [30]. The resulting feed forward ANN structure effectively captured the multidimensional relationships governing the release process. The stability and robustness of the training procedure were assessed through the validation performance curve presented in **Figure 11**, which illustrates changes in MSE as a function of training epochs. The optimal network performance was achieved at approximately the 1000^{th} epoch, where the validation MSE reached a minimum value of 0.00022332. The absence of a premature increase in the validation or test error curves indicates that the model was successfully trained without overfitting. Had the test error increased significantly prior to the validation error, it would have suggested potential overtraining; however, such behavior was not observed in this case.

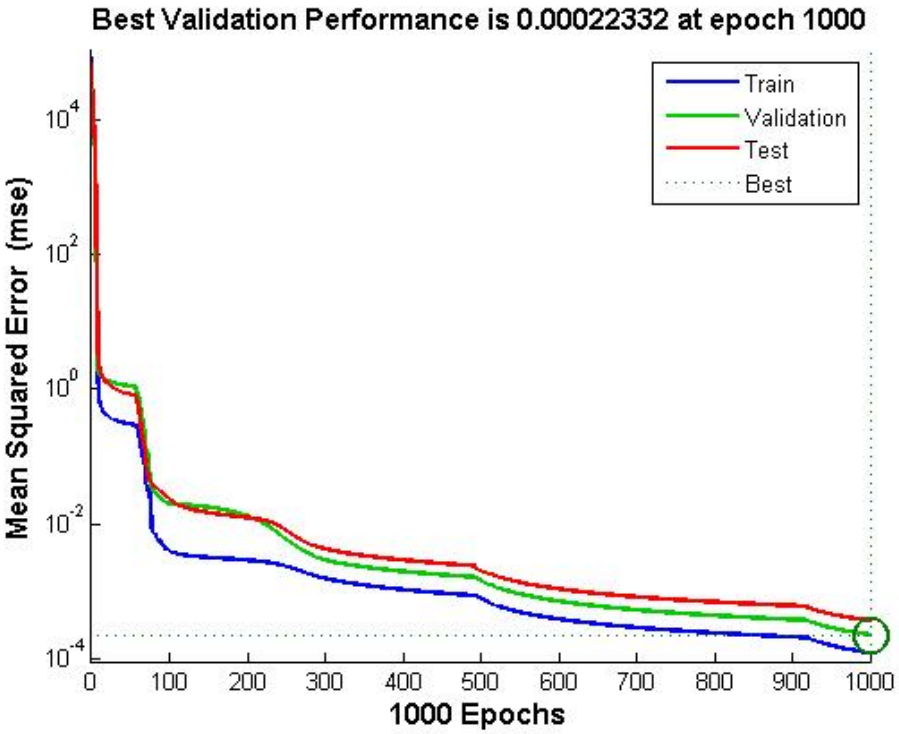


Figure 11: ANN performance validation plot.

Figure 12 presents the regression analysis of the artificial neural network, illustrating the relationship between the experimental target values and the corresponding normalized outputs predicted by the model for the training, validation, testing, and combined datasets. Prior to model evaluation, all data were subjected to normalization to enhance training efficiency and prediction accuracy. The resulting correlation coefficients were equal to 1.0 for each dataset category training, testing, validation, and overall indicating an excellent agreement between predicted and experimental values. In addition, the training phase achieved a mean square error (MSE) of 0.000175, reflecting high predictive precision. Among the evaluated configurations, the ANN architecture defined by a 3-10-1 topology comprising three input neurons, ten neurons within a single hidden layer, and one output neuron exhibited the highest model fitness. The optimal connection weights and bias parameters associated with each network layer were derived from the experimental dataset and are summarized in **Table 5**, providing a complete numerical description of the trained ANN model.

Table 5: Values of connection weights and biases for the completed neural network model. Source: Authors.

W_1	Node 1	Node 2	Node 3	Node 4	Node 5	Node 6	Node 7	Node 8	Node 9	Node 10	Bais (B_2)
Input 1	-0.0130	0.3327	-2.1000	-0.0050	0.0334	-0.9104	-0.0894	0.0372	0.9894	2.7652	
Input 2	-3.1667	2.2445	2.2429	0.0040	1.4111	-1.1554	-0.0534	0.2970	1.5424	1.8168	
Input 3	-0.0040	0.0901	0.6703	0.2404	0.0080	0.7462	0.0848	0.0099	0.3149	-2.2581	
Output Layer (W_2)	0.0887	0.0209	-0.0001	-2.9118	0.3477	-0.0003	1.1754	1.9143	0.0023	3.4517e-05	
Bais (B_1)	-2.1812	-2.7294	1.6635	-0.6679	-1.3465	-0.2382	-0.6207	0.0423	2.6413	4.2837	
											-0.8996

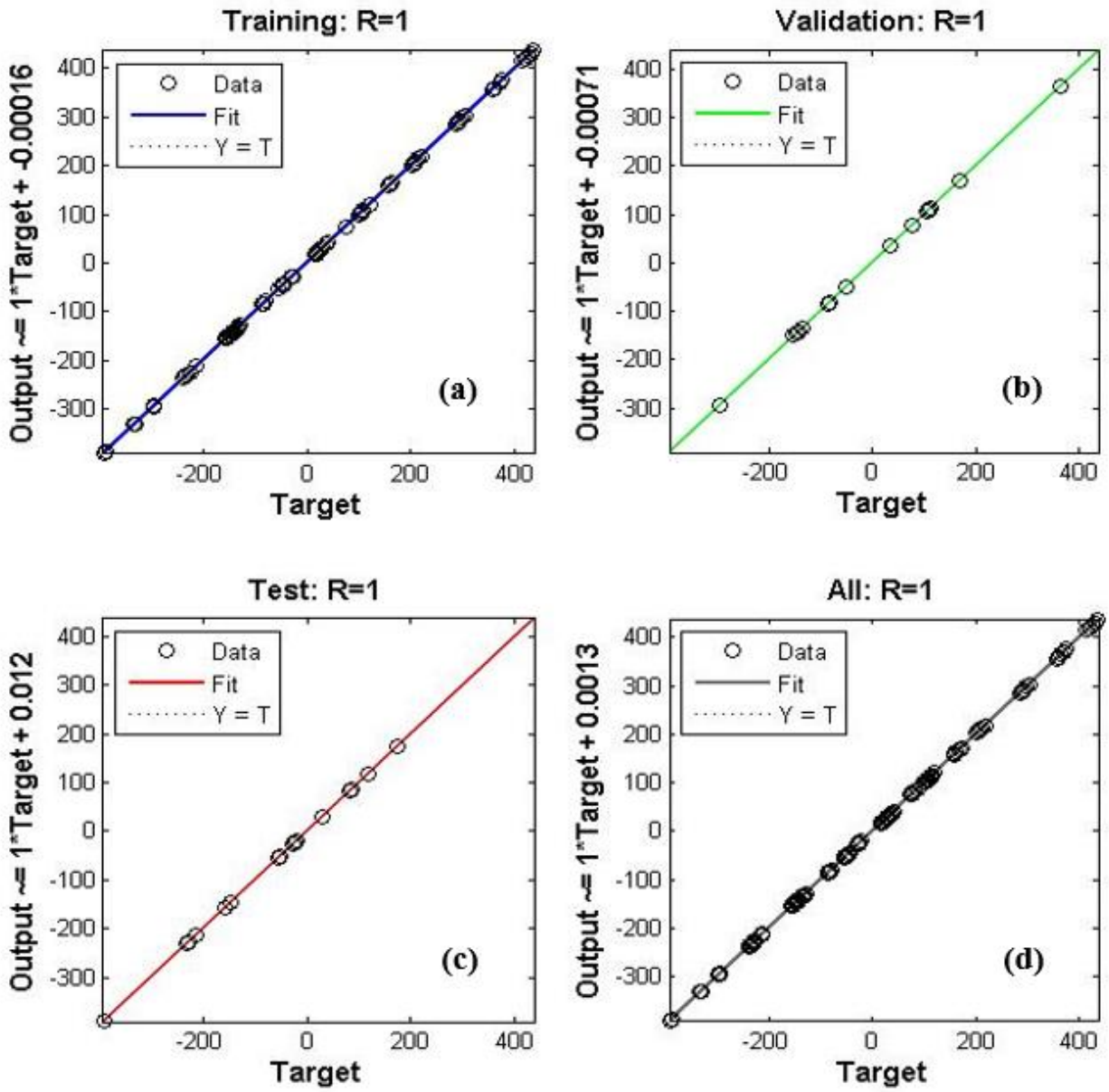


Figure 12: ANN correlation plots for (a) training, (b) validation, (c) testing and (d) overall network processes.

Correlation coefficients close to unity were obtained across all datasets, confirming the strong predictive capability of the model for each data category. In addition, the regression lines closely followed the ideal 45° reference line, particularly for the training and overall datasets, indicating a high level of agreement between experimental targets and ANN predicted outputs.

These results demonstrate that the ANN response accurately represents the ibuprofen release behavior. The complete set of ANN predicted release values corresponding to each experimental condition is provided in the supplementary material, while a direct comparison with the experimental results is presented in **Table 1**. The high level of correlation and predictive accuracy achieved by the ANN model can be attributed to its well-established ability to capture and approximate nonlinear system behavior [31].

The training performance of the ANN is depicted in **Figure 13**. As shown, the gradient value used to iteratively adjust network parameters during optimization reached 0.76032. The adaptive learning parameter (μ), which controls weight updates throughout the training process, was maintained at 1×10^{-3}, while the validation checks at the 1000^{th} epoch was equal to zero. Collectively, these indicators confirm the stability and effectiveness of the ANN training process, as well as the strong correspondence between predicted and experimental values [32].

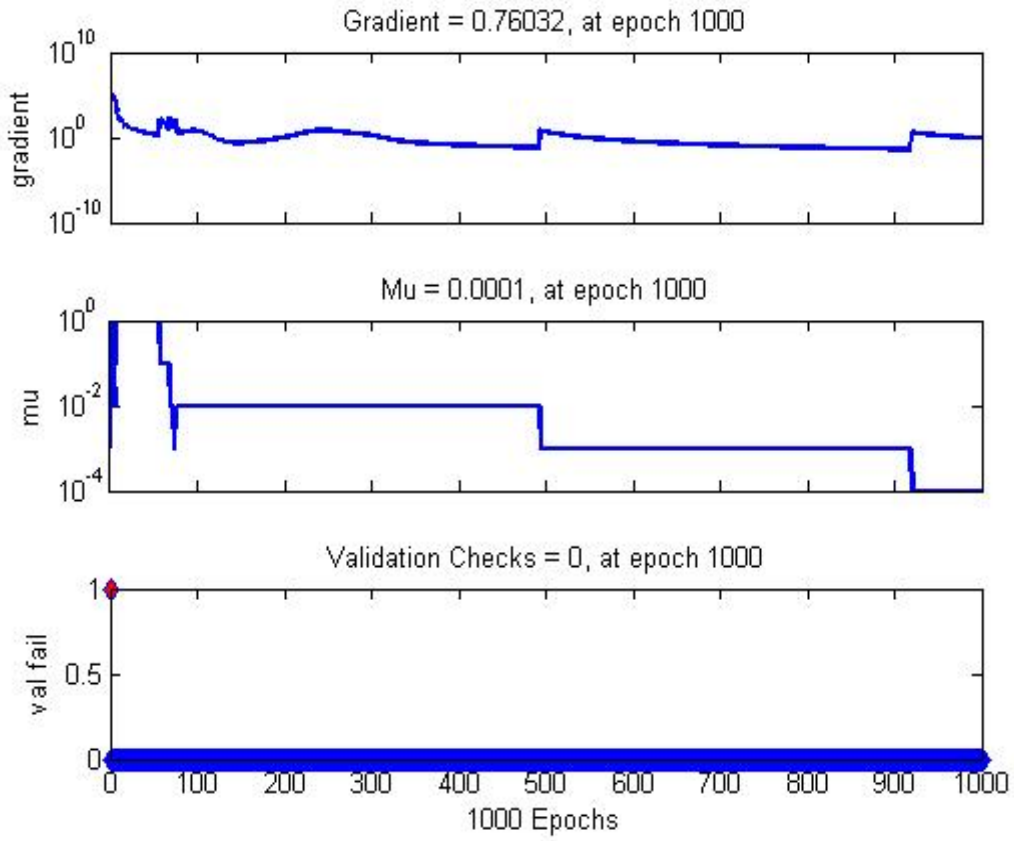
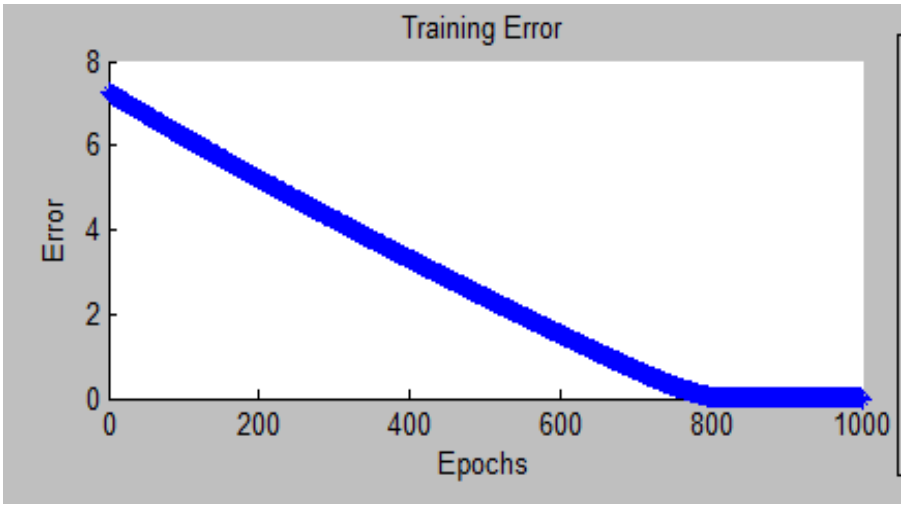


Figure 13: Training State.

1.7 Adaptive neuro-fuzzy inference system modeling

In addition to the ANN and RSM frameworks, an adaptive neuro-fuzzy inference system (ANFIS) was implemented to further investigate the relationship between predicted outcomes and experimental observations. The ANFIS architecture was developed using a hybrid learning strategy that combines the least squares estimation technique with gradient-based optimization. To improve computational performance and model accuracy, data normalization was applied prior to fuzzy model training. The input dataset implemented in the MATLAB environment consisted of a 125 × 3 matrix, corresponding to 125 experimental instances of three independent variables pH, contact time (min), and stirring rate (RPM) along with 125 associated values of the dependent variable representing ibuprofen release. **Figure 14** presents the structure of the Sugeno type fuzzy inference system generated through the grid partitioning approach. In this configuration, each input variable was assigned three membership functions to establish the fuzzy rule base. The ANFIS model achieved a correlation coefficient of 0.959934, demonstrating its strong capability to accurately predict release behavior. One of the key strengths of ANFIS lies in its ability to reduce prediction error by integrating fuzzy logic with adaptive learning mechanisms. Model training was carried out using triangular membership functions within the hybrid FIS training algorithm [33], with the learning process executed over 1000 epochs. At the completion of training, the model exhibited an error value of 0.040066, confirming its effectiveness in representing the release mechanism. The relatively low mean square error further indicates that the model did not suffer from overfitting and retained strong generalization ability. Detailed ANFIS predicted release values for all experimental conditions are provided in the supplementary material, while a comparative evaluation against other modeling approaches is summarized in **Table 1**.

(a)



(b)



Figure 14: (a) ANFIS Sugeno training error and (b) ANFIS distribution of predicted and experimental data of the release process.

1.7.1Statistical error analysis

To further evaluate the predictive robustness of the developed models, seven statistical error metrics were applied to the predicted outputs, with the corresponding results summarized in **Table 6**. The coefficient of determination (R^2) and root mean square error (RMSE) were specifically examined for each modeling approach.

Lower values of these error indicators are associated with stronger predictive performance, and the obtained results revealed generally low error magnitudes for all models under consideration. In addition, both R^2 and adjusted R^2 values were analyzed to assess model reliability while accounting for model complexity[34].

Comparative statistical analysis indicated that the response surface methodology (RSM) exhibited the lowest predictive accuracy among the evaluated approaches. While the ANN and ANFIS models both demonstrated superior predictive capability relative to RSM, slight differences were observed between them depending on the selected performance criteria. Overall, the results confirm that artificial intelligence-based models, particularly ANN and ANFIS, provide enhanced accuracy for predicting the release behavior, with performance advantages that vary marginally between the two techniques [33,35-36].

Table 6: Statistical error indices of the RMS, ANN, and ANFIS.

Parameters	Results		
	RMS	ANN	ANFIS
R^2	0.9693	0.9999	0.959934
RMSE	0.0307	0.0001	0.04006

1.8 Comparative analysis of the models

The ability of the RSM, ANN, and ANFIS approaches to capture the nonlinear behavior associated with ibuprofen release was evaluated using both graphical representations and statistical analyses. **Table 1** presents a comparison of the experimentally measured values with the corresponding predicted outputs and residuals generated by each model. Overall, all three modeling techniques demonstrated satisfactory performance, providing accurate estimations of release behavior. The residual values, which represent the deviation between observed and predicted data, were generally small, indicating strong agreement between experimental results and model predictions across the dataset. Among the evaluated approaches, the ANN model exhibited a slight advantage in predictive performance, as evidenced by the presence of numerous negligible residual values. Comparative results summarized in **Table 6** further illustrate the relationship between experimental measurements and predictions obtained from the RSM, ANN, and ANFIS models.

Graphical comparisons revealed a strong correlation between measured and predicted values for all three methods, with no significant discrepancies observed for most factorial and axial experimental points. To further distinguish model performance, a series of statistical error metrics was applied, enabling a more rigorous comparison of the predictive accuracy of the three modeling strategies.

1.9 Optimization using genetic algorithm

A genetic algorithm (GA) was applied as an optimization tool to identify operating conditions that maximize the release efficiency while minimizing experimental effort. For this purpose, the ANFIS framework was selected as the most reliable predictive model to guide the optimization process. The decision variables considered in the GA included solution pH (ranging from 1 to 8), contact time (20-120 minutes), and stirring speed (50-100 rpm). The optimization procedure identified optimal conditions at a pH of 4.234, a processing time of 53.452 minutes, and an agitation rate of 63.581 rpm. Under these conditions, the GA converged consistently to an optimal response value of 0.469. To confirm the reliability of the GA-derived solution, validation experiments were performed in triplicate using the optimized parameter set. The experimentally obtained release value matched the predicted outcome, yielding a release of 0.469, thereby demonstrating strong agreement between the GA prediction and experimental verification [37].

2. Conclusion

In this study, sodalite zeolite was successfully synthesized using raw bentonite (Maghnite) as a low-cost and sustainable aluminosilicate precursor and subsequently evaluated as a functional carrier for the controlled release of ibuprofen in simulated physiological media. The successful synthesis and application of this material highlight its potential as an alternative drug delivery platform derived from natural resources.

To minimize experimental effort while identifying the most influential operational variables governing drug release, a structured experimental strategy was implemented using Design-Expert software. A total of 18 experimental runs were performed to investigate the combined effects of pH, release duration, and stirring speed. The experimental findings revealed that maximum ibuprofen release was achieved under highly acidic conditions (pH 1), with a short contact time of 20 minutes and a stirring speed of 75 rpm, emphasizing the dominant role of pH in controlling release behavior.

The predictive reliability of the system was further enhanced through the integration of statistical and artificial intelligence-based modeling tools implemented in MATLAB. Within the Box–Behnken Design framework, a high coefficient of determination (R^2 = 0.9693) confirmed that approximately 95% of the variability in ibuprofen release could be explained by the developed model. Complementary response surface methodology (RSM) analysis using a Central Composite Design (CCD) demonstrated that a quadratic regression model provided the most accurate description of the release process, as evidenced by a low standard deviation (0.0257) and an identical R^2 value of 0.9693. Analysis of variance (ANOVA) further validated the robustness of this model, yielding a highly significant p-value (< 0.0001) and an F-value of 28.03, along with a mean square of 0.0185 and a sum of squares of 0.1668.

Advanced artificial intelligence models were subsequently employed to improve prediction accuracy. The artificial neural network (ANN), trained using the Levenberg–Marquardt backpropagation algorithm with a 3-10-1 multilayer perceptron structure, demonstrated excellent learning performance. Using 125 experimental data points, the ANN achieved a minimum validation mean square error of 0.00022332 at the 1000^{th} training epoch, indicating strong generalization ability and absence of overfitting.

In parallel, the adaptive neuro-fuzzy inference system (ANFIS) model, developed using the same dataset, achieved a correlation coefficient of 0.959934 with a final training error of 0.040066 after 1000 epochs, confirming its effectiveness in capturing nonlinear system behavior.

Comparative graphical and statistical evaluations of experimental, predicted, and residual values demonstrated that RSM, ANN, and ANFIS models were all capable of accurately representing the ibuprofen release process, with ANN exhibiting the highest predictive precision. Building upon this predictive framework, a genetic algorithm (GA) was applied to determine optimal release conditions. The optimization process converged to an optimal fitness value of 0.469 at pH 4.234, a release time of 53.452 minutes, and a stirring speed of 63.581 rpm. Experimental validation conducted under these optimized conditions confirmed close agreement with the GA prediction.

Overall, the integration of sustainable material synthesis, experimental design, statistical modeling, artificial intelligence, and evolutionary optimization provides a powerful and efficient framework for developing controlled drug delivery systems. The results demonstrate that sodalite zeolite derived from bentonite is a promising carrier for ibuprofen release and that AI-assisted optimization strategies can significantly enhance prediction accuracy and process efficiency. This approach offers a valuable foundation for future studies aimed at extending zeolite-based delivery systems to other pharmaceutical compounds and therapeutic applications.

References

[1] K. Atkovska and al., "Adsorption of Fe (II) and Zn (II) ions from landfill leachate by natural bentonite," Journal of Chemical Technology and Metallurgy, pp. 215–222, 2016.

[2] Y. Liu and al., "Mechanical activation of kaolinite for sodalite synthesis under mild conditions," Appl. Clay Sci., vol. 271, no. February, p. 107796, 2025 doi: 10.1016/j.clay.2025.107796.

[3] A. El-kordy and al., "Exploring nickel-modified sodalite zeolite for efficient methyl orange removal from aqueous solutions : A comprehensive mechanistic and equilibrium analysis," Inorg. Chem. Commun., vol. 183, no. P1, p. 115686, 2026. doi: 10.1016/j.inoche.2025.115686.

[4] A. Kordy and al, "Preparation of sodalite and faujasite clay composite membranes and their utilization in the decontamination of dye effluents," Membranes, pp. 1–18, 2022. doi: 10.3390/ membranes12010012.

[5] C. Günther and al., "Synthesis and characterization of a sulfur containing hydroxy sodalite without sulfur radicals," Microporous Mesoporous Mater., vol. 214, pp. 1–7, 2015. doi: 10.1016/j.micromeso.2015.04.024.

[6] M. Osacký and al., "Low-cost zeolite-based sorbents prepared from industrial perlite by-product material for Zn^{2+} and Ni^{2+} removal from aqueous solutions: synthesis, properties and sorption efficiency," Heliyon, vol. 8, no. November, 2022. doi: 10.1016/j.heliyon.2022.e12029.

[7] M. M. Kumar and H. Jena, "Direct single-step synthesis of phase pure zeolite Na – P1 , hydroxy sodalite and analcime from coal fly ash and assessment of their Cs^{+} and Sr^{2+} removal efficiencies," Microporous Mesoporous Mater., vol. 333, no. November 2021, p. 111738, 2022. doi: 10.1016/j.micromeso.2022.111738.

[8] K. Pertiwi and al, "Enhanced antibacterial efficacy of Ag (I), Cu (II), and Zn (II) modified sodalite zeolite against Escherichia coli and Staphylococcus aureus," Journal of Scientific and Applied Chemistry, vol. 27, no. 10, pp. 477–484, 2024. doi: 10.14710/jksa.27.10.477-484.

[9] M. J. P. Araneta and al., “Enhanced Removal of Acetylsalicylic Acid Using Surfactant-Modified Natural Zeolites,” Trends Sci, vol. 22, no. 2, pp. 1–18, 2025. doi: 10.48048/tis.2025.8908.

[10] K. Imene and al., “Thermal treatment of Cu-doped hydrotalcite-like adsorbents for improved removal of methyl orange from water,” Sep. Purif. Technol., vol. 365, no. February, p. 132656, 2025. doi: 10.1016/j.seppur.2025.132656.

[11] R. Das and al, “Synthesis of single crystal zeolite L rods with high aspect ratio using rice husk ash as silica source,” Indian Journal of Chemistry, vol. 53A no. July, 2014.

[12] F. Xu and al, “Thermodynamic study of ibuprofen by adiabatic calorimetry and thermal analysis,” Thermochimica Acta, vol. 412, pp. 33–37, 2004. doi: 10.1016/j.tca.2003.08.021.

[13] B. Tita and al, “Kinetic study of decomposition of ibuprofen under isothermal conditions,” Rev. Chim. (Bucharest), vol. 62, no. February, 2011.

[14] C. Schlumberger and M. Thommes, “Characterization of hierarchically ordered porous materials by physisorption and mercury porosimetry — a tutorial review,” Adv. Mater. Interfaces, vol. 2002181, 2021. doi: 10.1002/admi.202002181.

[15] D. Liu and al, “Pore structure characterization and its significance for gas adsorption in coals : A comprehensive review,” Unconv. Resour., vol. 2, no. September, pp. 139–157, 2022. doi: 10.1016/j.uncres.2022.10.002.

[16] K. A. Tarach and al, “Tailored approach for hierarchization of all-silica zeolites,” Materials & Design, vol. 257, no. April, 2025. doi: 10.1016/j.matdes.2025.114435.

[17] J. Amaya and al, “Bifunctional catalysts supported on modi fi ed vermiculite for the hydroconversion of decane . E ff ect of the metal phase (Mo or W) and promoters (Ni or Co),” Catalysis Today, vol. 356, no. November 2019, pp. 271–283, 2020. doi: 10.1016/j.cattod.2019.11.023.

[18] K. S. W. SING and al, “Reporting physisorption data for gas/solid systems with special reference to the determination of surface area and porosity,” vol. 57, no. 4, pp. 603–619, 1985.

[19] C. Eduardo and al., "Basic-dye adsorption in albedo residue : Effect of pH , contact time , temperature , dye concentration , biomass dosage , rotation and ionic strength," J. King Saud Univ. - Eng. Sci., vol. 32, no. 6, pp. 351–359, 2020.
doi: 10.1016/j.jksues.2019.04.006.

[20] S. N. Guilhen and al, "Role of point of zero charge in the adsorption of cationic textile dye on standard biochars from aqueous solutions : Selection criteria and performance assessment", Recent Progress in Materials, vol. 4, no. 2, 2022.
doi: 10.21926/rpm.2202010.

[21] O. Emmanuel Chinonye and al, "Statistical analysis for orange G adsorption using kola nut shell activated carbon," J. Chinese Adv. Mater. Soc., vol. 6, no. 4, pp. 605–619, Oct. 2018.
doi: 10.1080/22243682.2018.1534607.

[22] I. C. Ositadinma and al, "Optimum process parameters for activated carbon production from rice husk for phenol adsorption," Curr. J. Appl. Sci. Technol., pp. 1–11, Aug. 2019.
doi: 10.9734/cjast/2019/v36i630264.

[23] N.C. Oguanobi and al, "Adsorption of a dye (crystal violet) on an acid modified non-conventional adsorbent, " J. Chem. Technol. Metallurgy, vol. 54, no. 1, pp 95–110, 2019.

[24] H. Mazaheri and al, "Application of machine/statistical learning, artificial intelligence and statistical experimental design for the modeling and optimization of methylene blue and Cd^{2+} removal from a binary aqueous solution by natural walnut carbon," Phys. Chem. Chem. Phys., vol. 19, no. 18, pp. 11299–11317, 2017.
doi: 10.1039/C6CP08437K.

[25] M. Taran and E. Aghaie, "Designing and optimization of separation process of iron impurities from kaolin by oxalic acid in bench-scale stirred-tank reactor," Appl. Clay Sci., vol. 107, pp. 109–116, Apr. 2015.
doi: 10.1016/j.clay.2015.01.010.

[26] G. Sodeifian and al, "Evaluation of the response surface and hybrid artificial neural network-genetic algorithm methodologies to determine extraction yield of Ferulago angulata through supercritical fluid," J. Taiwan Inst. Chem. Eng., vol. 60, pp. 165–173, Mar. 2016.
doi: 10.1016/j.jtice.2015.11.003.

[27] J. L. Pilkington and al, "Comparison of response surface methodology (RSM) and artificial neural networks (ANN) towards efficient extraction of artemisinin from Artemisia annua," Ind. Crops Prod., vol. 58, pp. 15–24, Jul. 2014. doi: 10.1016/j.indcrop.2014.03.016.

[28] J. Shafi and al, "ANN and RSM based modelling for optimization of cell dry mass of Bacillus sp. strain B67 and its antifungal activity against Botrytis cinerea," Biotechnol. Biotechnol. Equip., vol. 32, no. 1, pp. 58–68, Jan. 2018. doi: 10.1080/13102818.2017.1379359.

[29] M. Bhowmik and al, "Sono-assisted rapid adsorption of anionic dye onto magnetic $CaFe_2O_4/MnFe_2O_4$ nanocomposite from aqua matrix," Powder Technol., vol. 354, pp. 496–504, Sep. 2019. doi: 10.1016/j.powtec.2019.06.009.

[30] O. Chijioke Elijah and al, "Application of modified agricultural waste in the adsorption of bromocresol green dye," Asian J. Chem. Sci., pp. 15–24, Jan. 2020. doi: 10.9734/ajocs/2020/v7i119011.

[31] M. Venkatesh Prabhu and R. Karthikeyan, "Comparative studies on modelling and optimization of hydrodynamic parameters on inverse fluidized bed reactor using ANN-GA and RSM," Alexandria Eng. J., vol. 57, no. 4, pp. 3019–3032, Dec. 2018. doi: 10.1016/j.aej.2018.05.002.

[32] C. E. Onu and al, "Comparative analysis of RSM, ANN and ANFIS and the mechanistic modeling in eriochrome black-T dye adsorption using modified clay," South African J. Chem. Eng., vol. 36, no. December, pp. 24–42, 2021. doi: 10.1016/j.sajce.2020.12.003.

[33] M. Kaveh and al, "ANFIS and ANNs model for prediction of moisture diffusivity and specific energy consumption potato, garlic and cantaloupe drying under convective hot air dryer," Inf. Process. Agric., vol. 5, no. 3, pp. 372–387, Sep. 2018. doi: 10.1016/j.inpa.2018.05.003.

[34] A. M. Joglekar and A. T. May, "Product excellence through design of experiments, " Cereal. Food World, vol. 32, no. 12, pp 857–868 1987.

[35] M. Aminian and R. Teimouri, "Erratum to: Application of soft computing techniques for modeling and analysis of MRR and taper in laser machining process as well as weld strength and weld width in laser welding process," Soft Comput., vol. 19, no. 3, pp. 811–811, Mar. 2015.

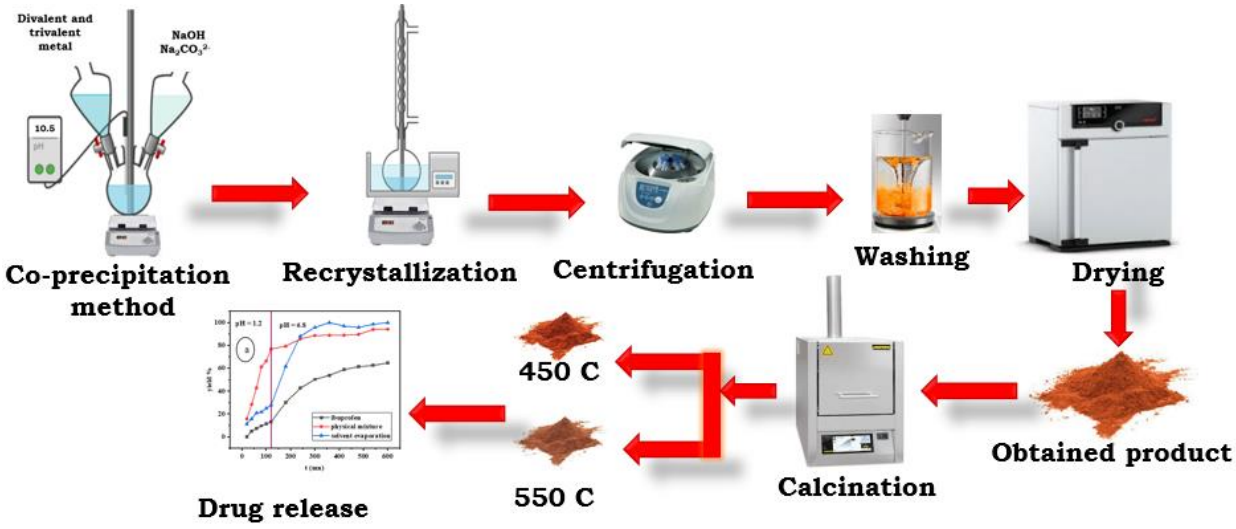
doi: 10.1007/s00500-014-1566-4.

[36] M. T. Dastorani and al, “Application of ANN and ANFIS models for reconstructing missing flow data,” Environ. Monit. Assess., vol. 166, no. 1–4, pp. 421–434, Jul. 2010. doi: 10.1007/s10661-009-1012-8.

[37] H. A. M. Atta, “Artificial Neural Network [ANN] modeling for tetracycline adsorption on rice husk using continuous system,” Desalin. Water Treat., vol. 317, no. December 2023, p. 100026, 2024.
doi: 10.1016/j.dwt.2024.100026.

Chapter 5

The Synthesis of Calcium-Iron Layered Double Hydroxide (CaFe-CO_3^{2-} LDH) as a Carrier for The Release of an Anti-inflammatory Drug in Gastrointestinal Medium.



Layered double hydroxides were used as a carrier in the biomedical field for controlled the release rate of drugs. As a results, LDHs have grown in popularity recently in the drug delivery system for their advantages based on the high capacity for loading pharmaceutical active agent, on the big specific surface area and the movable interlayer spacing of the LDHs. The goal of this study was to develop modified release drug delivery systems for the gastrointestinal tract using synthetic CaFe-CO_3 layered double hydroxides, to protect the anti-inflammatory drug ibuprofen from gastric acidity, and simultaneously to protect the gastric mucosa from the acidic nature of ibuprofen, thereby reducing adverse effects and maximizing therapeutic efficacy.

Results and discussion

1. XRD analysis

The X-ray diffraction of synthetic Ca-Fe-CO_3^{2-} LDH uncalcined and calcined at 450, and 550°C was illustrated in the **Figure 1**. The diffraction pattern results of the samples was simulated to the data obtained in the literature, the structure of obtained uncalcined LDH presented in the **Figure 1a**, was confirmed by the XRD patterns which indicate the presence of the basal peaks planes at (003), (006), (009), and (110) appearing at about 2theta values of 11.84°, 21.23°, 34.97° and 61.56°, respectively, are characteristic for LDH structure containing CO_3^{2-} as interlayer anion [1-7]. On the other hand, the data obtained from the sample confirm the presence of some extra peaks detected at 29.43°, 35.63°, and 47.13° in the structure of CaFe-CO_3^{2-} -LDH with different intensity, can be assigned to the formation of the calcium carbonate $CaCO_3$, with (104), (110) and (202) basal plans, and confirming with a reference code of (PDF: 00-005-0586), respectively. However, the calcined LDH at 450°C comprised mixed oxides, specifically iron oxide, calcium oxide, and iron hydroxide oxide, corresponding to reference codes (00-025-1402), (00-003-0865), and (01-076-0182), respectively. Finally, the calcined LDH at 550°C can be assigned to the formation of a mixture of hematite with the chemical formula of Fe_2O_3 and the rhomohedral structure of R-3c space group, and with orthrohombic $CaFe_2O_4$, which were indexed by the reference code of (01-079-1941) and (00-032-0168), respectively, in the high score plus data base.

The peaks detected at 24.2714°, 29.4708°, 33.2406°, 35.7069°, 40.8768°, 49.5631°, 54.0873°, 57.6800°, 62.5583°, 64.1204°, 72.0496°, 75.5903°, 82.9783°, 85.0032° and 88.6922°, which appearing at the basal peaks planes at (012), (210), (040), (201), (131), (241), (116), (018), (214), (300), (1 0 10), (220), (0 2 10), (134) and (226).

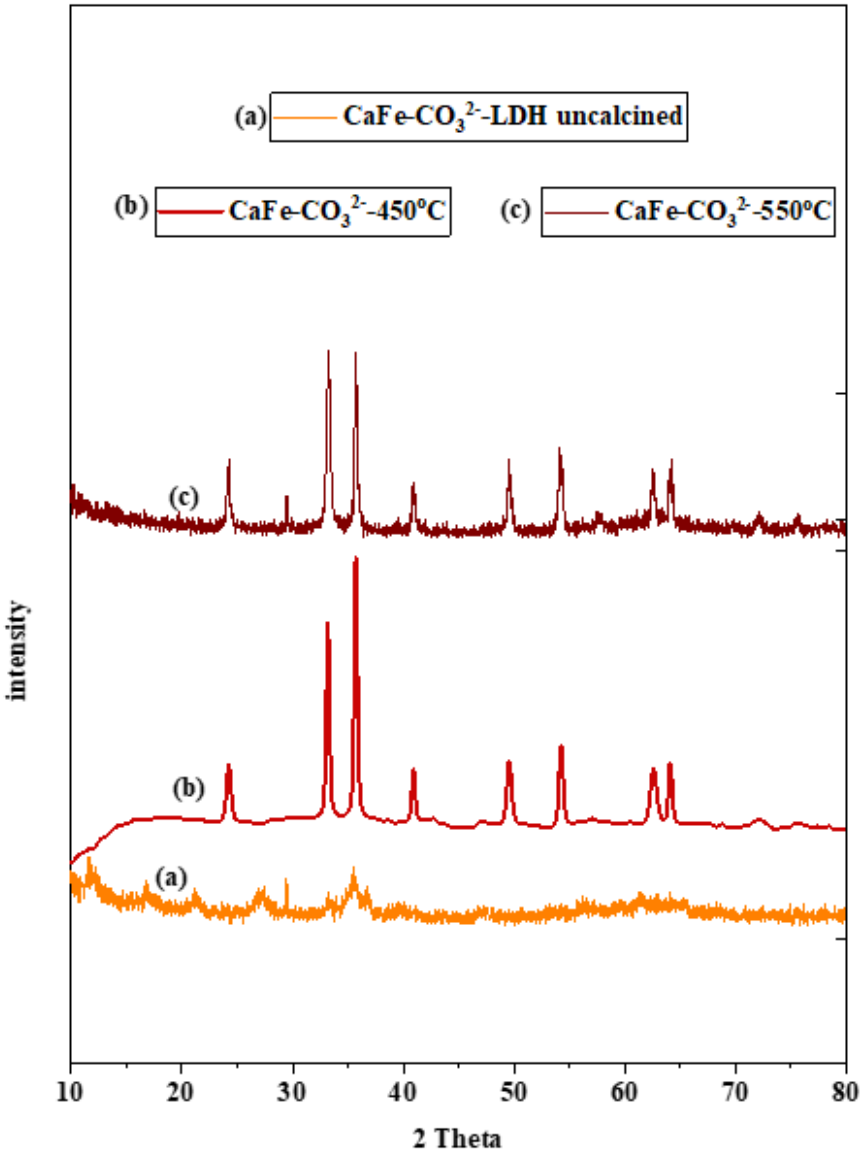


Figure 1: XRD spectra of (a) CaFe -CO_3^{2-} - LDH before calcination (orange), (b) CaFe - CO_3^{2-} - LDH calcined at 450°C (red) and after calcination at 550°C (wine).

2. FTIR analysis

Fourier Transform Infra-Red (FTIR) technique is one of the methods used to identify the structure of layered double hydroxides and the intercalated agent between the LDH layers. Generally, in the all of the FTIR spectrum of the hydrotalcite like the prepared layered double hydroxides (**Figure 2**), the absorption bands were listed in 04 classes. Firstly, the absorption bands around 3300 - 3600 cm^{-1} were presented the OH stretching vibration of H_2O molecules in the layered double hydroxides and in the metal hydroxide layers. Secondly, the OH bending vibration, which usually appeared in the region of 1620 cm^{-1}. Thirdly, the metal oxides vibration: M-O and O-M-O (with M = Ca or Fe) characteristic absorption bands can be appeared in the interval from 400 cm^{-1} to 1100 cm^{-1} .Finally, the absorption bands presented in the range from 800cm^{-1} to 1700cm^{-1} was usually identify the agent intercalated in the structure of layered double hydroxides such as the CO_3^{2-} [8].

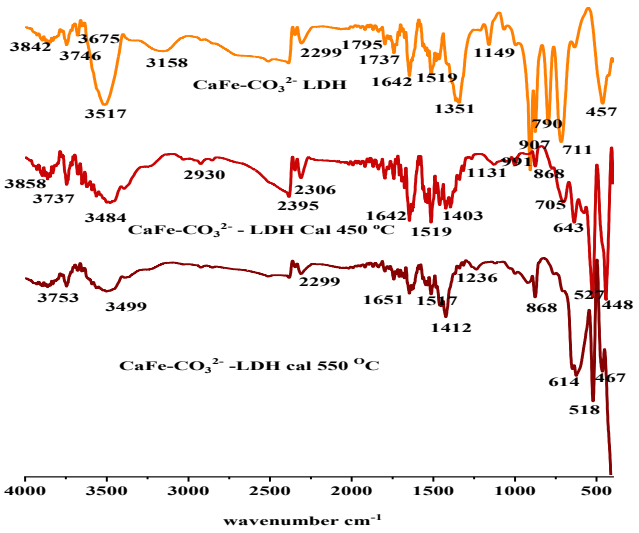


Figure 2: FTIR spectra of CaFe-CO_3^{2-} -LDH.

3. Zeta potential

The zeta potential measurement of the values between -10 mV and +10 mV are considered as a neutral charge [9], but the values indicated the high levels of stability are found in a samples with a values greater than +25 mV or less than -25 mV. Van Der Waals interparticle attractions will result in the aggregatement of low potential zeta values in dispersion [10]. Strongly cationic or anionic samples are identified by zeta potential signals greater than +30 mV or smaller than -30mV respectively [11].

The averaged of three measurements of the particle's stability using zeta potential was showed in the **Figure 3**. The sample's concentration was $3*10^{-3}$M in distilled water with pH value of 7.12, and it was measured at 25°C with an applied voltage of 150V.

The sample have a zeta potential measurement equals -7.47 mV, -13.7 mV and -20.9 mV with a standard deviation SD of 1.56 mV, 2.55 mV and 1.73 mV, and a conductivity of 0.0339 mS/cm, 0.0347 mS/cm and 0.0347 mS/cm for the CaFe-CO_3^{2-}-LDH, CaFe-CO_3^{2-}-LDH calcined at 450°C and CaFe-CO_3^{2-}-LDH calcined at 550°C respectively. So, the value of measurement zeta potential of CaFe-CO_3^{2-} (-7.47 mV) demonstrated the presence of the neutral charge in their surface (-10 mV < -7.47 mV < +10mV). The zeta potential measurements of LDH, CaFe-CO_3^{2-}-LDH calcined at 450°C and CaFe-CO_3^{2-}-LDH calcined at 550°C respectively are in the range of (-25 mV < -13.7 mV, -20.9mV < +25 mV) and in the range of (-30 mV < -13.7 mV, -20.9 mV< +30 mV), this signal demonstrated the presence of the negative charge on their surface as strongly anionic clay with a high level of stability.

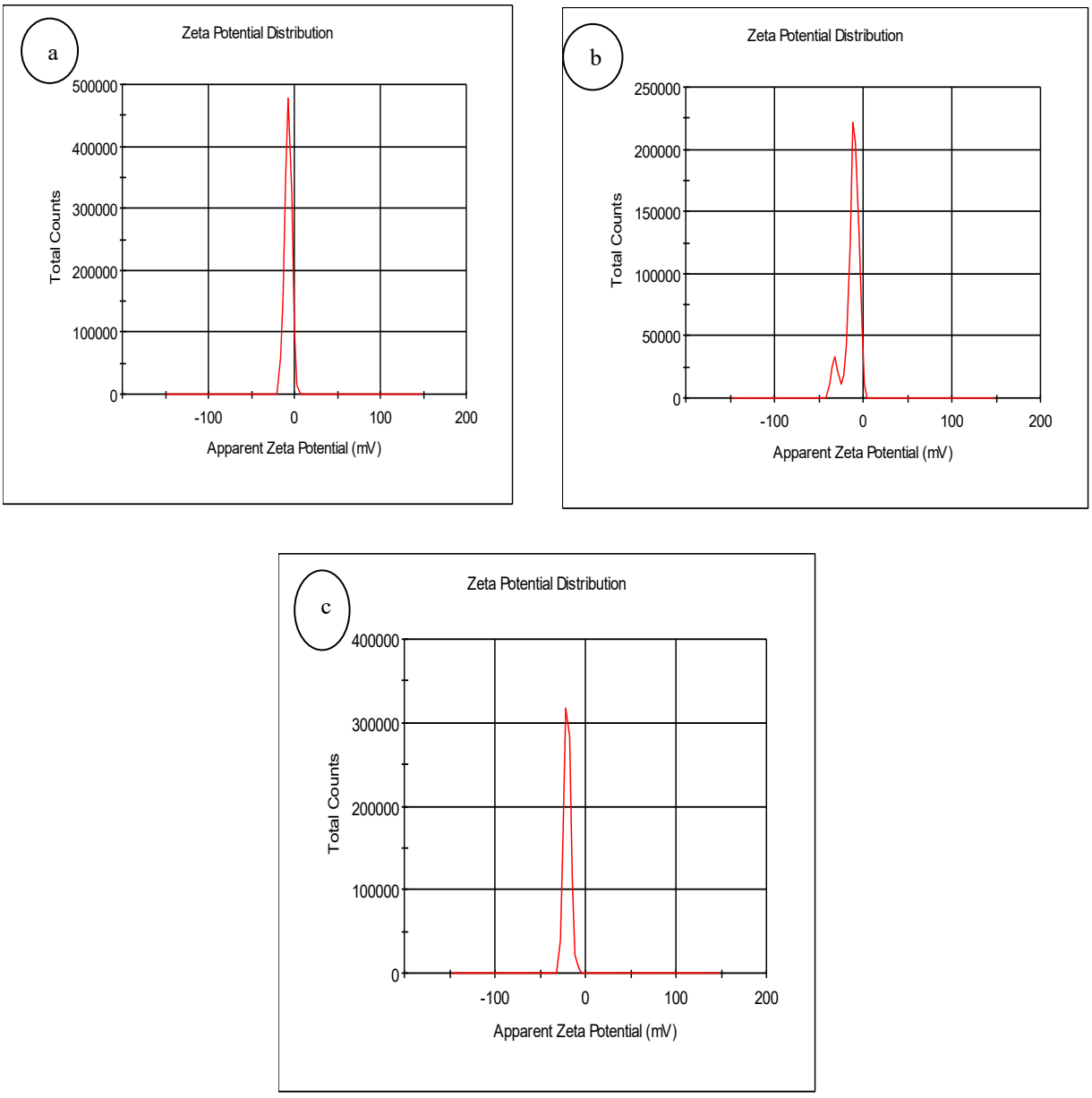
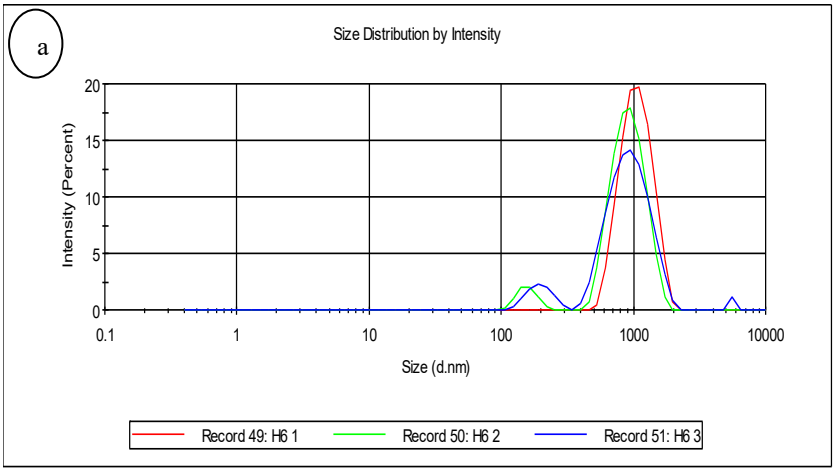
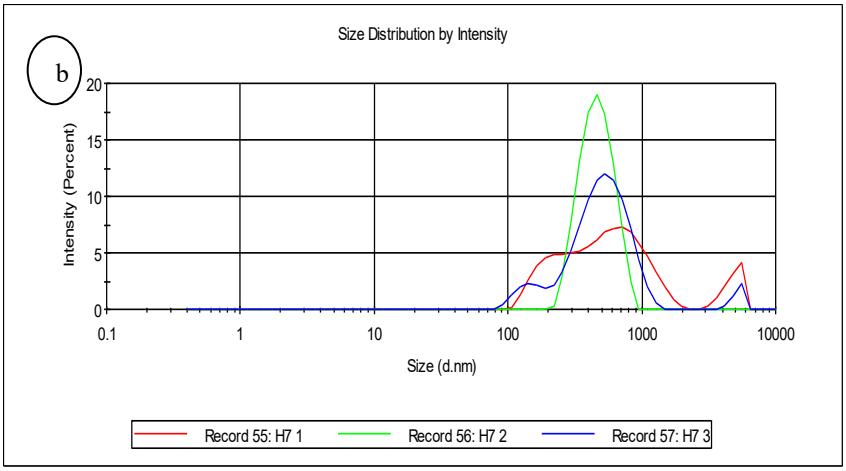


Figure 3: zeta potential of (a) CaFe-CO_3^{2-}-LDH uncalcined, (b) CaFe-CO_3^{2-}-LDH calcined at 450ºC and (c) CaFe-CO_3^{2-}-LDH calcined at 550ºC.

4. Size distribution

The averaged of three measurements of the particle's size distribution was showed in the **Figures 4**. The samples were measured at 25°C with a viscosity of 0.8872mPa.s. CaFe-CO_3^{2-}-LDH uncalcined (a), CaFe-CO_3^{2-}-LDH calcined at 450°C (b), and CaFe-CO_3^{2-}-LDH calcined at 550°C (c) have a mean measurement size equals to 973.4 nm, 491.3 nm and 404.9 nm with a standard deviation of 190.9, 25.67 and 44.1, respectively.





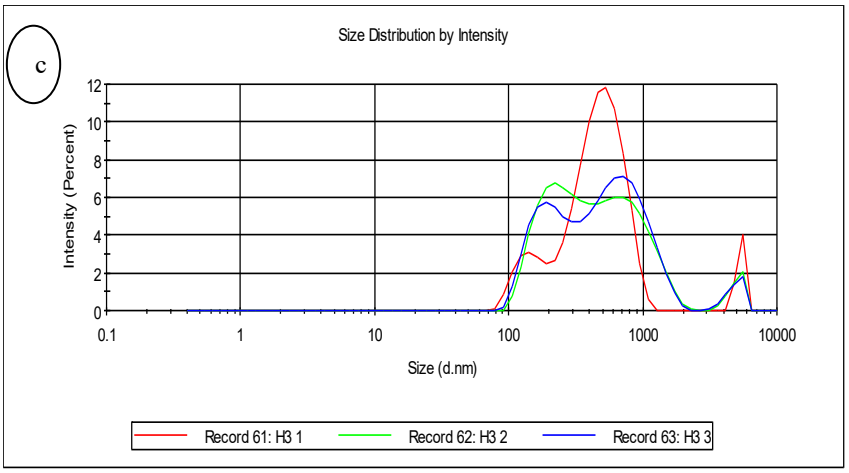


Figure 4: size distribution of (a) CaFe-CO_3^{2-}-LDH uncalcined, (b) CaFe-CO_3^{2-}-LDH calcined at 450°C and (c) CaFe-CO_3^{2-}-LDH calcined at 550°C.

5. Thermo-Gravimetric Analysis TGA

The **Figures 5** were presented the obtained results of the thermogravimetric analysis of our samples, which determined the mass loss as a function of temperature of CaFe-CO_3^{2-} LDH uncalcined, CaFe-CO_3^{2-} calcined at 450°C , CaFe-CO_3^{2-} calcined at 550°C and ibuprofen as a model drug, the curve reveals the steps of decomposition process of LDH samples in the range from 0°C to 1300°C for LDH and from 25°C to 488°C for ibuprofen.

The TGA/DSC curve of uncalcined CaFe-CO_3^{2-}-LDH with approximately 21% total weight loss across the temperature range studied. The blue TGA curve reveals five distinct decomposition stages: first, a sharp initial weight loss of about 14% from room temperature to 281°C corresponding to the removal of physically adsorbed water and interlayer water molecules, which is typical for hygroscopic LDH materials [1]. Second, a gradual weight loss of about 4% between 281 to 666°C associated with dehydroxylation of the LDH structure as hydroxyl groups in the brucite like layers condense and release water, leading to the collapse of the layered structure [12]. Third, a relatively stable region from 666 to 1128°C with minor continued weight loss of 1% related to decarbonation and transformation to mixed metal oxides.

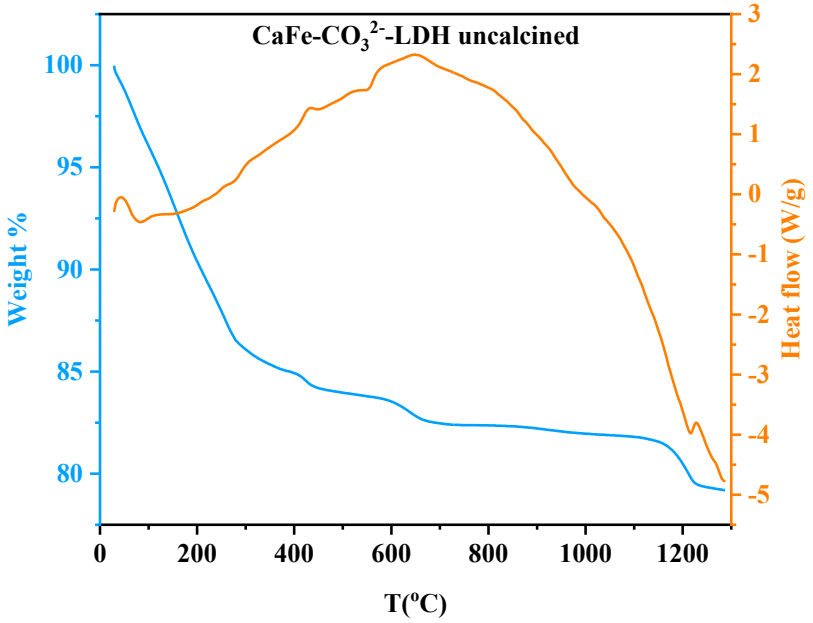
Fourth, a gradual loss of approximately 2% from 1128 to 1232°C, indicated the complete decarbonation and the final transformation to mixed metal oxides [13]. The final step, at high temperature more than 1232°C, which shown a weight loss may explain the fusion process of the metal presented in its structure. The orange DSC curve complements this with an endothermic peak around 82°C corresponding to the removal of water molecules, a broad exothermic peak approximately at 651°C indicating the crystallization of new oxide phases and possible combustion of organic components as the LDH structure decomposes to form mixed metal oxides, and a sharp endothermic drop around 1219°C suggesting a phase transformation or melting event in the resulting oxide mixture. Overall, the analysis confirms typical thermal behavior for carbonate intercalated LDH materials and indicates complete decomposition to metal oxides by approximately 1228°C.

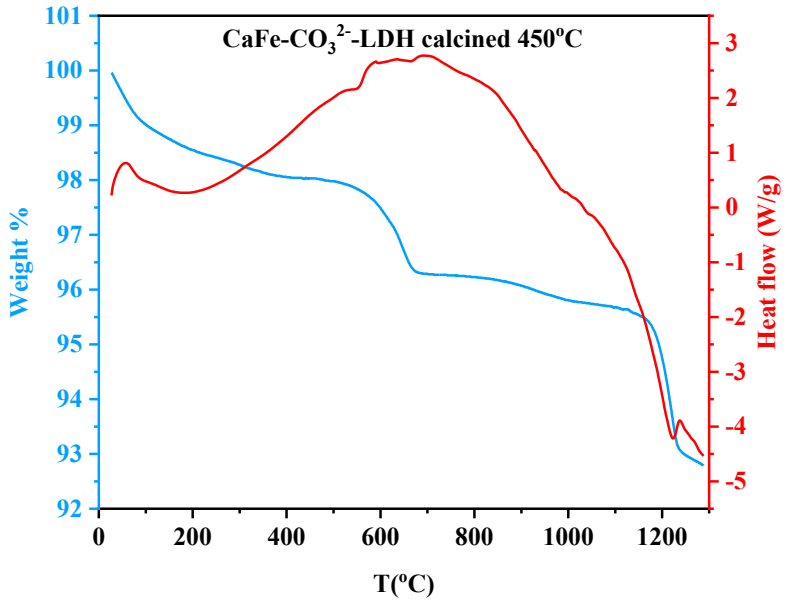
This TGA/DSC curve shows the thermal behavior of CaFe-CO_3^{2-}-LDH that has been precalcined at 450°C, exhibiting significantly different decomposition characteristics compared to the uncalcined material with a total weight loss of only about 8%. The blue TGA curve shows that the initial weight loss stage associated with physically adsorbed and interlayer water from room temperature to 359°C, is much smaller at only 2%, indicating that the precalcination process has already removed most of the water content and initiated partial dehydroxylation of the LDH structure. The most significant weight loss of approximately 2% occurs between 359 to 675°C, corresponding to further dehydroxylation and the beginning of decarbonation, as the material continues its structural transformation that was initiated during the 450°C precalcination [14]. A gradual weight loss of about 3% is observed from 675 to 1233°C, primarily associated with the complete removal of residual carbonate anions and final conversion to stable mixed metal oxides [15], such as CaO and Fe_2O_3. The red DSC curve shows a small exothermic event around 58°C corresponding to residual water removal, a broad exothermic peak at 699°C indicating continued phase transformation and crystallization of oxide phases, and a sharp endothermic drop around 1225°C suggesting a phase transition or partial melting of the oxide mixture. The significantly reduced total weight loss (7% versus 21% in the uncalcined sample) confirms that precalcination at 450°C has already completed the major dehydration and dehydroxylation processes, leaving primarily decarbonation and final oxide formation to occur at higher temperatures.

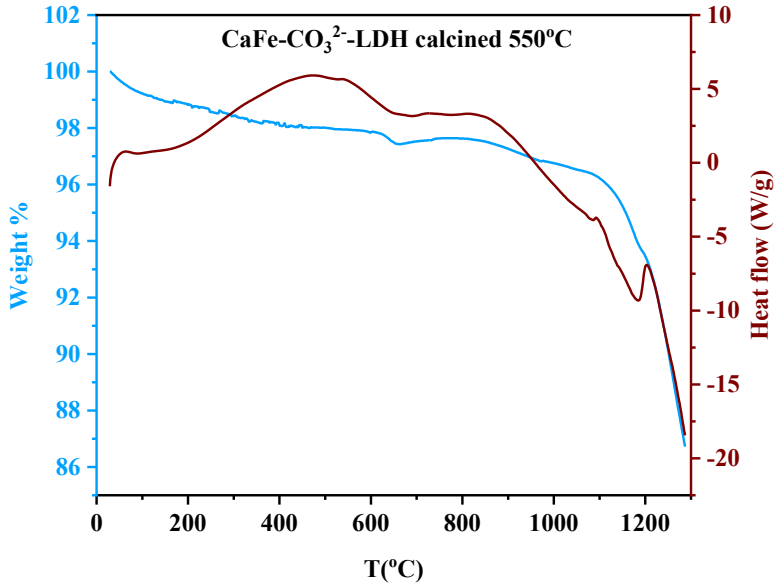
This TGA/DSC curve shows the thermal behavior of CaFe-CO_3^{2-}-LDH that has been precalcined at 550°C, displaying even more pronounced differences from the lower temperature calcined samples with a total weight loss of approximately 14%. The blue TGA curve reveals that the initial weight loss from room temperature to 306°C is minimal at less than 2%, confirming that the 550°C precalcination has effectively removed nearly all physically adsorbed and interlayer water. Between 306 to 1072°C, the material shows relatively stable weight with only about 2% loss, indicating that most of the dehydroxylation process was completed during the precalcination step. The most significant weight loss of approximately 10% occurs dramatically between 1072 to 1284°C, which is notably different from the previous samples and primarily corresponds to the decomposition of residual carbonate species that have become more thermally stable due to their incorporation into a partially transformed oxide matrix during the 550°C treatment. The red DSC curve shows small thermal events at lower temperatures, a broad exothermic region between 300 to 950°C with fluctuations indicating complex phase transformations and crystallization processes in the partially decomposed LDH structure, followed by a sharp and intense endothermic event around 1184°C, which is much more pronounced than in the samples calcined at lower temperatures and suggests a significant phase transition, likely the melting or major structural reorganization of the calcium iron oxide phases formed. The shift of major weight loss to higher temperatures (from 1000 to 1300°C) compared to the 450°C calcined sample demonstrates that precalcination at 550°C has created a more thermally stable intermediate structure where remaining carbonates are more strongly bound within the evolving oxide framework, requiring significantly higher temperatures for complete decomposition and final oxide formation.

The TGA-DSC analysis of ibuprofen reveals 03 distinct thermal steps in the TGA curve. The initial step, occurring between 25 and 100 °C, indicates no observable mass loss, thereby confirming the lack of physiosorbed water molecules in the sample. The second thermal step, which takes place between 100 and 256 °C, corresponds to the total decomposition of ibuprofen with an amount approximately to 100%. The final stage (from 256 to 500°C) shows no further mass loss, indicating complete degradation of the organic content. In addition, the DSC curve features two endothermic peaks. The first peak, observed at 79.97 °C, corresponds to the melting transition of crystalline ibuprofen, occurring independently of any mass change [16].

The second endothermic peak, located at 215.76 °C, is closely associated with a marked mass loss in the TGA analysis. This combined thermal and gravimetric response is indicative of ibuprofen's decomposition process, during which volatilization and oxidative breakdown lead to substantial mass reduction. Beyond the decomposition region, the thermogram indicates no further significant mass loss, confirming the near-complete degradation of the drug [17]. In summary, the TGA-DSC results affirm the absence of surface bound moisture, accurately establish the melting point of ibuprofen, and effectively delineate the onset and progression of its thermal degradation.




CaFe-CO3 2--LDH calcined 450°C
Weight %
Heat flow (W/g)
T(°C)
101
100
99
98
97
96
95
94
93
92
3
2
1
0
-1
-2
-3
-4
-5
0
200
400
600
800
1000
1200


CaFe-CO3 2--LDH calcined 550°C
Weight %
Heat flow (W/g)
T(°C)
102
100
98
96
94
92
90
88
86
10
5
0
-5
-10
-15
-20
0
200
400
600
800
1000
1200

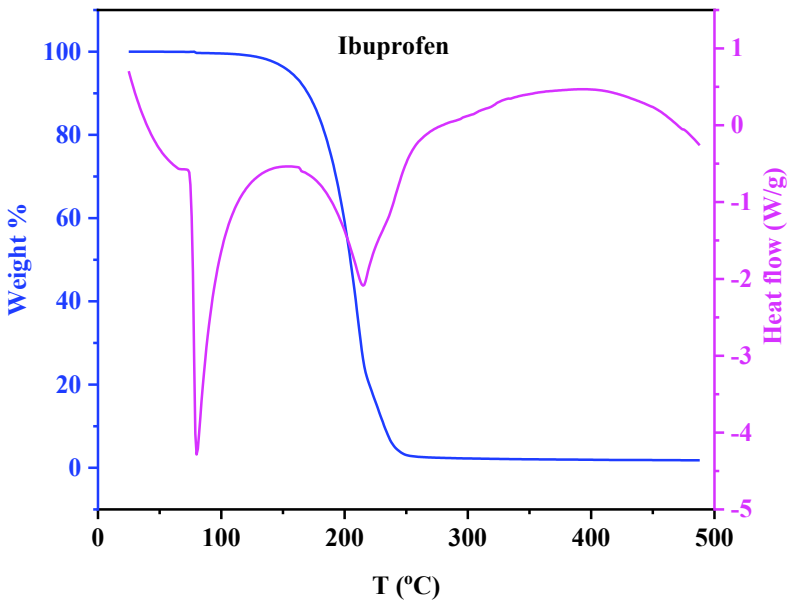
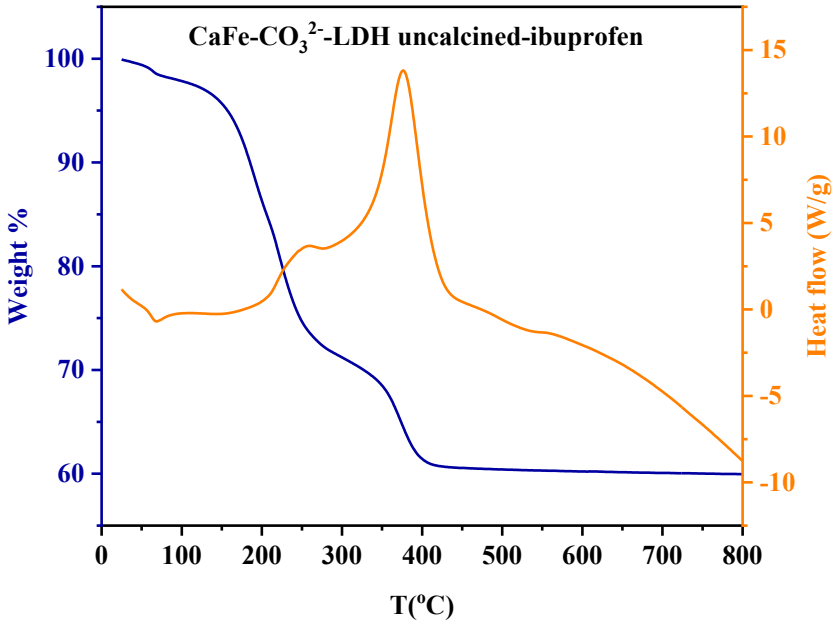


Figure 5: Thermogravimetric analysis of CaFe-CO_3^{2-} LDH uncalcined, CaFe-CO_3^{2-} LDH calcined and ibuprofen.

The **Figure 6** presented the obtained results of the TGA/DSC curves of our samples to calculate the amount of ibuprofen loaded into LDH. The uncalcined Layered Double Hydroxide demonstrates the highest ibuprofen loading capacity at 24.08%. This is attributed to its intact layered structure, which features accessible interlayer galleries, numerous hydroxyl groups, and carbonate exchange sites, all of which facilitate drug intercalation via anion exchange and hydrogen bonding. In contrast, the LDH calcined at 450°C exhibits a reduced loading capacity of 13.79%, likely due to partial collapse of its layered structure and the loss of interlayer sites. Despite this, the developed porous oxide structure still offers surface adsorption sites. Interestingly, the LDH calcined at 550°C shows an intermediate loading capacity of 20.77%. This suggests that the highly transformed mixed oxide structure produces unique surface properties, defect sites, or microporous regions that can effectively accommodate drug molecules through strong surface interactions. The presence of an additional high temperature exothermic peak in the 550°C sample indicates that some ibuprofen or its degradation products are more robustly retained within the oxide matrix.

All ibuprofen loaded samples exhibit distinct sharp exothermic decomposition peaks around 377 to 403°C, confirming the successful incorporation of the drug and indicating similar thermal degradation mechanisms across different LDH calcination states, although the intensity and specific temperature vary depending on the properties of the host matrix.



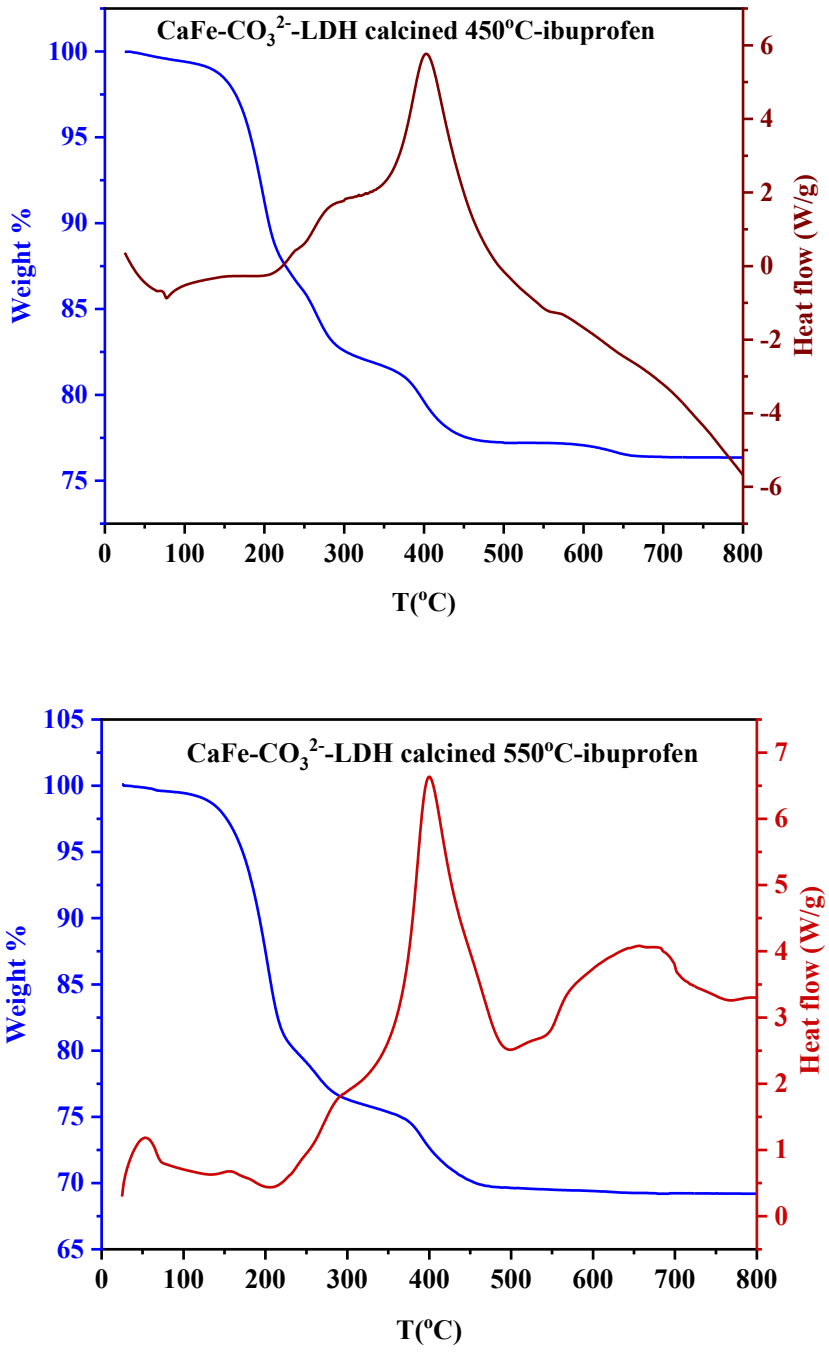


Figure 6: TGA/DSC curve of LDH-ibuprofen.

6. N_2 adsorption-desorption isotherm

The N_2 adsorption/desorption isotherm presented in **Figure 7,** shows the porosity characteristics of uncalcined CaFe-CO_3^{2-}-LDH, displaying a Type IV isotherm with H3 hysteresis according to IUPAC classification, which is characteristic of mesoporous materials [1]. The curve exhibits relatively low nitrogen uptake at low relative pressures ($P/P_0 < 0.3$) with adsorbed volumes around 2 to 2.5 mmol/g, indicating limited microporosity, which is typical for layered double hydroxides where the interlayer galleries are occupied by CO_3^{2-} anions and water molecules that restrict access to nitrogen molecules during analysis. A gradual and progressive increase in adsorbed volume occurs from P/P_0 of 0.3 to 0.9, rising from approximately 2.5 to 7 mmol/g, representing monolayer and multilayer adsorption on the pore walls and external surfaces of the LDH particles, with the continuously increasing slope suggesting a distribution of mesopore sizes. The most prominent feature is the steep uptake at high relative pressures ($P/P_0 > 0.9$) where the adsorbed volume increases sharply from about 7 mmol/g to nearly 15 mmol/g, indicating capillary condensation in larger mesopores and macropores formed by the interparticle voids between agglomerated LDH platelets. A clear hysteresis loop is present between the adsorption and desorption branches at relative pressures above $P/P_0 = 0.6$, with the desorption branch following a lower path than the adsorption branch, which is characteristic of H3 type hysteresis associated with slit shaped pores, plate like particle assemblies, or non-rigid aggregates of plate like particles. This hysteresis pattern confirms that nitrogen condenses into mesopores during adsorption but requires lower relative pressures to evaporate during desorption due to pore network effects and the geometry of slit shaped interparticle spaces created by the stacked LDH platelets. The overall isotherm profile indicates that the uncalcined LDH possesses a hierarchical porous structure with predominantly mesoporous and macroporous character arising from the aggregation and stacking of layered crystallites, providing accessible surface area and pore volume that could be beneficial for applications such as drug loading and adsorption processes.

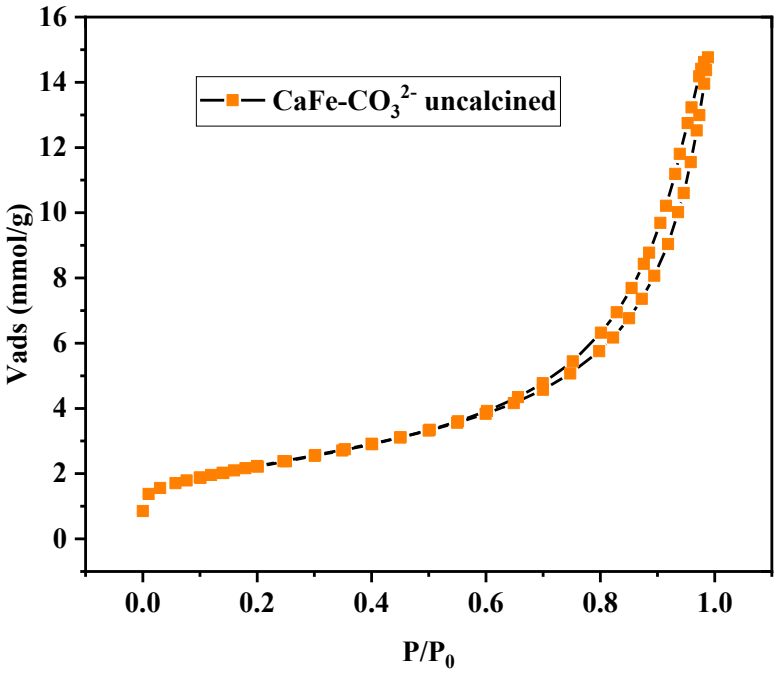


Figure 7: N_2 adsorption-desorption isotherm of uncalcined LDH.

The uncalcined layered double hydroxide material demonstrated a high specific surface area of S_{BET} = 179.4791 m^2/g, as determined by BET analysis. The cumulative pore volume for pores with diameters below 166.7878 nm, measured at a relative pressure of P/P_0 = 0.988266157, was found to be 0.511856 cm^3/g. Pore size analysis revealed average pore diameters of 11.4076 nm and 11.3041 nm for the adsorption and desorption branches, respectively, as calculated using the BET method (4V/A).

The pore size distribution curve presented in **Figure 8** demonstrates that the uncalcined layered double hydroxide sample possesses a heterogeneous pore structure dominated by mesopores [18], with the highest pore volume dV/dD = 0.025 cm^3/g nm, concentrated at small pore diameters under than 5 nm. The particle size distribution exhibits a characteristic exponential decay pattern, with pore volume sharply decreasing as pore diameter increases from 0 to approximately 30 nm, indicating that smaller mesopores constitute the majority of the porous architecture. Beyond 30 nm, the pore volume contribution becomes minimal and under than 0.005 cm^3/g nm, though the presence of a gradual tail extending to 150 nm suggests a continuous but sparse distribution of the

larger mesopores and some macropores. This pore size distribution, typical of layered double hydroxide materials, indicates a predominantly mesoporous structure with good accessibility for small to medium sized molecules, rendering the material potentially suitable for applications in drug delivery systems where mesoporous characteristics are advantageous.

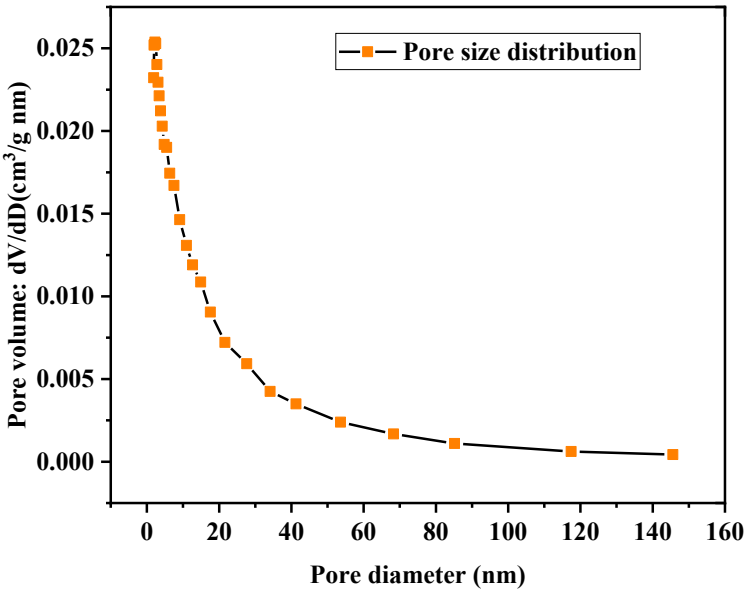


Figure 8: Pore size distribution of uncalcined LDH.

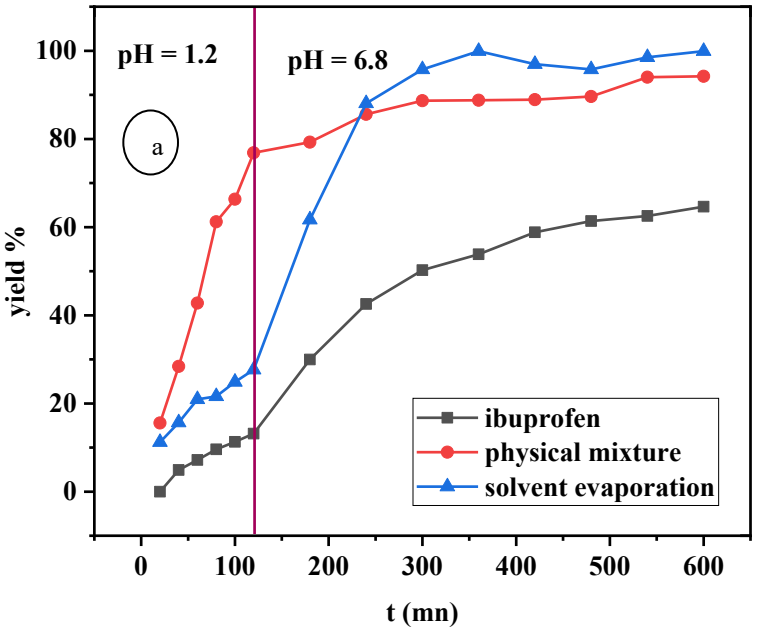
7. Drug release profile

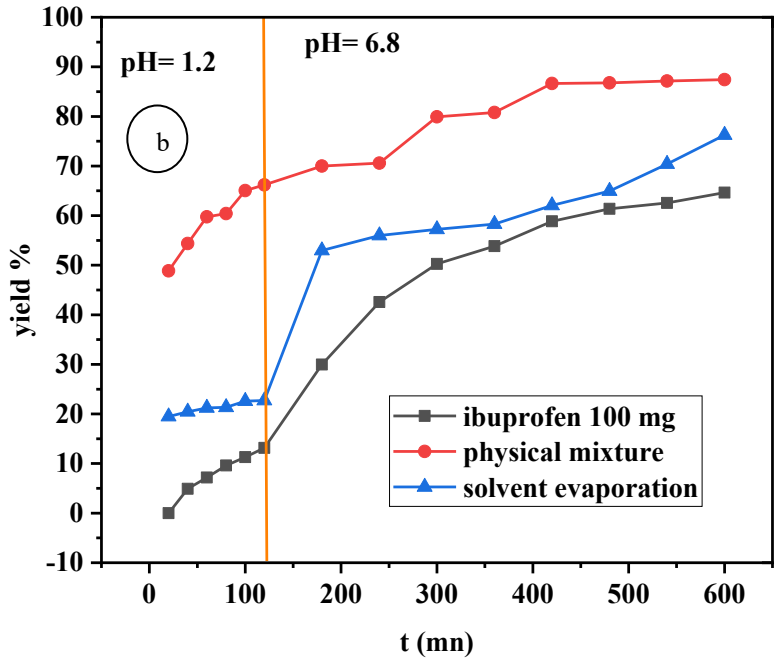
Ibuprofen belongs to the class of non-steroidal anti-inflammatory drugs (NSAIDs) and is commonly administered orally for the management of pain, reduction of fever, and treatment of inflammatory conditions. Despite its widespread use, ibuprofen exhibits limited solubility in aqueous environments, which restricts its dissolution from conventional solid dosage forms. As a consequence, oral administration often results in reduced bioavailability, particularly at higher doses, thereby increasing the likelihood of adverse side effects. To address this limitation, CaFe-CO_3^{2-} layered double hydroxide (LDH) was employed in this study as an excipient with the aim

of enhancing the solubility and dissolution behavior of ibuprofen within gastrointestinal conditions.

In this study two methods are used to loaded ibuprofen as a model drug into CaFe-CO_3^{2-} -LDH as a carrier; physical mixture and by solvent evaporation method. The drug release profile was presented in the **Figure 9**, it shows that the dissolution test of ibuprofen in simulated gastric fluid at pH = 1.2 dissolved a considerable amount about 13% from the control drug, when it was released 27%, 23% and 18% from the matrix containing LDH - Ibuprofen for the solvent evaporation method, but it was released 77%, 66% and 19% for the physical mixture method, for the CaFe-CO_3^{2-} -LDH uncalcined and calcined at 450 and 550^{O} C respectively and after 2 hours. On the other hand, the release of ibuprofen in simulated intestinal fluid at a pH = 6.8 was equivalent to 64% from the control sample and after 10 hours, when it was released a considerable amount from the matrix containing LDH-ibuprofen about 99%, 76% and 88% for the solvent evaporation method, and it was 94%, 87% and 89% for the physical mixture method, for the CaFe-CO_3^{2-} -LDH uncalcined and calcined at 450 and 550^{o}C, respectively.

The intercalation of ibuprofen into CaFe-CO_3^{2-} -LDH can protect this active compound from the effect of the physiological medium, the O-H groups into CaFe-CO_3^{2-} -LDH which interacted with ibuprofen can increase their solubility, to reduce the aggregation of the ibuprofen on the surface area of CaFe-CO_3^{2-} -LDH and to obtain the high therapeutic efficacity. The degradation of layered double hydroxide in the acidic medium have a positive effect to increase the solubility of ibuprofen and to simplify the removal of the LDH from the human body [19].


pH = 1.2
pH = 6.8
a
yield %
t (mn)
ibuprofen
physical mixture
solvent evaporation


pH= 1.2
pH= 6.8
b
yield %
t (mn)
ibuprofen 100 mg
physical mixture
solvent evaporation

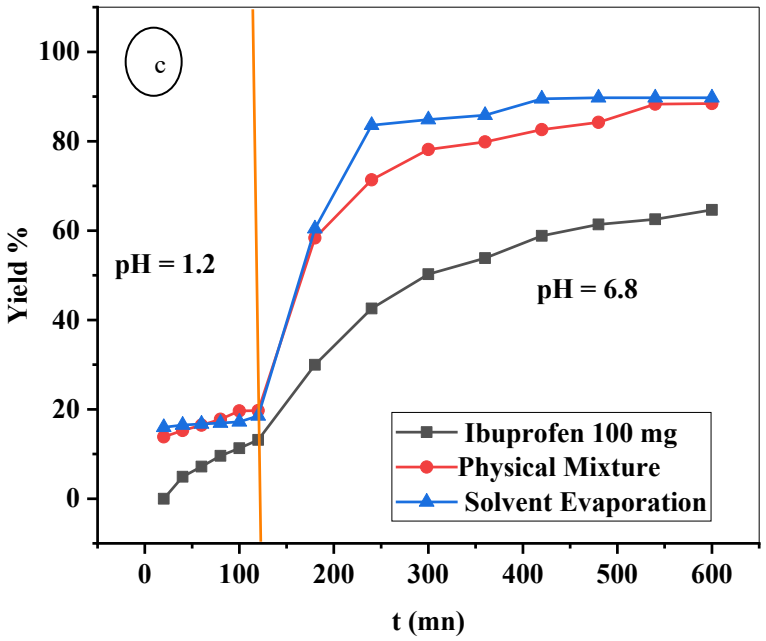


Figure 9: drug release from (a) CaFe-CO_3^{2-}-LDH non calcined, (b) CaFe-CO_3^{2-}-LDH calcined at 450°C and from (c) CaFe-CO_3^{2-}-LDH calcined at 550°C.

8. Conclusion

The drug carrier of CaFe-CO_3^{2-}-LDH was prepared by the coprecipitation method at constant pH = 10.5. This product was successfully loaded with ibuprofen as a model non-steroidal anti-inflammatory drug, using two methods; physical mixture and solvent evaporation. The in vitro release studies show that the LDH used have the ability to improve the solubility of ibuprofen in gastrointestinal medium and the solvent evaporation method was the best for released 99.9% of drug. So, the CaFe-CO_3^{2-}-LDH have gained significant attention as promising vehicles for drug release in gastrointestinal environment. Therefore, LDH as a carrier can protect the active pharmaceutical compound from the negative effects in the physiological medium, also to prevent it of their degradation, to improve their stability and their solubility, which can be beneficed on their optimal therapeutic efficacity. The degradation property of LDH in acidic medium have the ability to facilitate the removal of CaFe-CO_3^{2-}-LDH from the human body, thereby assuring the biological safety.

References

[1] K. Imene and al., "Thermal treatment of Cu-doped hydrotalcite-like adsorbents for improved removal of methyl orange from water," Sep. Purif. Technol., vol. 365, no. March, p. 132656, 2025.

doi: 10.1016/j.seppur.2025.132656.

[2] Z. Song and al, "In situ hydrolysis strategy to synthesis ultrathin CoNi-LDH nano fl owers for High-performance supercapacitors," J. Electroanal. Chem., vol. 936, no. March, p. 117379, 2023.

doi: 10.1016/j.jelechem.2023.117379.

[3] Z. Wang and al, "Eco-friendly in-situ synthesis of monolithic NiFe layered double hydroxide for catalytic decomposition of ozone," Catal. Commun., vol. 177, no. December 2022, p. 106635, 2023.

doi: 10.1016/j.catcom.2023.106635.

[4] P. Yazdani and al., "Layered double hydroxide nanoparticles as an appealing nanoparticle in gene / plasmid and drug delivery system in C_2C1_2 myoblast cells," Artif. Cells, Nanomedicine, Biotechnol., vol. 47, no. 1, pp. 436–442, 2019.

doi: 10.1080/21691401.2018.1559182.

[5] J. Chai and al., "Assembled Fe_3O_4 nanoparticles on Zn – Al LDH nanosheets as a biocompatible drug delivery vehicle for pH-responsive drug release and enhanced anticancer activity," Appl. Clay Sci., vol. 228, no. February, p. 106630, 2022.

doi: 10.1016/j.clay.2022.106630.

[6] A. Gnana and al, "Phosphate intercalated Mg / Al layered double hydroxide nanosheets as a novel flame retardant for leather : Synthesis , characterization , and application studies," Appl. Clay Sci., vol. 230, no. September, p. 106714, 2022.

doi: 10.1016/j.clay.2022.106714.

[7] E. Andr and al, "Layered Double Hydroxides (LDH) as nanocarriers for antimicrobial chemotherapy : From formulation to targeted applications," Materials Chemistry and Physics, vol. 293, no. September 2022, 2023.

doi: 10.1016/j.matchemphys.2022.126965.

[8] M. Shabanian and al, "FTIR characterization of layered double hydroxides and modified layered double hydroxides, " Journal of Polymer Nanocomposites, Elsevier Ltd, pp 77-102, 2020.

doi: 10.1016/B978-0-08-101903-0.00002-7.

[9] S. E. McNeil, Characterization of Nanoparticles Intended for Drug Delivery *(*Humana Press), Springer, pp 1-283, 2010.

doi: 10.1007/978-1-60327-198-1.

[10] P. Hirsch, "Zeta potential analysis of nanoparticles," Music Lett., vol. 32, no. 2, p. 204, 1951.

doi: 10.1093/ml/XXXII.2.204.

[11] N. E. A. El-Naggar and al, "Phycobiliprotein-mediated synthesis of biogenic silver nanoparticles, characterization, in vitro and in vivo assessment of anticancer activities," Sci. Rep., vol. 8, no. 1, pp. 1–21, 2018.

doi: 10.1038/s41598-018-27276-6.

[12] M. Szabados and al, "Conventional or mechanochemically-aided intercalation of diclofenac and naproxen anions into the interlamellar space of CaFe-layered double hydroxides and their application as dermal drug delivery systems ☆," Applied Clay Science, vol. 212, 2021.

doi: 10.1016/j.clay.2021.106233.

[13] M. Kostić and al., "Ultrasound-assisted synthesis of a new material based on MgCoAl-LDH : Characterization and optimization of sorption for progressive treatment of water," Environ. Technol. Innov., vol. 26, p. 102358, 2022.

doi: 10.1016/j.eti.2022.102358.

[14] J. Singh and S. Khare, "Facile synthesis , characterization , and catalytic activity of Cr (III) Schiff base complex immobilized on layered double hydroxide," Results Chem., vol. 4, no. September, p. 100503, 2022,

doi: 10.1016/j.rechem.2022.100503.

[15] A. R. Sangtam and al, "Synthesis and characterization of Co (II) – Co (III) LDH and Ac @ Co (II) – Co (III) LDH nanohybrid and study of its application as bactericidal agents," Results Chem., vol. 4, no. September, p. 100671, 2022.

doi: 10.1016/j.rechem.2022.100671.

[16] F. Xu and al, "Thermodynamic study of ibuprofen by adiabatic calorimetry and thermal analysis," Thermochimica, vol. 412, pp. 33–37, 2004.

doi: 10.1016/j.tca.2003.08.021.

[17] B. Tita and al, "Kinetic study of decomposition of ibuprofen under isothermal conditions," Methods, vol. 15, no. February, pp 29-32, 2011.

[18] A. R. Sangtam and al, "Synthesis and characterization of Co (II) – Co (III) LDH and Ac @ Co (II) – Co (III) LDH nanohybrid and study of its application as bactericidal agents," Results in Chemistry, vol. 4, no. September, 2022.

doi: 10.1016/j.rechem.2022.100671.

[19] T. Hu and al, "Layered Double Hydroxide-Based Nanomaterials for Biomedical Applications," Chemical Society Reviews, vol. 51, no 14, p. 6126-6176, 2022.

General conclusion

General conclusion

The development of controlled drug delivery systems has emerged as a crucial area in pharmaceutical sciences, aiming to improve therapeutic outcomes while minimizing adverse effects. The creation of modified release drug delivery systems in the gastrointestinal tract utilizing synthetic clay has long been an aim of science. The drug needs to be released in the best carrier possible from the intestine, which serves as the primary site of absorption. For this purpose, the goal of this study is to valorize the natural sources and to be used as starting material. Expanded perlite and bentonite are used as raw aluminosilicate material to synthesized zeolite P and sodalite, respectively. The synthesized zeolites are investigated for their potential pharmaceutical application as a carrier for the controlled release of ibuprofen in simulated gastrointestinal fluid for zeolite P, and was tested at different pH medium. In parallel, computational studies were conducted on the ibuprofen molecule to complement the experimental results. Density Functional Theory (DFT) calculations were used to optimize its molecular geometry, evaluate the energy gap, and analyze its electronic and vibrational properties. Additionally, molecular docking simulations were carried out to investigate the interaction of ibuprofen with its biological targets, providing insight into its binding affinity and interaction mechanisms. Furthermore, the antibacterial activity of the synthesized zeolite P and Ag-doped zeolite P (1 wt% Ag) was evaluated against selected bacterial strains. The incorporation of silver into the zeolite framework aimed to enhance its antimicrobial properties while maintaining its structural integrity. Comparative analysis between the undoped and Ag-doped samples demonstrated the influence of silver on the antibacterial efficiency of zeolite P, confirming its potential use in biomedical and pharmaceutical applications. To systematically evaluate and optimize the synthesis and release performance, a statistical and artificial intelligence-based modeling approach was employed. A Box-Behnken experimental design was developed using Design Expert software, and the experimental data were analyzed through response surface methodology (RSM). In addition, advanced artificial intelligence models, including artificial neural networks (ANN), adaptive neuro-fuzzy inference systems (ANFIS), and genetic algorithms (GA), were applied to model, predict, and optimize the system behavior. A comparative assessment of these modeling techniques was conducted to identify the most accurate and efficient approach for describing and optimizing the ibuprofen release performance of the synthesized sodalite zeolite.

Zeolite P was successfully synthesized from expanded perlite, a natural aluminosilicate source, using the hydrothermal method. The synthesized zeolite P demonstrated the ability to load and release ibuprofen used as a model anti-inflammatory drug in simulated gastrointestinal fluids. To enhance its antimicrobial activity and drug release rate, zeolite P was further modified by photodeposition with 1% silver. As a novel drug carrier in the biopharmaceutical field, zeolite P facilitates the controlled release of ibuprofen in the gastrointestinal environment, helping to protect the drug from gastric acidity and, conversely, to shield the stomach from the acidic nature of ibuprofen, which is known to cause gastric irritation and ulcers. Furthermore, DFT/B3LYP/6-311G calculations were performed to predict the molecular properties of four ibuprofen conformations, while molecular docking simulations were carried out to explore the binding affinities and interaction types between ibuprofen (ligand) and the 5F1A protein (receptor).

The ibuprofen release profiles in a simulated gastrointestinal environment, at pH 1.2 representing the gastric medium and pH 6.8 representing the intestinal medium. The control test (pure ibuprofen) exhibited a rapid release in the acidic medium, with 27.65% of ibuprofen released within the first two hours. In comparison, the ibuprofen-zeolite P matrix released 44.01%, while the ibuprofen-zeolite P-Ag matrix showed the highest release of 49.66% under the same conditions. After two hours of dissolution testing in the intestinal pH environment (pH 6.8), the samples exhibited a gradual increase in ibuprofen release over the time range of 2 to 10 hours. The cumulative amounts of ibuprofen released in the intestinal medium were 99.90% for the control sample, 67.11% for the ibuprofen-zeolite P matrix, and 82.62% for the ibuprofen-zeolite P-Ag matrix. These results indicate that silver modification of zeolite P via the photodeposition method enhanced the drug release behavior of the composite in the simulated gastrointestinal medium when compared to the unmodified zeolite P matrix.

According to the results obtained from the agar well diffusion method, small inhibition zones were observed around the wells, indicating that zeolite P was able to diffuse through the agar medium and inhibit bacterial growth at high concentrations. For the Gram-positive strains, the inhibition zones were 14 mm for *Staphylococcus aureus methicillin*-resistant (MRSA) ATCC 43300 and 11 mm for *Bacillus subtilis* ATCC 6633. For the Gram-negative strains, the inhibition zones were 9 mm for *Pseudomonas aeruginosa* ATCC 27853 and 8 mm for *Escherichia coli* ATCC 7839 at a concentration of 100 mg/mL. In contrast, the silver doped zeolite P (S-Ag) exhibited a stronger

antibacterial effect, producing larger and clearer inhibition zones against both Gram-positive and Gram-negative bacteria across all tested concentrations. The increase in inhibition zone diameter at higher concentrations demonstrated that the antibacterial activity of both zeolite P and zeolite P-Ag was dose dependent. The minimum inhibitory concentration (MIC) was defined as the lowest concentration of zeolite capable of inhibiting bacterial growth after 24 hours of incubation, as determined using the 96 well microplate dilution method. These findings demonstrate that zeolite P inhibited bacterial growth only at high concentrations, consistent with the inhibition zones observed in the agar well diffusion assay and further confirmed by the MIC test. In contrast, the silver doped zeolite P (1% Ag) exhibited a MIC value of 0.625 mg/mL, indicating a significantly enhanced antibacterial effect. However, at this concentration, the material showed no inhibitory activity against *Bacillus subtilis* ATCC 6633. Zeolite P exhibited a moderate minimum fungicidal concentration (MFC) of 25 mg/mL against both *Aspergillus niger* (ATCC 16888) and *Penicillium expansum* (ATCC 7861). This relatively high value may be attributed to the low solubility of zeolite P in distilled water, which limits its dispersion and interaction with fungal cells in the medium. In contrast, the modified zeolite P doped with 1% silver showed significantly lower MFC values, measured at 0.39 mg/mL for *Aspergillus niger* and 0.024 mg/mL for *Penicillium expansum*. These results indicate that silver modification substantially enhanced the antifungal activity of zeolite P, suggesting its promising potential for biomedical applications.

Sodalite zeolite was successfully synthesized from raw bentonite (Maghnite) as an aluminosilicate source and employed as a carrier material to control the release of ibuprofen in simulated body fluid. To reduce the number of required experiments and identify the key parameters influencing drug release, Design Expert software was used to evaluate 18 experimental runs involving three factors: pH, release time, and stirring speed. The results showed that the highest ibuprofen release occurred at pH 1, with a release time of 20 minutes and a stirring speed of 75 rpm. The predictive performance of the model was further validated using MATLAB through RMS, ANN, and AFNIS analyses based on artificial intelligence algorithms. In the Box–Behnken Design (BBD), the determination coefficient R^2 of 0.9693 demonstrated that the model explained approximately 95% of the total variance. Using the response surface methodology (RSM), the Central Composite Design (CCD) implemented in Design-Expert indicated that the quadratic model with a standard deviation of 0.0257 and R^2 of 0.9693 was the most suitable representation of the release behavior. Analysis of variance (ANOVA) confirmed the significance of the quadratic model and the

influence of the input variables, with a p-value < 0.0001 and an F-value of 28.03, supporting that the model explains 95% of the release variability. The model also presented a mean square of 0.0185 and a sum of squares of 0.1668. The artificial neural network (ANN) was trained using the Levenberg-Marquardt (LM) backpropagation algorithm with a multilayer perceptron (MLP) topology of 3-10-1 (three input nodes: pH, time, stirring speed; ten hidden neurons; one output node representing ibuprofen release). The ANN evaluation using 125 data sets produced a minimum validation mean square error (MSE) of 0.00022332 at the 1000^{th} epoch, indicating no signs of overfitting. Similarly, the AFNIS model (Adaptive Neuro-Fuzzy Inference System) was developed using the same MATLAB data set (125 × 3 input samples and 125 output samples). AFNIS achieved R^2 of 0.959934 with a final training error of 0.40066 after 1000 epochs. The results of RSM, ANN, and AFNIS supported by graphical and statistical analyses of predicted, experimental, and residual values confirmed that all three models were successful and accurate in estimating ibuprofen release behavior. Finally, the genetic algorithm (GA) was applied to optimize the release conditions. The optimal fitness was obtained at pH 4.234, t=53.452 minutes, and 63.581 rpm, corresponding to a predicted ibuprofen release of 0.469.

On the other hand, layered double hydroxides were used as a carrier in the biomedical field for controlling the release rate of drugs. As a result, LDHs have grown in popularity recently in the drug delivery system for their advantages based on the high capacity for loading pharmaceutical active agent, on the big specific surface area and the movable interlayer spacing of the LDHs. The goal of this study was to develop modified release drug delivery systems for the gastrointestinal tract using synthetic CaFe-CO_3 layered double hydroxides, to protect the anti-inflammatory drug ibuprofen from gastric acidity, and simultaneously to protect the gastric mucosa from the acidic nature of ibuprofen, thereby reducing adverse effects and maximizing therapeutic efficacy.

In this study two methods are used to loaded ibuprofen as a model drug into CaFe-CO_3^{2-} -LDH as a carrier; physical mixture and by solvent evaporation method. It shows that the dissolution test of ibuprofen in simulated gastric fluid at pH = 1.2 dissolved a considerable amount about 13% from the control drug, when it was released 27%, 23% and 18% from the matrix containing LDH - Ibuprofen for the solvent evaporation method, but it was released 77%, 66% and 19% for the physical mixture method, for the CaFe-CO_3^{2-} -LDH uncalcined and calcined at 450 and 550^{O} C respectively and after 2 hours. On the other hand, the release of ibuprofen in simulated intestinal

fluid at a pH = 6.8 was equivalent to 64% from the control sample and after 10 hours, when it was released a considerable amount from the matrix containing LDH-ibuprofen about 99%, 76% and 88% for the solvent evaporation method, and it was 94%, 87% and 89% for the physical mixture method, for the CaFe-CO_3^{2-} -LDH uncalcined and calcined at 450 and 550°C, respectively.

The intercalation of ibuprofen into CaFe-CO_3^{2-} -LDH can protect this active compound from the effect of the physiological medium, the O-H groups into CaFe-CO_3^{2-} -LDH which interacted with ibuprofen can increase their solubility, to reduce the aggregation of the ibuprofen on the surface area of CaFe-CO_3^{2-} -LDH and to obtain the high therapeutic efficacy. The degradation of layered double hydroxide in the acidic medium has a positive effect to increase the solubility of ibuprofen and to simplify the removal of the LDH from the human body.

Abstract: This study focuses on the development of controlled drug delivery systems utilizing synthetic clay, specifically zeolite P and sodalite, to enhance the therapeutic efficacy of non-steroidal anti-inflammatory drugs like ibuprofen. By valorizing natural resources such as expanded perlite and bentonite, zeolite P and sodalite were synthesized and assessed as carriers for the controlled release of ibuprofen in simulated gastro-intestinal conditions. Notably, the incorporation of 1% silver into zeolite P improved its antibacterial properties while maintaining structural integrity. These findings demonstrate the potential of zeolites and layered double hydroxides as effective carriers for drug delivery systems, addressing key challenges in enhancing the therapeutic efficacy of NSAIDs while minimizing adverse effects and increasing the therapeutic efficacity.

Keywords: zeolite, synthesis, natural resources, gastro-intestinal, LDH, drug delivery systems.

Résume : Cette étude se concentre sur le développement de systèmes de délivrance contrôlée de médicaments utilisant de l'argile synthétique, en particulier la zéolithe P et la sodalite, afin d'améliorer l'efficacité thérapeutique des anti-inflammatoires non stéroïdiens comme l'ibuprofène. En valorisant des ressources naturelles telles que la perlite expansée et la bentonite, la zéolithe P et la sodalite ont été synthétisées et évaluées tant que supports pour la libération contrôlée de l'ibuprofène dans des conditions gastro-intestinales simulées. Notamment, l'incorporation de 1 % d'argent dans la zéolithe P a amélioré ses propriétés antibactériennes tout en maintenant son intégrité structurelle. Ces résultats démontrent le potentiel des zéolithes et des hydroxydes doubles lamellaires tant que supports efficaces pour les systèmes de délivrance de médicaments, abordant ainsi des défis clés pour améliorer l'efficacité thérapeutique des AINS tout en minimisant les effets indésirables et en augmentant l'efficacité thérapeutique.

Mots clés : zeolite, synthèse, sources naturelles, gastro-intestinal, HDL, systèmes de libération des médicaments.

الملخص: تركز هذه الدراسة على تطوير أنظمة توصيل الأدوية الخاضعة للرقابة باستخدام الطين الاصطناعي، وتحديدًا الزيوليت Pوالصوداليت، لتعزيز الفعالية العلاجية للأدوية المضادة للالتهابات غير الستيرويدية مثل الإيبوبروفين. من خلال تثمين الموارد الطبيعية مثل البيرلايت الموسع والبنتونيت، تم تصنيع الزيوليت P والسوداليت وتقييمهما كحاملات للإطلاق المتحكم فيه للإيبوبروفين في محاكاة ظروف الجهاز الهضمي. والجدير بالذكر أن إضافة 1% من الفضة إلى الزيوليت P أدى إلى تحسين خصائصه المضادة للبكتيريا مع الحفاظ على سلامته البنيوية. توضح هذه النتائج إمكانات الزيوليت والهيدروكسيدات المزدوجة ذات الطبقات كحاملات فعالة لأنظمة توصيل الأدوية، ومعالجة التحديات الرئيسية في تعزيز الفعالية العلاجية لمضادات الالتهاب غير الستيروئيدية مع تقليل الآثار الضارة وزيادة الفعالية العلاجية.

الكلمات المفتاحية: الزيوليت، تصنيع، الموارد الطبيعية، الجهاز الهضمي، والهيدروكسيدات المزدوجة ذات الطبقات، أنظمة توصيل الأدوية.